DISSERTATION

THE DYNAMIC NATURE OF LIGAND LAYERS ON GOLD NANOCLUSTERS

Submitted by

Christopher Allen Hosier

Department of Chemistry

In partial fulfillment of the requirements

For the Degree of Doctor of Philosophy

Colorado State University

Fort Collins, Colorado

Spring 2020

Doctoral Committee:

Advisor: Christopher J. Ackerson

Alan J. Kennan
Chuck Henry
Matthew Kipper

Copyright Christopher Allen Hosier 2020
All Rights Reserved

ABSTRACT

THE DYNAMIC NATURE OF LIGAND LAYERS ON GOLD NANOCLUSTERS

Gold nanoclusters have been heavily investigated over the last few decades for their potential use in sensing, imaging, energy conversion, and catalytic applications. The development of methodology that allows for controlled functionalization of the surface ligand layer in these compounds is of particular interest due to the role of ligands in determining a large number of cluster properties. One of the fundamental ways of tailoring the ligand layer is the use of ligand exchange reactions. Despite the synthetic utility that ligand exchange reactions afford, a significant number of unanswered challenges currently limits the scope and control that can be obtained with these reactions. While a large variety of ligand types have been used to protect nanocluster surfaces, the majority of reported ligand exchange reactions revolve around chalcogenate-for-chalcogenate exchange. Site-selectivity in these reactions is limited to kinetic phenomenon, and the role of intercluster exchange largely remains a mystery. Additionally, recent works suggest that changes in ligand orientation can impact bulk material properties. In this thesis, we seek to address these challenges by reporting new exchange methodology, probing the evolution of exchanged ligand layers over time, investigating the stability of ligand layers in reaction conditions, and exploring the impact of ligand orientation on nanocluster behavior and reactivity. By addressing these questions and challenges, we seek to move closer to the goal of developing methodology that can be easily and reliably used to tailor gold nanoclusters for directed applications.

ACKNOWLEDGEMENTS

Outside of the “classic” chemistry building, there is a quote from Issac Newton: “If I have seen further, it is because of standing on the shoulders of giants.” While this saying is usually thought of in a scientific context where one’s research builds on previous findings, it can also describe the relationships that have helped me reach where I am. There are a large number of people who have substantially impacted my life over the last six years. Without their help, my life would be completely different from how it is right now. The following is a list of people who I owe an especially great deal of thanks to. It is by no means a comprehensive list, however, as there is a huge number of people who have supported and influenced me throughout graduate school.

To my family: Thank you for all your support throughout the last six years. There have been a lot of times throughout graduate school where it was difficult to get ahold of me and I was been distant and moody, but you have always supported me through those times and never complained. Whether I was struggling with deciding if I should switch research groups or how to afford food for the rest of the month, you were there to help how you could. I wouldn’t be where I am today without the advice, encouragement, and financial support you’ve given me over these last six years. Thank you for believing in me and what I can accomplish.

To Chris Ackerson: You were willing to take in another drifting organic student, thanks in part due to the (fortunate for me) departure of another student from your group. Despite a rocky first year and a half with the group where I was still struggling with motivation issues and confidence in my own abilities, you continued to be patient while gently

pushing me forward. This approach gave me room to find my own path in graduate school and helped me grow both as a chemist and as a person. I owe a lot of my successes in the last few years to this freedom, and I genuinely believe that I would not have reached this point with nearly any other boss.

To Dr. Heather Rubin: You have been one of my best friends throughout these crazy last six years. We've been through a lot of ups and downs together—both in my life and in your life—and we always made it work out in the long term. You were instrumental in helping me with switching research groups and were there to offer advice in all areas of life. Even during the times where I would feel down and would be aloof and difficult to deal with, you always seemed to be patient with me and would help out where you could. Plus you brought Bella into my life, so I naturally have to thank you for that as well.

To Dr. Scott Thullen: I'm fortunate that CU Boulder didn't notify you that you were accepted until the response deadline because I likely wouldn't have gotten to meet you otherwise. A lot of my favorite memories and experiences in grad school involve things we have done together, such as spending 10 hours summitting La Plata on our second attempt or getting together every week for our Risk Legacy series. I've learned to be a more active and healthier person from being around you and appreciate the impact you've had on me in how I view life and the world.

To Jonathan Thielman: A lot has changed since that first week of graduate school, including your transformation from preppy, clean shaven southern boy into scraggly Colorado mountain man. Your drive and passion for chemistry was always infectious though, and our talks about chemistry regularly forced me to consider new things. I'm a much better chemist now for knowing you. You also always seemed genuinely interested

in hearing about how I was doing and gave me a lot of room to just talk and share things when I needed it.

To Phil Knutson: It's a huge shame that you moved out to Georgia after our first year together in graduate school. Despite doing so, we've remained close over the years. You're some I've always looked up to for being genuine, open, and honest and have grown a lot as a person from being around you.

To Ben Unsworth: I don't think I can count the number of times you've been there for me to talk to when graduate school was taking its toll on me. You've always been incredibly generous to me and have helped me out in numerous ways, from constantly letting me vent about grad school issues to gifting me games so we could play something together. My graduate school experience and where I am in life would be entirely different if you didn't send me those computer parts several years as a long series of events never would have happened. I don't think I can thank you enough for all the help you've given me over the years I've been in grad school.

To Bryan Matthews: Your life has always challenged me to grow and consider what is possible in my own life, even as far back as middle school and high school. In a lot of ways, it seemed like you were constantly one step ahead in life and I was playing catch up. Despite talking about plans to go back to graduate school, I likely would still be working an unfulfilling job at MillerCoors or some other company if you weren't already applying to grad schools yourself. You've passively had a huge impact on the trajectory of my life, and I'm immensely grateful for it. I'm proud to see us both finishing our PhDs—even despite difficult life situations for us both in the last couple of years—and I look forward to what life has in store for us afterwards.

To Justin, Christina, Valerie, Addison, Zach, Fuz, Andrew, Erica, Kevin, Maddie, and all of my other “non-graduate school” friends in the general Fort Collins area: You all were my refuge away from graduate school for years. I’m fortunate that I was able to meet initially meet Justin, Christina, Valerie, Addison, and Fuz in rapid succession, and that I was able to form a large group of friends with all of you as you one-by-one moved out here. Whether we were getting together to watch kung fu movies, hike a fourteener, play board games at a brewery, or do anything else, I felt like I could disconnect from chemistry—a rare and fleeting feeling in my life—and be a normal person when around all of you. Even during the times when graduate school would ramp up and I would seemingly just disappear from life, you all were always understanding and never seemed to be phased by it happening. Thanks for all the great times over the years and for those that are to come.

To Marte, Jasper, Janik, Stefan, Luiza, Ruth, Lauro, and the other international people I have met: One of my greatest privileges in graduate school was getting the chance to get to know all of you. I have learned so much about the world and other ways of life from knowing you, and I feel I have grown so much as a person for it. I hope that we remain close over the years despite any physical distances, and I look forward to seeing those of you in Europe more soon.

DEDICATION

To my dad, who always believed I could do great things

TABLE OF CONTENTS

ABSTRACT……...ii
ACKNOWLEDGEMENTS……...iii
DEDICATION……..…vii
Chapter 1: Introduction……1
1.1 Introduction to Gold Nanoclusters……..1
1.2 Tuning Gold Nanocluster Properties *via* Ligand Exchange Reactions……..2
1.3 Ligand Dynamics on Gold Nanoclusters……3
1.4 Thesis Scope……..…5
Chapter 2: Regiochemistry of Thiolate for Selenolate Ligand Exchange on Gold Clusters
……..……..7
2.1 Synopsis……..…7
2.2 Introduction……..……..…7
2.3 General Methods……..……..……..…9
2.4 1:1 SPh:Au_{25} Ligand Exchange Results.....11
2.5 100:1 SPh:Au_{25} Ligand Exchange Results.....14
2.6 Discussion.....16
Chapter 3: Acetylide-for-Thiolate Ligand Exchange on Gold Clusters……21
3.1 Synopsis……21
3.2 Introduction……...21
3.3 Results and Discussion……..23
Chapter 4: Ligand Exchange of Non-Innocent Reactants and Products on $Au_{25}(PET)_{18}$ in
Thioether Oxidation Reactions……..……..…29
4.1 Synopsis……..……29
4.2 Introduction……...29
4.3 Results……...……..……..31
4.4 Discussion……..……36
Chapter 5: Conformational Polymorphism in $Au_{25}(PET)_{18}^0$……..40
5.1 Synopsis ……..40
5.2 Introduction……..…40
5.3 Results……..……...42
5.4 Discussion ……48
References ……..52
Appendix A: Supplementary to Chapter 2……...65
A.1 General Methods……..……65
A.2 Synthesis of $Au_{25}(PET)_{18}$TOA……65
A.3 Synthesis of $Au_{25}(SePh)_{18}$TOA……..……66
A.4 Ligand Exchange Reactions on $Au_{25}(PET)_{18}$TOA……..……66
A.5 Synthesis of $Au_{25}(SePh)_{18-x}(SPh)_x$TOA Crystals……67
A.6 MALDI-MS Data Collection and Spectra..……67
A.7 Single Crystal X-ray Diffraction Data Collection and Workup……69
A.8 Solvent Accessibility Calculations……..70
A.9 Crystallographic Ligand Exchange Results……71

A.10 Crystallographic Information File for Crystal #1 100 Equivalents PhSH at 5 Days……..……..…80
A.11 Crystallographic Information File for Crystal #2 100 Equivalents PhSH at 5 Days…….……84
A.12 Crystallographic Information File for Crystal #3 100 Equivalents PhSH at 5 Days……..…88
A.13 Crystallographic Information File for Crystal #1 100 Equivalents PhSH at 10 Days……..…92
A.14 Crystallographic Information File for Crystal #2 100 Equivalents PhSH at 10 Days……..…96
A.15 Crystallographic Information File for Crystal #1 100 Equivalents PhSH at 15 Days……100
A.16 Crystallographic Information File for Crystal #2 100 Equivalents PhSH at 15 Days……104
A.17 Crystallographic Information File for Crystal #1 1 Equivalent PhSH at 10 Days……108
A.18 Crystallographic Information File for Crystal #2 1 Equivalent PhSH at 10 Days……112
A.19 Crystallographic Information File for Crystal #3 1 Equivalent PhSH at 10 Days……116
A.20 Crystallographic Information File for Crystal #1 1 Equivalent PhSH at 15 Days……120
A.21 Crystallographic Information File for Crystal #2 1 Equivalent PhSH at 15 Days…….... 124
A.22 Crystallographic Information File for Crystal #3 1 Equivalent PhSH at 15 Days……127
Appendix B: Supplementary to Chapter 3……133
B.1 General Methods……133
B.2 MALDI-MS Data Collection……..……...…133
B.3 Synthesis of $Au_{25}(PET)_{18}TOA$……..……134
B.4 Synthesis of Gold(I)-Phenylacetylide..……135
B.5 Acetylide Exchange Reactions on $Au_{25}(PET)_{18}TOA$…..……135
B.6 Exchange of Lithium Phenylacetylide on $Au_{25}(PET)_{18}$…….……136
B.7 Synthesis of $Au_{44}(PA)_{28}$……136
B.8 Thiolate Ligand Exchange on $Au_{44}(PA)_{28}$……...137
B.9 Mass Spectrometry Results……137
Appendix C: Supplementary to Chapter 4……142
C.1 General Methods……...…142
C.2 Synthesis of $Au_{25}(PET)_{18}TOA$……142
C.3 Reaction Between $Au_{25}(PET)_{18}TOA$ and Thioethers…..……...143
C.4 MALDI-MS Data Collection……...143
Appendix D: Supplementary to Chapter 5…..……..147
D.1 General Methods……...…147
D.2 Synthesis of $Au_{25}(PET)_{18}TOA$……147
D.3 Crystallization of Cuboid $Au_{25}(PET)_{18}^0$ Samples……..……148
D.4 Crystallization of Quadrilateral Prism $Au_{25}(PET)_{18}^0$ Samples……..……...149

D.5 Crystallization of Thin Platelet $Au_{25}(PET)_{18}^0$ Samples……149
D.6 Crystallization of Needle $Au_{25}(PET)_{18}^0$ Crystals……....150
D.7 Single Crystal X-ray Diffraction Data Collection……....151
D.8 Solvent Accessibility Calculations……..……151
D.9 MALDI-MS Data Collection……..…152
D.10 Summary of Crystal Structure Results……153
D.11 Crystallographic Information File for $Au_{25}(PET)_{18}^0$ Needle Sample…….154
D.12 Crystallographic Information File for $Au_{25}(PET)_{18}$ Rhomboid Sample…….158
D.13 Crystallographic Information File for $Au_{25}(PET)_{18}$ Thin Film Sample.....162
D.14 Crystallographic Information File for $Au_{25}(PET)_{18}$ Quadrilateral Prism Sample
…..…….....…168

CHAPTER 1: INTRODUCTION TO LIGAND-PROTECTED GOLD NANOCLUSTERS

1.1 Introduction to Gold Nanoclusters

Since their first report in 1857,[1] gold nanoparticles—nanometer-sized aggregates of gold—have been investigated for their use in applications such as targeted biologic delivery,[2] photothermal and photodynamic therapy,[3,4] chemical and biological sensing,[5] bioimaging,[6] solar conversion,[7,8] and catalysis.[9] One challenge in developing gold nanoparticles for directed applications though is the ability to analyze the impact of specific changes in a nanoparticle. Nanoparticles lack structural uniformity, and are generally described in terms of size, dispersity (e.g.-7.3 nm ± 0.4 nm), and shape. Consequently, structural changes (e.g.-exchange of individual ligands or metal atoms) can be difficult to detect and structural ambiguity limits the determination of structure-property relationships.

To this end, gold nanoclusters can serve as ideal model systems for investigating related reactions and phenomena. Unlike gold nanoparticles, gold nanoclusters are monodisperse and can be assigned discrete formulae (e.g.-$Au_{25}(SR)_{18}$). This precision allows for a large number of analyses to be performed including the quantification of metal dopant atoms and exchanged ligands,[10–14] the identification of charge states,[15–17] and the detection of changes in cluster identity.[18–21] Additionally, the crystallographic determination of exact structures (figure 1.1) has afforded insight into the structural origins of material properties,[22–25] been used to probe site selectivity in exchange reactions,[26–32] and provided models for computational investigations.[33–37] Due to their smaller relative

size, gold nanoclusters also have properties which are more molecule-like compared to nanoparticles, making them materials of interest in their own right.

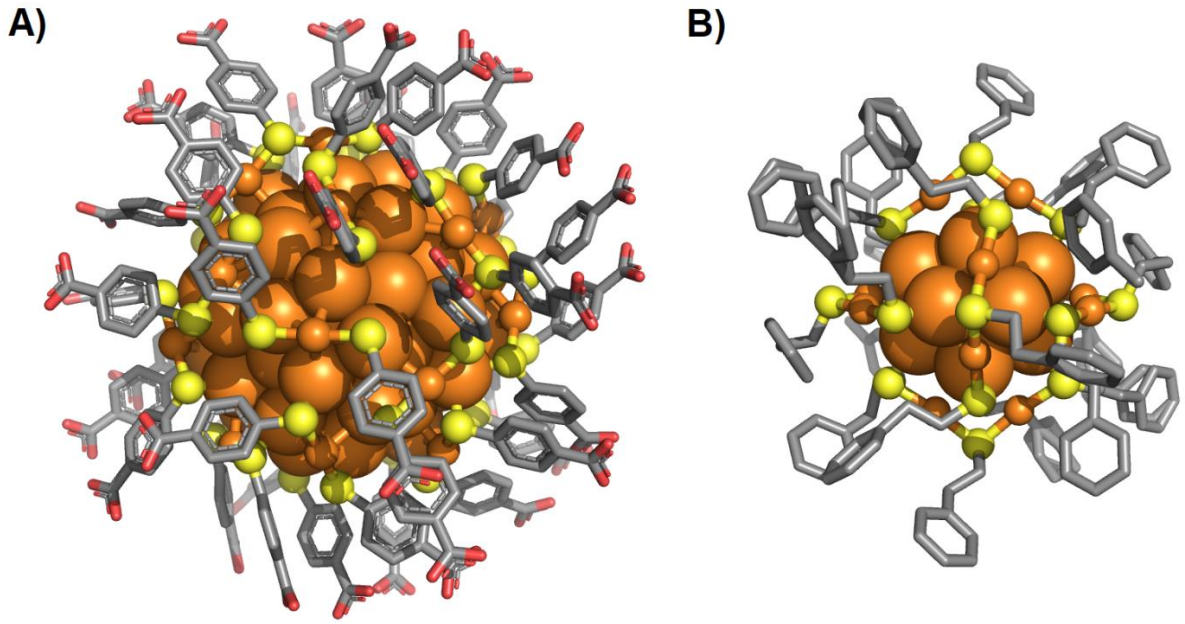


Figure 1.1 Crystal structures of A) Au_{102}(*p*-MBA)$_{44}$ and B) $Au_{25}(PET)_{18}^{0}$.

1.2 Tuning Gold Nanocluster Properties *via* Ligand Reaction Reactions

Phosphine-protected clusters were first studied in the 1960s.[38] Since then, a variety of ligand types have been utilized to passivate gold clusters, including thiolates,[39–41] selenolates,[42–44] tellurolates,[28,45] halides,[46–49] acetylides,[50–52] and *N*-heterocyclic carbenes.[53–55] This diversity in ligand choice has allowed for tailoring of nanocluster properties such as photoluminescence,[56] electrochemical response,[28,57] and catalytic activity.[58,59] Other aspects of ligands such as steric effects and the presence of additional functional groups can be manipulated to determine physical properties such as solubility and stability.[60,61] These effects can be highly sensitive in nature as changes in core structure, cluster size, and stability have been observed as a result of using different structural isomers of a ligand.[62–65]

Ligand exchange is one of the fundamental reaction types used to modify the ligand layer of gold nanoclusters. Exchange reactions have been used to functionalize nanocluster surfaces,[66–68] adjust specific nanocluster properties,[69] and induce structural transformations.[70–73] These reactions can result in either partial or full replacement of the ligand layer with the ligand feed ratio often controlling the degree of exchange.[14,74]

Despite the synthetic utility that ligand exchange reactions afford, a significant number of unanswered fundamental challenges limit the control and substrate scope that can be obtained with these reactions. While there are numerous reports of ligand exchange reactions, few of these examples involve ligand types other than chalcogenates. In the case of tellurolate-for-thiolate exchange, only partial replacement of the ligand layer has been achieved.[28,45] Partial exchange reactions often produce a large distribution of products that can be difficult to separate, limiting the synthetic usefulness of such reactions.[14,75,76] Further, there appears to be multiple mechanisms which affect site-selectivity in partial exchange processes.[75] Exploration into the factors affecting these pathways has yielded insights into the formation of kinetically-favorable products, but questions still remain about potential thermodynamically-favorable and intercluster exchange pathways.[26–28]

1.3 Ligand Dynamics on Gold Nanoclusters

Since the first reported thiolate-protected gold nanocluster crystal structure in 2007, x-ray crystallography has served as a critical technique for developing understanding of nanocluster reactivity and behavior.[39] However, this analytical approach only provides a “snapshot” of the nanocluster in one specific structural form. Compounds are inherently always in motion due to molecular vibrations and rotations and therefore their exact

structural forms are always changing. While it is theoretically possible to isolate and crystallographically determine multiple structural variations of the same compound, practically doing so can be a difficult undertaking. For this reason, only one crystal structure is normally reported for most compounds.

An emerging direction in nanocluster-related research over the last several years is the effects of ligand dynamics on gold nanocluster behavior and properties. In 2016, Häkkinen et al. reported the first empirical evidence suggesting dynamic behavior of ligands on gold nanoclusters (figure 1.2).[77] Subsequent investigations by other groups have suggested that ligands which form a more “rigid” layer improve emission intensity of the nanocluster relative to ligands which are more dynamic on the surface.[78,79] Similarly, “rigidifaction” of the ligand layer is believed to account for two instances of enhanced emission intensity in crystallized gold nanoclusters relative to those in other physical states (figure 1.3).[80,81]

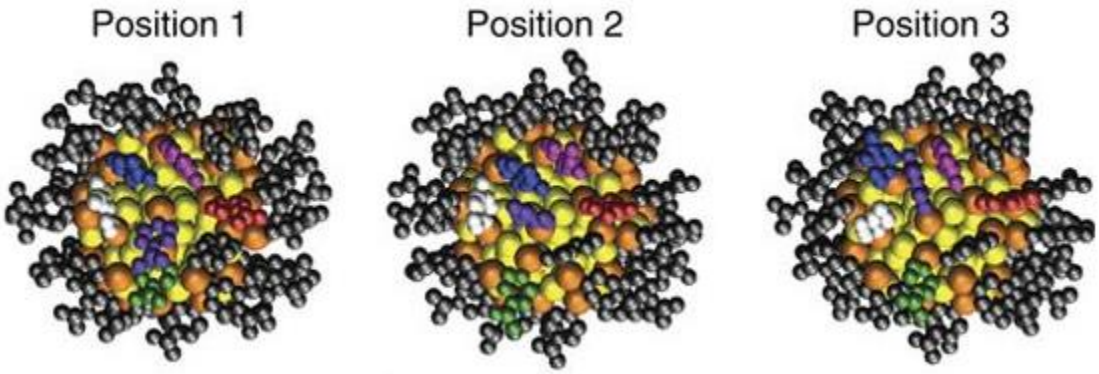


Figure 1.2 Calculated ligand conformations on Au_{102}(*p*MBA)$_{44}$ using molecular dynamics simulations. Figure is reproduced from Salorinne *et al.*[77]

Due to the recency of these initial results, little else is known about the nature of ligand dynamics on gold nanoclusters. It is unclear which properties might be affected by such behavior. While a reduction in dynamics appears to result in increased emission intensity,

changes to the conformation of a ligand layer are expected to have minimal impact on the resulting UV-Vis spectrum.[82] Conversely, a chiral ligand layer conformation might afford second-order non-linear optical properties in a symmetric cluster that otherwise would not exhibit such a response.[33] Surface dynamics might also hypothetically impact ligand exchange and catalytic reactions that occur at exposed surface gold atoms due to changes in surface solvent accessibility.[26–28,83–86] Control over dynamic processes represents an additional fundamental challenge that must be overcome to investigate and utilize these effects for specific applications.

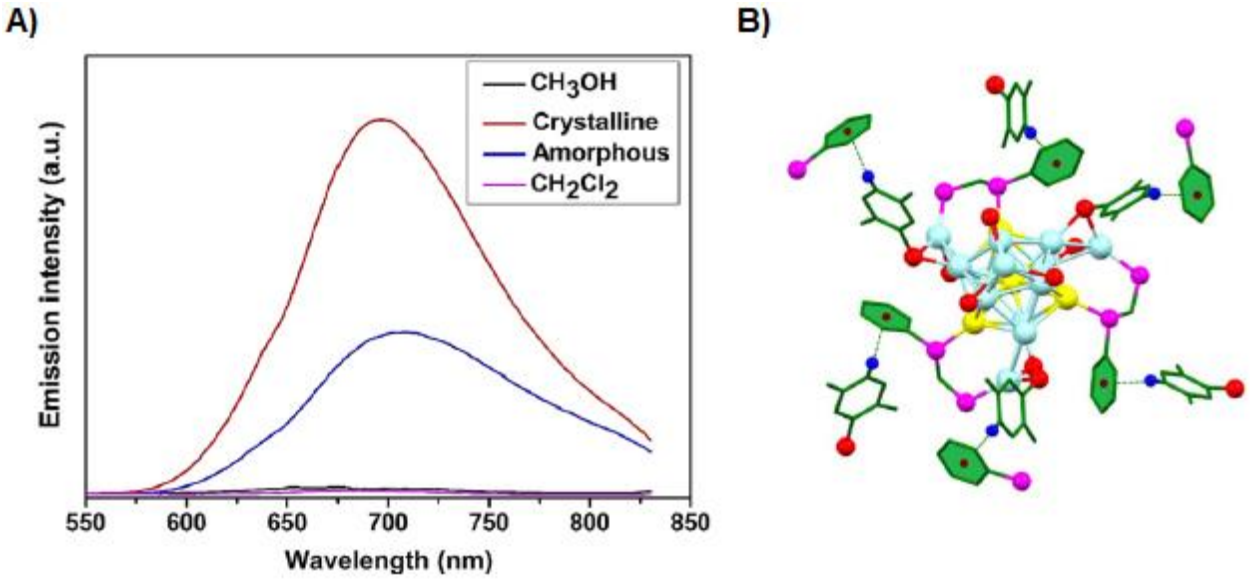


Figure 1.3 A) Emission intensity spectra for $Au_4Ag_9(DPPM)_3(2,5\text{-}DMBT)_9$ in different solid states. B) CH-π interactions between $Au_4Ag_9(DPPM)_3(2,5\text{-}DMBT)_9$ clusters that are proposed to promote increase emission intensity in the crystalline state. Figures reproduced from Chen *et al.*[80]

1.4 Thesis Scope

The work presented herein seeks to improve understanding and control over surface ligand layers on gold nanoclusters. Chapter two probes the evolution of site-selective ligand exchange over time and contextualizes these results in terms of ligand dynamic

processes. Chapter three introduces the first methodology for acetylide-for-thiolate exchange and offers preliminary investigations into the stability of acetylide ligands relative to thiolate ligands. Chapter four explores the stability of gold nanoclusters in catalytic conditions by determining exchange products involving reactants and/or products of the reaction. Finally, chapter five represents the first foray into selective crystallization of different conformational polymorphs and affords insight into the potential impact of surface dynamics on reactions at nanocluster surfaces and the induction of new material properties. By addressing these questions and challenges, we seek to move closer to the goal of developing methodology that can create controlled, robust ligand layers that can be tailored for directed applications.

CHAPTER 2: REGIOCHEMISTRY OF THIOLATE FOR SELENOLATE LIGAND EXCHANGE ON GOLD CLUSTERS*

2.1 Synopsis

Previous investigations into site-selectivity in ligand exchange reactions revealed positions where exchange is kinetically favorable. Thiolate ligand layers have been shown to evolve over time, however, leading to potential isomerization of the nanocluster surface. Additionally, bias in the results might arise from selective crystallization of specific compounds in a mixture. To address these questions, we investigate a selenolate-for-thiolate exchange reaction over time using x-ray crystallography. The steric factors of the incoming and outgoing ligands in this reaction are nearly identical, reducing concerns over selective crystallization. Overall, we observe a much more complex set of results that represent isomerization of exchange positions over time, changes in solvent accessible locations, and varying selectivity trends depending on the degree of exchange.

2.2 Introduction

Ligand exchange is a fundamental reaction of inorganic nanoparticles and nanoclusters. Such reactions are used widely for bio-labeling,[66,67,87–89] functionalization of na[1]noparticles into theranostics,[90,91] and the processing of inorganic semiconductor colloids for solar cell applications.[92–94]

For ligand exchange on thiol protected gold nanoparticles, the seminal work of Murray established multiple kinetic exchange environments, implying differential ligand

* The work presented here is published in *Journal of the American Chemical Society*. Christopher A. Hosier's contributions include project planning, experimental design, data gathering and interpretation, and preparation of the manuscript. *J. Am. Chem. Soc.* **2019**, *141*, 309. © 2019 American Chemical Society

reactivates.[12] Such differential reactivities imply the prospect of regiochemical control of incoming ligand placement on nanoparticle surfaces. Confounding the prospect of regiochemical control are the possibilities of ligand fluxionality and/or isomerization under normal handling conditions. To this end it is worth noting that the barrier to stereoisomerization is low,[95] that inter-particle ligand exchange occurs apparently readily,[75] and that there is some evidence that ligands may translate within the surface of a particle.[96,97] It is unclear under which conditions translation of ligands across the surface of a particle may occur—or if events assumed as translation may actually arise from inter-particle exchange—as some reports show that ligand translation events occur on the same time scale as ligand dissociation events (which are slow at ambient lab-temperatures).[98]

Previously, we examined ligand exchange from a structural standpoint, solving single-crystal structures of $Au_{102}(pMBA)_{44}$ and $Au_{25}(PET)_{18}$ after ligand exchange with *p*-bromobenzethiol (pBBT).[26,27] These crystal structures revealed ligand exchange occurring at a limited number of ligand positions (accounting for 4 of 22 ligands for Au_{102} and 2 of 18 ligands for Au_{25}). These crystal structures were solved after very short time-scale ligand exchange reactions and may correspond to sites that are kinetically fast for exchange. Because the steric shapes of the incoming and outgoing ligands are different, there is some concern that our previous results were biased towards those ligand exchange products that form crystals, excluding some products from our analysis.

Herein we structurally study exchange of selenolates for thiolates on $Au_{25}(SeR)_{18}$ by single crystal X-ray. In this case, we exchanged benzenethiolate for benezeneselenolate. The identical R group relieves concern about selective crystallization biasing our results.

We solved a total of 13 structures, corresponding to 2 different amounts of incoming ligand, and 3 different time points. Overall, we observe a much more complicated ligand exchange process. The distribution of ligands across different sites is broader than in our previous short-time-scale experiments. Based on this distribution, we see evidence for associative ligand exchange, inter-cluster ligand exchange, and a different regiochemical preference for selenolate ligands versus thiolate ligands.

2.3 General Methods

$Au_{25}(SePh)_{18}$ was synthesized from $Au_{25}(PET)_{18}$ and HSePh through a previously reported selenol for thiol complete exchange method.[74] The $Au_{25}(SePh)_{18}$ was validated by mass spectrometry (figure A.1). To this $Au_{25}(SePh)_{18}$ cluster, we added either 1 or 100 equivalents of benzeneselenol. Ligand exchange was allowed to progress for 30 minutes prior to quenching ligand exchange by addition of methanol, which precipitates the $Au_{25}(SR)_{18}$ clusters but in which free ligand is soluble. The isolated $Au_{25}(SR)_{18}$ clusters were washed extensively in methanol to remove any remaining ligand. Crystallization proceeded by the methods described in the materials and methods section in appendix A.

Under the crystallization conditions used, approximately 5 days elapsed at room temperature before crystals became apparent. This time and temperature may allow additional reactions to occur, such as inter-cluster ligand exchange and intra-cluster ligand translation. In order to gain insight into the dynamics of post-ligand exchange reactions, we dissolved a sub-set of the crystals formed after 5 days and re-crystallized that material. Again, 5 days at room temperature were required before additional crystals were observed. Thus, these $Au_{25}(SR)_{18}$ clusters had ~10 days of time for inter- and intra-

cluster ligand dynamics to manifest. A second recrystallization was executed for the 100 equivalent ligand feed reaction. Crystals resulting from this contain $Au_{25}(SR)_{18}$ that had ~15 days at room temperature to manifest intra- and inter-cluster ligand dynamics.

We collected single-crystal diffraction data on Advance Light Source beamline 4.2.2. Full details of data collection are given in appendix A. The raw diffraction images were integrated and processed using XDS[99] and XPREP (version 6.12; Bruker AXS: Madison, WI, 1999), and structure refinement was performed using SHELX.[100] The extent of ligand exchange at any given ligand position was determined through a static substitutional disorder refinement at each chalcogen atom position. Occupancies less than 4% were considered negligible for the purposes of our analysis, consistent with practice.[28] To describe the location and extent of ligand exchange in any given ligand position on $Au_{25}(SR)_{18-x}(SeR)_x$, we adopt the convention proposed by Pradeep and colleagues.[101] In this convention, the semiring units surrounding the core of Au_{25} are considered as a set of 3 interlocked Borromean rings (Figure 2.1). Each gold atom and chalcogen atom (e.g. ligand position) is given a unique identifier, which is independent of any symmetry. A symmetry-independent description of each ligand is important in our work as 11 of our structures show no symmetry.

Following the convention, we identify each of the 18 unique ligands by two numbers: the first number delineates on which of the 6 semiring units any ligand sits. The second number delineates the site of the chalcogen atom (e.g. ligand site). Each semiring unit is comprised of 3 ligands and 2 Au(I) atoms in alternating order. By convention, these are numbered 1 through 5 in clockwise order. Thus, the unique location of any ligand on the cluster is described. For example, ligand D2-3 is the ‘apex’ ligand of the second semiring

unit, whereas D2-1 and D2-5 are the 2 ‘core’ ligands on the second semiring unit. Note that D2-2 and D2-4 are the Au(I) atoms in the second semiunit and represent sites of ‘attachment’ for incoming ligands in associative exchange mechanisms.

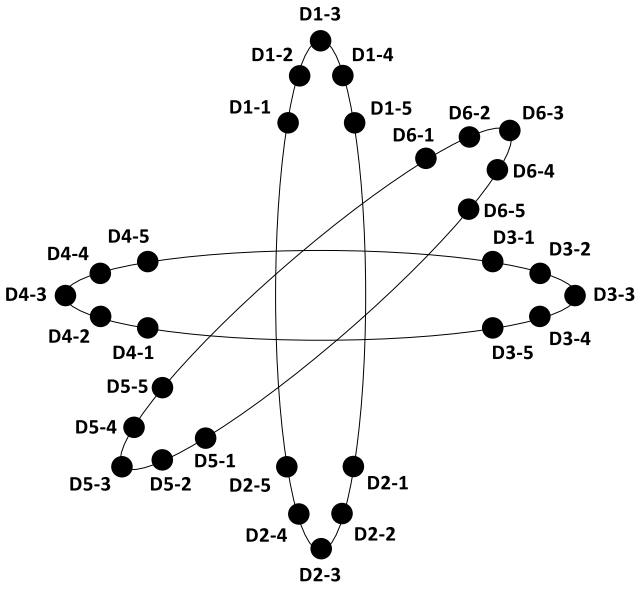


Figure 2.1. Numbering of ligands and Au(I) atoms in each semiring.

In order to compare ligand positions across a set of polymorphic structures, the structures were oriented against each other through visual inspection. Solvent accessibility values were calculated in PyMOL using a probe radius of 1.80 Å corresponding to the van der Waals radius of sulfur.

2.4 1:1 SPh:Au_{25} Ligand Exchange Results

We solved three crystal structures where crystals were observed 10 days after initiating crystallization. These crystal structures were dissimilar, revealing heterogeneity in ligand exchange reactions. We observe exchange at between 9 and 12 ligand positions, and a composite average of 11 ligand positions. An example composite structure is shown in figure 2.2A, colored with the non-exchanging ligand positions in red

(indicating Se) and exchanging positions colored in yellow (indicating S). The set of 3 crystal structures is summarized in Table 2.1A, entries 1 - 3.

On average, incoming (thiolate) ligands exchange appear preferentially at apex positions on the cluster (9.4% average occupancy vs. 5.2% average occupancy). Incoming ligands are observed at a minimum of 5 apex sites, with one structures showing incoming ligand density at all 6 apex sites. This contrasts the ligands bound to the icosahedral core as structures show between 4 and 8 non-exchanging sites. Overall, this distribution of incoming ligands implies a mechanistically different route for ligand exchange than observed in prior ligand-exchange structures.

Three more crystal structures were solved of $Au_{25}(SR)_{18-x}(SeR)_x$ clusters that had 15 days to react prior to observation of crystals. In this set of crystals, we observed an increase in the number of exchanging positions. Incoming ligand occupancy was between 11 and 14 positions, with a composite average of 13. Notably, the sum-total of ligands exchanged at 10 days and 15 days, as determined by a total sum-of-occupancies is essentially constant, at 1.20 and 1.29 ligands per cluster, respectively. Those results show a larger envelope of ligand distribution for the 15 day exchange relative to the 10 day exchange (figure 2.2). The preference for apex positions is maintained, but less so that in the 10 day sample, with an average of 8.8% occupancy across all apex sites and 6.3% across all core sites.

We attempted to understand the selectivity of ligand exchange by calculating the solvent exposed surface area of gold atoms bonded to exchanging ligands. Previous structural studies of ligand exchange conducted at comparatively short time periods (after 5 minutes of ligand exchange) showed incoming ligand occupancy as completely

correlated with solvent exposure of bonded gold atoms. This is consistent with associative ligand exchange mechanisms. In the present work, the correlation between exchange and solvent exposure of bonded gold atoms is not as robust (table 2.1)

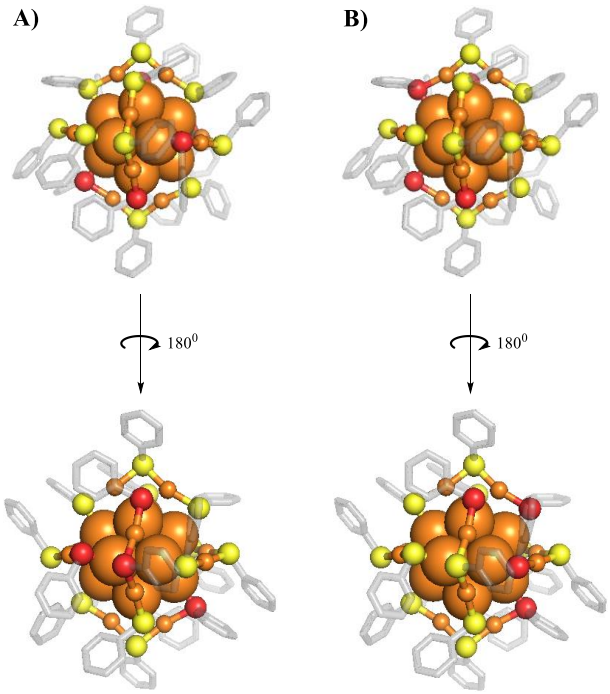


Figure 2.2. 1 eq. PhSH exchange after A) 10 days and B) 15 days. Yellow atoms indicate positions where partial exchange occurs and red atoms indicate positions where no exchange occurs. Orange atoms represent gold atoms and gray sticks represent bonds to carbon. Hydrogen atoms and counterion atoms have been omitted for clarity

At 10 days of crystallization time, we observe evidence of exchange for 20 of 30 ligands (66.7%) bonded to solvent exposed gold atoms across 3 structures. This compares to 45% (11 of the 24) of the ligands bonded to gold atoms with no solvent exposure. At 15 days of reaction time, we observe 20 of 30 solvent exposed gold atoms facilitate exchange (66.7%) and 18 of 24 (75%) of the solvent buried ligands exchange. Structural analysis at 5 days was not performed as the crystals did not yield reliable structures.

Table 2.1. Solvent accessibility of gold atoms connected to each ligand position in 1 eq. PhSH crystal structures at A) 10 days and B) 15 days. All area values are in $Å^2$. Positions highlighted in green exhibit partial ligand exchange.

A)

	Crystal 1	Crystal 2	Crystal 3
D1-1	0.231	0.116	0.231
D1-3	0.231	0.116	0.231
D1-5	0	0	0
D2-1	0	0	0
D2-3	0.100	0.100	0.045
D2-5	0.100	0.100	0.045
D3-1	0	0	0
D3-3	1.263	1.320	1.263
D3-5	1.263	1.320	1.263
D4-1	0	0	0
D4-3	0.449	0.563	0.393
D4-5	0.449	0.563	0.393
D5-1	0.362	0.362	0.419
D5-3	0.362	0.362	0.419
D5-5	0	0	0
D6-1	0	0	0
D6-3	0	0	0
D6-5	0	0	0

10 Days

B)

	Crystal 1	Crystal 2	Crystal 3
D1-1	0.175	0.175	0.242
D1-3	0.175	0.175	0.242
D1-5	0	0	0
D2-1	0	0	0
D2-3	0.045	0.210	0.109
D2-5	0.045	0.210	0.109
D3-1	0	0	0
D3-3	1.263	1.263	1.146
D3-5	1.263	1.263	1.146
D4-1	0	0	0
D4-3	0.393	0.562	0.449
D4-5	0.393	0.562	0.449
D5-1	0.362	0.362	0.372
D5-3	0.362	0.362	0.372
D5-5	0	0	0
D6-1	0	0	0
D6-3	0	0	0
D6-5	0	0	0

15 Days

2.5 100:1 SPh:Au_{25} Ligand Exchange

In addition to the 1:1 incoming ligand ratio, we examined crystals formed in otherwise identical experimental conditions with a 100-fold incoming ligand to $Au_{25}(SeR)_{18}$ ratio. We solved structures of 3 crystals that first formed after 5 days post-exchange reaction, 2 crystals that formed after 10 days and 2 crystals that formed after 15 days. In the 5-day post-exchange crystals, we observe evidence of ligand exchange in 14, 15 or 16 ligand positions. In the 10-days post exchange crystals, we observe evidence of ligand exchange in 12 and 13 ligand positions. In the 15 day post-exchange crystals, we observed evidence of ligand exchange at 10 and 12 ligand sites. Summing the percent occupancy of all ligands in all structures reveals that an average of 2.59 incoming ligands were incorporated into these structures. These results are shown tabular form in table 2.2. An example rendering of the exchanged products is shown in Figure 2.3. A higher

variation in number of exchanged ligands is observed between these structures relative to the 1:1 SPh:Au25 structures, with ranges of 0.95 and 0.22 ligands respectively. The structures at 15 days exhibit similar degrees of exchange (2.33 and 2.30 ligands) to several of the structures at 5 days (2.17, 2.40, and 2.84 ligands), however, suggesting a similar consistency over time.

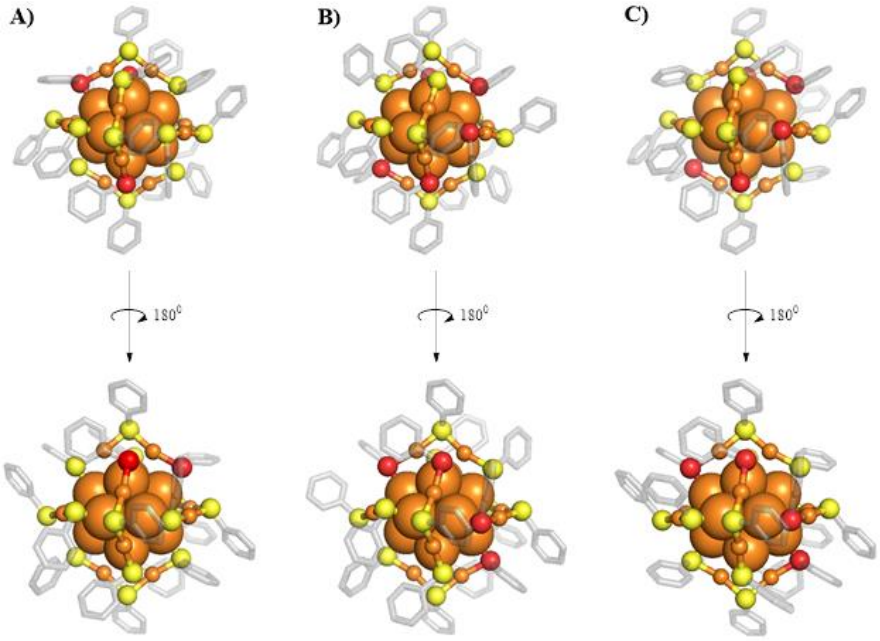


Figure 2.3 100 eq. PhSH exchange after A) 5 days, B) 10 days, and C) 15 days. Yellow atoms indicate positions where partial exchange occurs and red atoms indicate positions where no exchange occurs. Orange atoms represent gold atoms and gray sticks represent bonds to carbon. Hydrogen atoms and counterion atoms have been omitted for clarity.

At this higher feed ratio, we observe a very strong preference for incoming thiolate ligand occupancy at the apex positions as compared to core position. After 5 days, 10 days, and 15 days we observe incoming thiolate ligand in all 6 apex sites in each structure, but only 75%, 54% and 42% of core sites. Furthermore, the apex sites reflect a higher average occupancy (average of 26.9% in the substitutional refinement) than the core sites (8.2%). We observe ligand exchange at 83% of solvent exposed Au(I) atoms

and 83% of solvent buried Au(I) atoms at 5 days, exchange at 83% of exposed Au(I) atoms and 58% of solvent buried Au(I) atoms at 10 days, and exchange at 83% of solvent exposed Au(I) atoms and 17% of solvent buried Au(I) atoms at 15 days

Table 2.2 Solvent accessibility of gold atoms connected to ligand positions in 100 eq. PhSH exchanged crystal structures at A) 5 days, B) 10 days, and C) 15 days. All area values are in $Å^2$. Positions highlighted in green exhibit partial exchange.

A)

	Crystal 1	Crystal 2	Crystal 3
D1-1	0.302	0.242	0.242
D1-3	0.302	0.242	0.242
D1-5	0	0	0
D2-1	0	0	0
D2-3	0.045	0.045	0.045
D2-5	0.045	0.045	0.045
D3-1	0	0	0
D3-3	0.965	1.310	1.146
D3-5	0.965	1.310	1.146
D4-1	0	0	0
D4-3	0.282	0.506	0.282
D4-5	0.282	0.506	0.282
D5-1	0.306	0.362	0.250
D5-3	0.306	0.362	0.250
D5-5	0	0	0
D6-1	0	0	0
D6-3	0	0	0
D6-5	0	0	0

5 Days

B)

	Crystal 1	Crystal 2
D1-1	0	0
D1-3	0	0
D1-5	0	0
D2-1	0	0
D2-3	0	0
D2-5	0	0
D3-1	1.548	1.615
D3-3	2.767	2.778
D3-5	1.219	1.163
D4-1	0	0
D4-3	0.165	0.222
D4-5	0.165	0.222
D5-1	0	0.115
D5-3	0.116	0.29
D5-5	0.116	0.175
D6-1	0	0
D6-3	0	0.061
D6-5	0	0.061

10 Days

C)

	Crystal 1	Crystal 2
D1-1	0.117	0.191
D1-3	0.117	0.191
D1-5	0	0
D2-1	0.117	0.191
D2-3	0.117	0.191
D2-5	0	0
D3-1	0	0
D3-3	0.061	0.397
D3-5	0.061	0.397
D4-1	0	0
D4-3	0.061	0.397
D4-5	0.061	0.397
D5-1	0	0
D5-3	0.244	0.056
D5-5	0.244	0.056
D6-1	0	0
D6-3	0.244	0.056
D6-5	0.244	0.056

15 Days

2.6 Discussion

Compared to our previous work, which appeared to capture short-time-scale kinetic products of exchange, this work appears to capture products closer to a thermodynamic equilibrium. In fact, we can take the 3 observational time points as snapshots of ligand shell evolution en route to a thermodynamically preferred ligand arrangement. This work is fundamentally different than our previous work on thiolate-for-thiolate exchange in that here we are studying thiolate-for-selenolate exchange. This means that kinetic vs. thermodynamic products of preferential selenolate and thiolate positions may be

observed herein, as well as how preferences for positions of these may change when there is more or less selenium or thiol in a cluster ligand shell.

One trend that is clear is that when ~3 thiolate ligands are incorporated, the thiolate ligands show a strong preference for the apex positions. It may be the case that the differing bond strengths for Se-Au(0), Se-Au(I), S-Au(0) and S-Au(I) sort the S atoms into core positions when one incoming ligand is incorporated,[102,103] whereas geometric constraints related to preferred bond lengths and atomic radii tend to favor sulfur in the apex positions when more than one thiolate ligand is incorporated into a cluster.[104,105] The idea here is that the larger atomic radius of Se and longer Se-Au(I) bond lengths favor S in apex positions more strongly as more S is incorporated. There is also the possibility that we are observing a kinetic phenomenon, wherein core ligands exchange first with ligands in solution, and apex ligands exchange later in an inter-cluster reaction. In this regime, the stronger S-Au(I) bond length places S preferentially at apex positions, and the kinetics of this observation are accelerated with the inclusion of 100-fold more ligand. Furthermore, there might be a preference for specific ligands to aggregate after initial exchange as this behavior has been observed on gold nanoparticles.[106] Stellacci and co-workers observed that exchanged ligands were evenly distributed on the nanoparticle surface. Over time the exchanged ligands aggregated near one another, creating an uneven, “patchy” distribution. It is possible a similar pattern might be occurring in this work due to differences in the chalcogen atom utilized in the two ligand types.

In the set of 13 crystal structures solved, we observe 3 crystallographic polymorphs. These differ from each other most notably in ligand conformation. These polymorphs reveal some sampling of the ligand conformational space, as well as provide some

interesting observations on new crystallographic symmetries for this well-studied cluster. Conformational variability of thiolate ligands on gold clusters has been observed experimentally and investigated theoretically.[77,107] One theoretical investigation suggests an energetic barrier of 10 kcal/mol, suggesting fairly free movement at room temperature.[108] Here we make an additional experimental observations of conformational space sampling. Specifically, we observe ligands D3-1, D5-5, and D6-5 occupying multiple conformations across the set of crystal structures.

This conformational variability observed in the ligand shell suggests that as many as 17 of the 18 ligands are bonded to Au(I) atoms that have some at least transient solvent exposure. While a maximum of 10 ligands are attached to solvent exposed Au(I) atoms in any individual structure, the movement of ligands may open up all but 1 ligand to exchange through some manner of associative exchange. As in previous experimental reports of the conformational space sampled by aromatic ligands on gold clusters, we observe only a limited set of conformers compared to what is theoretically possible.[77] It is possible that utilizing different synthetic conditions such as solvent choice could lead to a preference for other conformers and consequently impact ligand migration behavior.

While this analysis of solvent exposure focuses on potential associative-type exchange of solvated ligands with cluster bound ligands, the observation that the ligand distribution across clusters changes over time suggests that there are additional processes we are observing in these crystal structures. Recent work has highlighted the facile nature of both inter-particle ligand exchange and inter-particle metal exchange.[13,76] These processes can be remarkably fast in the case of interparticle metal exchange. The ligand distributions that continue to change some time after ligand exchange is ceased

are consistent with previous reports that suggest that ligand exchange into the 'apex' positions of clusters is mediated by inter-cluster reactions.[75]

All icosahedral Au_{25} crystal structures so-far reported contain an inversion symmetry element at the centroid of the cluster.[23,27,58,104,105,109,110] In 2 of the 3 polymorphs reported here, the arrangement of ligands in the ligand shell breaks the inversion symmetry. In all other previously published crystal structures, semirings D1 and D2 represent are related by inversion symmetry, as well as semirings D3/D4 and D5/D6. In all of the 5 and 10 day crystal structures reported here, we observe that ligands D5-5 and D6-5 are not related by inversion symmetry. Likewise, ligands D3-1 and D4-1 are not related by inversion symmetry. This observation has possible implications for the spectroscopic nature of icosahedral Au_{25} (or crystals thereof) in nonlinear spectrosocopy.

In previous papers we noted that selective crystallization of a limited set of the products of ligand exchange could bias our interpretation.[27] Explicitly, when using 4-bromo-benzenethiol as the incoming ligand in these reactions, exchange of that ligand into some positions could disrupt crystal-contacts and prevent crystallization. In this work, the crystal contacts are all mediated by identical aromatic ligand groups, which do not change after ligand exchange. Thus, the wider distribution of ligand positions we observe in these structures may be a better representation of the ligand exchange reaction than our previous work. That this work differs in that it is longer time scale, greater feed ratios of incoming ligand, and exchanging thiol for selenol makes direct comparison to our previous work less straightforward.

In conclusion, we solved 13 crystal structures of $Au_{25}(SeR)_{18-x}(SR)_x$ where x is variable and depends upon ligand feed and reaction time. In shorter time scale reactions,

we observed some preference for exchange mediated by solvent exposed Au atoms. For the first time, we observe ligand exchange of ligands that are not attached to solvent exposed Au atoms as well. We observe increasing exchange at solvent-buried positions over time when 1 equivalent of thiophenol is used per cluster and decreasing exchange at solvent-buried positions when 100 equivalents of thiophenol is used. We observe a preference for sulfur at ‘apex positions’ and selenium at ‘core positions’ that emerges in the longest time point and highest ligand feed crystal structures. Several different ligand conformations are noted in these structures, with many of them lacking symmetry within the cluster. Overall, several new structural ligand exchange phenomena are observed in this work.

CHAPTER 3: ACETYLIDE-FOR-THIOLATE EXCHANGE ON GOLD CLUSTERS

3.1 Synopsis

While an increasing number of acetylide-protected gold nanoclusters have been synthesized, there are few reports where gold clusters are post-synthetically functionalized with acetylides. In particular, acetylide-for-thiolate exchange has yet to be reported despite the ubiquity of thiolate-protected nanoclusters and calculations suggesting gold-acetylide bonds are stronger relative to gold-thiolate bonds. Herein, we utilize a gold(I)-acetylide complex to generate acetylide-for-thiolate exchange. Free alkyne is unable to undergo exchange on the nanocluster regardless of the presence of an exogenous base, indicating the necessity of using a pre-formed gold complex. We show that intercluster exchange can occur between homoleptic acetylide-protected and thiolate-protected clusters and that acetylide-protected clusters can undergo exchange with free thiols. These results overall indicate that acetylide-protected nanoclusters are not inherently more stable than thiolate-protected nanoclusters and that gold-acetylide bonds might be weaker than calculations suggest.

3.2 Introduction

Soluble inorganic nanoclusters and nanoparticles are typically stabilized or protected by a passivating ligand shell. Ligand exchange is a fundamental reaction of such systems, and the interaction strength of ligand with metal can underlie and/or define kinetics, thermodynamics, and regiochemistry of ligand exchange. Because the ligand shell determines nanoclusters or nanoparticle solubility, stability, and reactivity, ligand exchang

reactions can enable functionalization of metal clusters/nanoparticles for their use in bioimaging, catalysis, theranosticsc, and sensing applications.

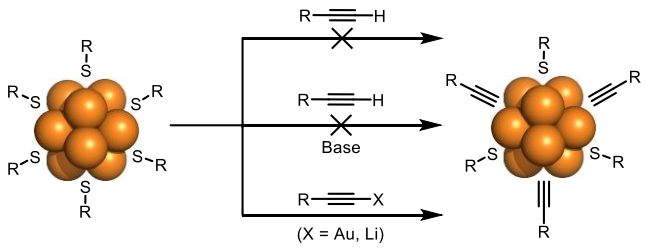
Thiolate-protected gold nanoclusters have received substantial interest over the past two decades due to their ease of synthesis and overall stability. Recent work has highlighted the propensity for rapid exchange of metal atoms and/or ligands between dissolved thiolate-protected coinage metal clusters. Furthermore, thiolate-protected clusters are unstable to oxidative conditions.

Whereas thiolate-protected gold clusters represent a now very well-defined class of atomically precise inorganic nanoparticles, gold nanoclusters ligated with organometallic ligands such as acetylides and *N*-heterocyclic carbenes have emerged only recently as alternatives that may present improved stability and/or catalytic properties. Acetylides in particular attract interest as robust ligands for protecting gold nanoclusters. Such clusters are suggested as more stable than the widely studied thiolate-protected clusters, with calculations suggesting that acetylide-gold bonds are stronger by 6 to 52 kcal/mol than thiolate-gold bonds. Acetylide gold surfaces show more consistent conductance measurements, are less susceptible to oxidation, and maintain similar packing densities compared to thiolate-coated surfaces. Furthermore, higher catalytic conversion efficiencies have been reported when using acetylide ligands on a gold nanocluster, and the ability for acetylides to adopt different binding motifs on cluster surfaces can potentially produce new properties in previously studied clusters.

Synthesis of acetylide-protected clusters proceeds most often by reduction of Au(I)-acetylide complexes. Only two examples of post-synthetic acetylide exchange on gold nanoparticles are so-far reported: Tsukuda and co-workers demonstrated that *N*-

vinylpyrrolidone-protected clusters undergo exchange with free phenylacetylene to afford a series of homoleptic phenylacetylide-protected clusters, and Konishi later showed acetylide-for-chloride exchange by using free phenylacetylene in the presence of a base. Examples of acetylide-for-thiolate exchange reactions and/or the reverse reaction are so-far unreported.

Herein, we reveal acetylide-for-thiolate and thiolate-for-acetylide exchange on gold nanoclusters for the first time. We provide insight into the nature of exchange by observing success or failure of exchange with different acetylide derivatives and/or reaction conditions (scheme 3.1). Overall, we find that forward exchange, reverse exchange, and interparticle ligand exchange are all facile reactions provided incoming ligands are suitable.



Scheme 3.1 Current reaction scheme.

The most straightforward reaction attempted—exchange between thiolate-protected clusters (e.g.-$Au_{25}(SR)_{18}$ in our studies) and soluble phenylacetylene—resulted in no reaction. The reaction failed in all tested incoming ligand concentrations (up to a 100-fold molar excess of phenylacetylene), temperatures (up to 60 °C attempted), and in the presence of an exogenous base (figures B.4-B.7). However, when phenylacetylene is introduced as a gold(I) or lithium phenylacetylide complex, exchange is successful in mild conditions. Figure 3.1 shows MALDI-MS spectra of phenylacetylide (PA) for phenylethanethiolate (PET) exchange after 30 minutes when gold(I)-phenylacetylide is

added in 1 or 10 equivalents to solutions containing $Au_{25}(PET)_{18}$. The distribution of exchange products increases with time and eventually results in a Gaussian-like distribution commonly observed in partial exchange reactions (figure B.8).

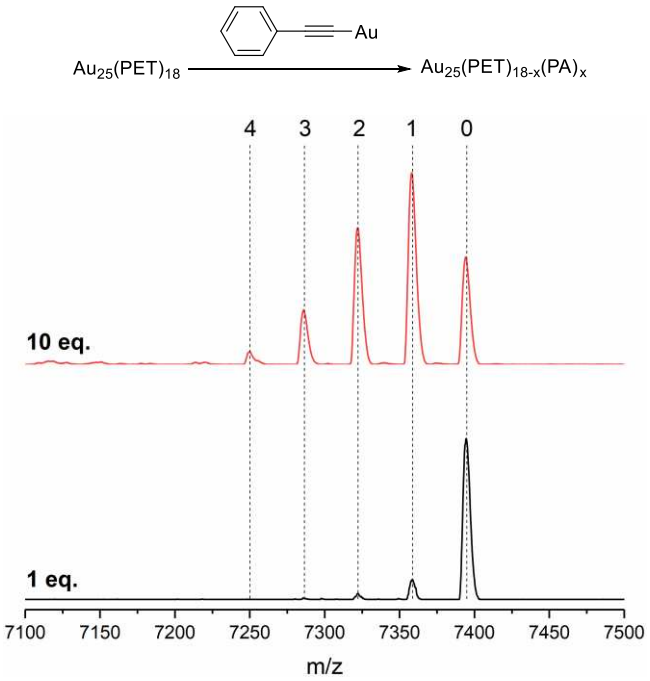


Figure 3.1 Positive ion MALDI mass spectra of the resulting $Au_{25}(PET)_{18-x}(PA)_x$ from reacting $Au_{25}(PET)_{18}$ with 1 and 10 equivalents of gold(I)-phenyacetylide.

To determine the extent of exchange that can be obtained, we reacted 100 equivalents of gold(I)-acetylide with $Au_{25}(PET)_{18}$ for 18 hours. While MALDI-MS shows a large distribution of products, we observe a peak at 6744.34 m/z, corresponding closely to the calculated mass of 6744.47 g/mol for $Au_{25}(PA)_{18}$ (figure B.9). This suggests an exchange-based synthetic route to a recently reported homoleptic acetylide-protected gold cluster, $Au_{25}(CCAr)_{18}$, which was synthesized by reduction of gold(I)-acetylide precursors. We have not attempted isolation of this specific compound at this time due to the apparent large number of competing exchange products.

This result differs somewhat from a recent report by Wang where addition of a gold(I)-phenylacetylide derivative to bis-phosphine-protected $Au_9(BINAP)_4$ resulted not in exchange but in addition of gold(I)-phenylacetylide complex to the cluster. Differences in the nature of the initial ligand layer (i.e.-monodentate ligands v. bidentate ligands, phosphines v. thiolates) between the clusters in the current reaction and the cluster in the reported reaction may account for this difference in reactivity.

We observe that lithium phenylacetylide, like gold(I)-phenylacetylide, is a competent ligand source for exchange with $Au_{25}(PET)_{18}$. Exchange of lithium phenylacetylide onto $Au_{25}(PET)_{18}$ in mild conditions is shown in figure B.10. Notably, only the acetylide and thiolate ligands exchange in this case as no masses corresponding to lithium-for-gold exchange were observed. Thus, the role of gold in the gold(I)-phenylacetylide-based exchange for thiolates is likely as a spectator and not a participant in the exchanging unit.

We also examined the reverse reaction, specifically the exchange of thiolates onto $Au_{44}(PA)_{28}$ (figure 3.2). Synthesis of this cluster is found in the supporting information. MALDI-MS reveals exchange after simple mixing of thiolates at room temperature with the $Au_{44}(PA)_{28}$ cluster, even at a short time scale. This result contrasts a previous report by Zheng and co-workers where addition of a similar amount of free thiol to the $Au_{24}Ag_{20}(2\text{-Spy})_4(PA)_{20}Cl_2$ cluster results only in thiolate-for-halide exchange and not in thiolate-for-acetylide exchange. The difference between these results and the results reported herein may be attributed to differences in metal doping (single metal versus mixed), ligand identities (homoleptic versus mixed ligand layers, aliphatic thiolate versus aromatic thiolate), or acetylide binding motifs (μ^2 versus μ^3).

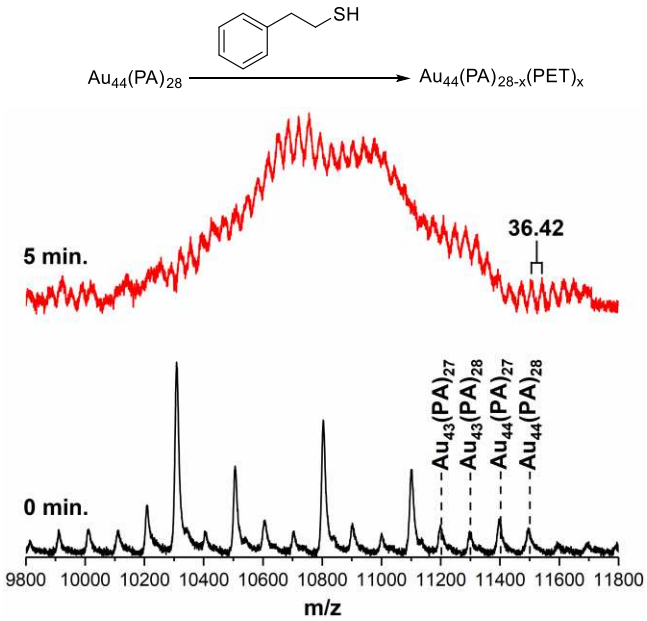


Figure 3.2 Positive MALDI mass spectrum of the reaction between $Au_{44}(PA)_{28}$ and PET. The parent peak of $Au_{44}(PA)_{28}$ and several fragmentation products are labelled in the spectrum for the starting material. The remainder of the peaks correspond to additional fragmentation of these compounds. In the spectrum corresponding to the reaction after five minutes, the average distance between peaks is 36.42 m/z. The calculated mass difference between PA and PET is 36.09 m/z.

Recent works by Pradeep and Bürgi have demonstrated that thiolate-protected gold clusters readily undergo intercluster exchange of ligands. As such, we attempted to determine if intercluster exchange occurs between thiolate- and acetylide-protected clusters. Multiple intercluster ligand exchange products derived from $Au_{25}(PET)_{18}$ and $Au_{44}(PA)_{28}$ are observed within five minutes of mixing, indicating that thiolate-for-acetylide intercluster exchange is a similarly facile process like thiolate-for-thiolate intercluster exchange (figure 3.3).

Combined, the failure of phenylacetylene-for-thiolate exchange with the success of thiolate-for-acetylide, lithium phenylacetylide-for-thiolate and gold(I) phenylacetylide-for-thiolate exchanges suggest that the net exchange reaction may be described as a metathesis reaction involving cluster, thiolate, acetylide, and hydrogen. Three versions of

this metathesis reaction are shown in scheme 3.2. Net bond enthalpies for each metathesis reaction can help rationalize observed reaction successes and failures. Given that the carbon-hydrogen bond in an alkyne is 46 kcal/mol stronger than the sulfur-hydrogen bond and that computational results suggest that gold gold-alkynyl bond is 6-20 kcal/mol stronger than the gold-thiolate bond, the enthalpic favorability of the overall metathesis reaction accounting for thiol-for-acetylide exchange is between -26 and -40 kcal/mol. The reverse reaction of phenylacetylene exchanging onto thiolate-protected clusters becomes enthalpically unfavorable by the same value.

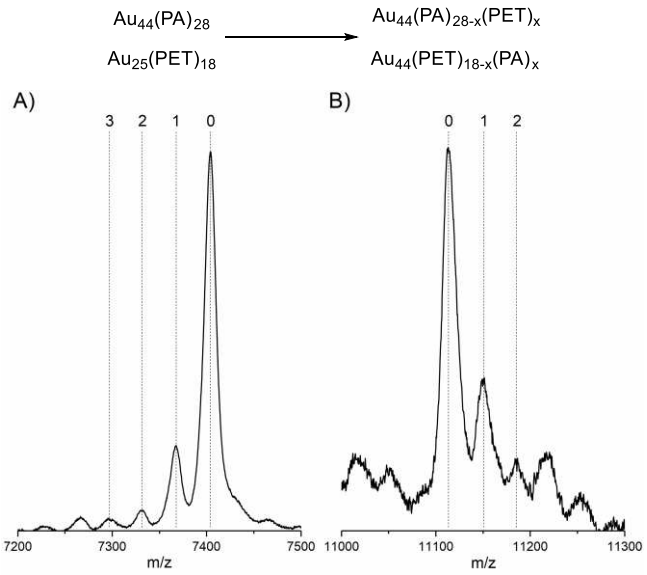
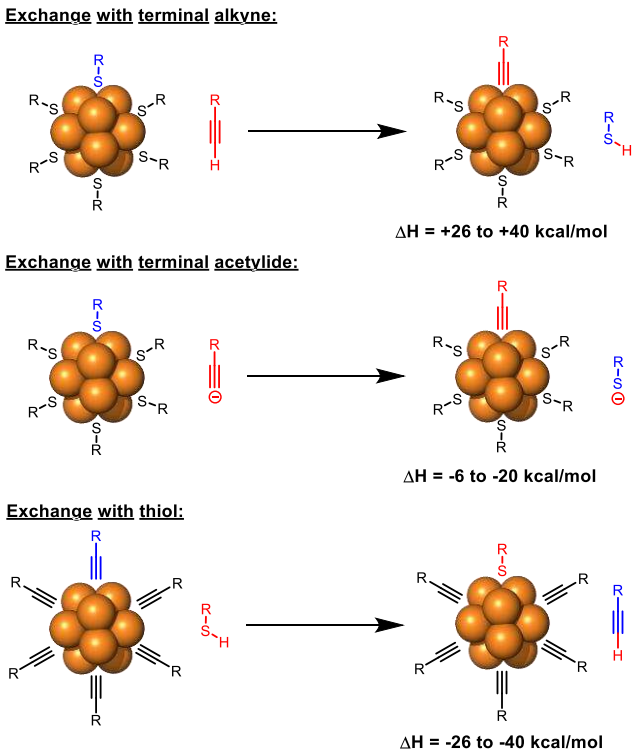


Figure 3.3 Positive ion MALDI mass spectrometry results of A) $Au_{25}(PET)_{18-x}(PA)_x$ and B) $Au_{44}(PA)_{28-x}(PET)_x$ after mixing $Au_{25}(PET)_{18}$ with $Au_{44}(PA)_{26}$ for 5 minutes, where x is equal to the number of ligands exchanged.

The bond enthalpies of lithium-acetylide and gold(I)-acetylide are presently unknown. However, the success of the metathesis reaction with thiolate-protected clusters when these are used as incoming ligands suggests that the bond enthalpies are much weaker than the hydrogen-alkyne enthalpy.

Overall, we report herein the apparent criteria for successful incorporation of acetylides into thiolate-protected clusters. The present work suggests that acetylide-protected clusters are more susceptible to exchange with thiolates than previously assumed and/or computationally predicted, and that intercluster exchange of thiolate-for-acetylide ligands is also spontaneous at room temperature. Some of these results may be rationalized by considering reactions as metathesis reactions rather than exchang reactions.



Scheme 3.2 Balanced reactions and net change in bond energies for exchange reactions with terminal alkynes, terminal acetylides, and thiols.

CHAPTER 4: LIGAND EXCHANGE OF NON-INNOCENT REACTANTS AND PRODUCTS WITH $Au_{25}(PET)_{18}$ IN THIOETHER OXIDATION REACTIONS

4.1 SYNOPSIS

Gold nanoclusters are reported to be stable and recyclable catalysts that can be used to oxidize thioethers into sulfoxides. However, gold has been shown to promote the breaking and forming of carbon-sulfur bonds. Additionally, the use of dimethyl sulfoxide as a solvent has been shown to increase catalytic activity in one case. In this work, we demonstrate that gold nanoclusters undergo ligand exchange with species present in thioether oxidation reactions. One exchange process appears to derive from the cleavage of carbon-sulfur bonds. This has only been observed once before with the use of gold nanoclusters. We also observe the first reported evidence of a sulfoxide ligand on a gold nanocluster, suggesting that sulfoxide-gold interactions are stronger than currently believed. Overall, these results indicate the gold nanoclusters are unstable in the catalytic reaction conditions.

4.2 INTRODUCTION

Structurally precise gold nanoclusters have been heavily investigated as catalysts over the last fifteen years due to their high surface area-to-volume ratio and unique size-dependent properties.[125–128] Relative to their larger nanoparticle counterparts, gold nanoclusters are of particular interest as their discrete atomic formulas and precise structures can allow for the determination of structure-activity relationships. Gold clusters have been reported to catalyze a large variety of reactions, including—but not limited to—oxidations,[83,129–131] reductions,[132] couplings,[133–135] and hydrogenations.[25,136]

In these reactions, surface ligands on gold nanoclusters can serve a critical role in determining catalytic properties. Ligand bond strength can impact turnover rate as catalysis is believed to occur by the desorption of individual surface ligands to reveal active catalytic sites.[83–86] The steric nature of the remaining ligands along with ligand-ligand interactions and ligand-solvent interactions can further dictate how accessible these sites are.[78] Catalytic activity and selectivity of a cluster can also be substantially altered by the functional group used for ligation (e.g.-thiolate versus acetylide) and the type of ligand (e.g.-aliphatic versus aromatic).[59,137] Further, clusters can also be prepared as homogeneous or heterogeneous catalysts depending on whether hydrophobic or hydrophilic ligands are utilized.[138]

Gold nanoclusters are suggested to be stable and recyclable catalysts in thioether oxidation reactions.[139,140] The presence of a sulfur atom in both the reactant and product of this reaction might promote degradation of the cluster ligand layer, however. Thioether functionalities have been previously used to protect gold nanoparticle surfaces.[141–143] Gold has also been previously shown to cleave carbon-sulfur bonds in thioethers, and thioether oxidation can lead to a large variety of sulfur-containing degradation products.[144,145] Further, Wu showed an increase in conversion of propargylic alcohols to enones by gold clusters when dimethyl sulfoxide was used as a solvent.[146] While the authors suggest that solvent molecules stabilize the overall nanocluster, it is possible that discrete interactions lead to the observed increase in catalytic activity.

Herein, we investigate potential interactivity between gold nanoclusters and the reactants and products of thioether oxidation reactions. Interestingly, we observe two net reactions that amount to ligand exchange on $Au_{25}(PET)_{18}$. One process we observe is

thiolate-for-thiolate exchange, where the incoming ligand is derived from the thioether solvent or an intermediate in the oxidation reaction. We also report sulfoxide-for-thiolate exchange, which constitutes the first experimental evidence to suggest a sulfoxide ligand on a gold nanocluster. These results overall demonstrate that the surface of a gold nanocluster can evolve over the course of this reaction and suggest that sulfoxide solvents might serve a direct role in other catalytic reactions. The cleavage of a carbon-sulfur bond to form a thiolate also has implications for the biofunctionalization of gold nanoclusters and nanoparticles.

4.3 Results

We began our investigation by stirring $Au_{25}(PET)_{18}$ in dimethyl sulfide (DMS). Full synthetic and analytical details for this process can be found in appendix C. Interestingly, mass spectrometry results obtained after stirring for one minute reveal the formation of a new product (figure 4.1). The mass difference between this peak and the starting material closely corresponds to the mass difference between a phenylethanethiolate (PET) ligand and methylthiolate (90.73 observed versus 90.13 calculated). When stirred for longer periods of time, we observe an increased number of products with a Gaussian-like distribution, where each peak differs by approximately the same mass difference (i.e.- approximately 90 m/z). The presence of a Gaussian-like distribution of products that evolves with time is characteristic of ligand exchange reactions where only part of the ligand layer is replaced.[13,27,76] These findings suggest a similar process occurs in the present work. Such a result would necessitate carbon-sulfur bond cleavage, of which gold has been reported to perform.[144,147,148]

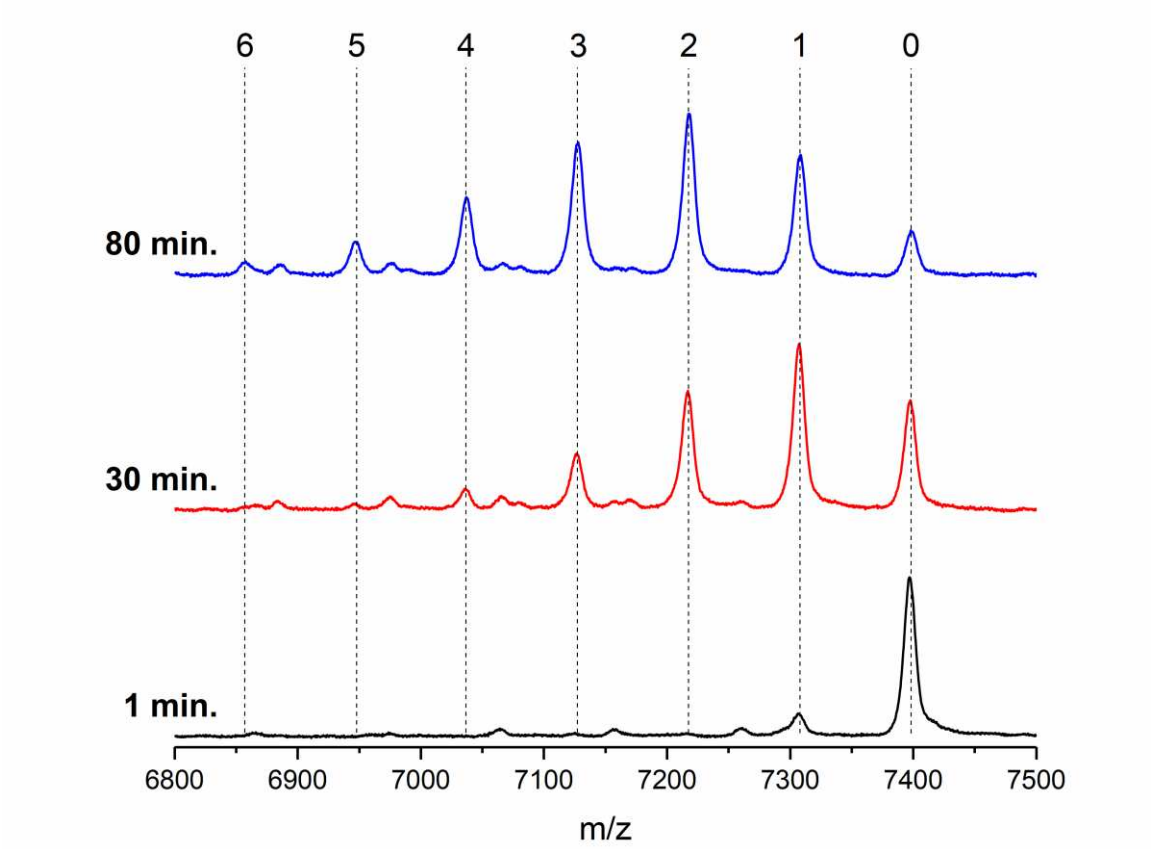


Figure 4.1. Evolution of the positive MALDI-MS for $Au_{25}(PET)_{18-x}(SMe)_x$ over time when stirred in DMS, where x is the number of exchanged ligands.

To test if the observed products are formed by thiolate exchange *via* carbon-sulfur bond cleavage, we performed a similar reaction using di-*tert*-butyl sulfide (figure 4.2). After stirring for one minute, we observe the formation of an additional product. The difference between this peak and the parent compound closely mirrors the mass difference between a PET ligand and *tert*-butyl thiolate (48.86 observed versus 48.05 calculated). We note that unlike in the case of dimethyl sulfide, we do not observe an increase in the distribution of products over time in the current example. However, the initial peak intensity of this new product does increase over time, suggesting a much slower reaction relative to when dimethyl sulfide is used.

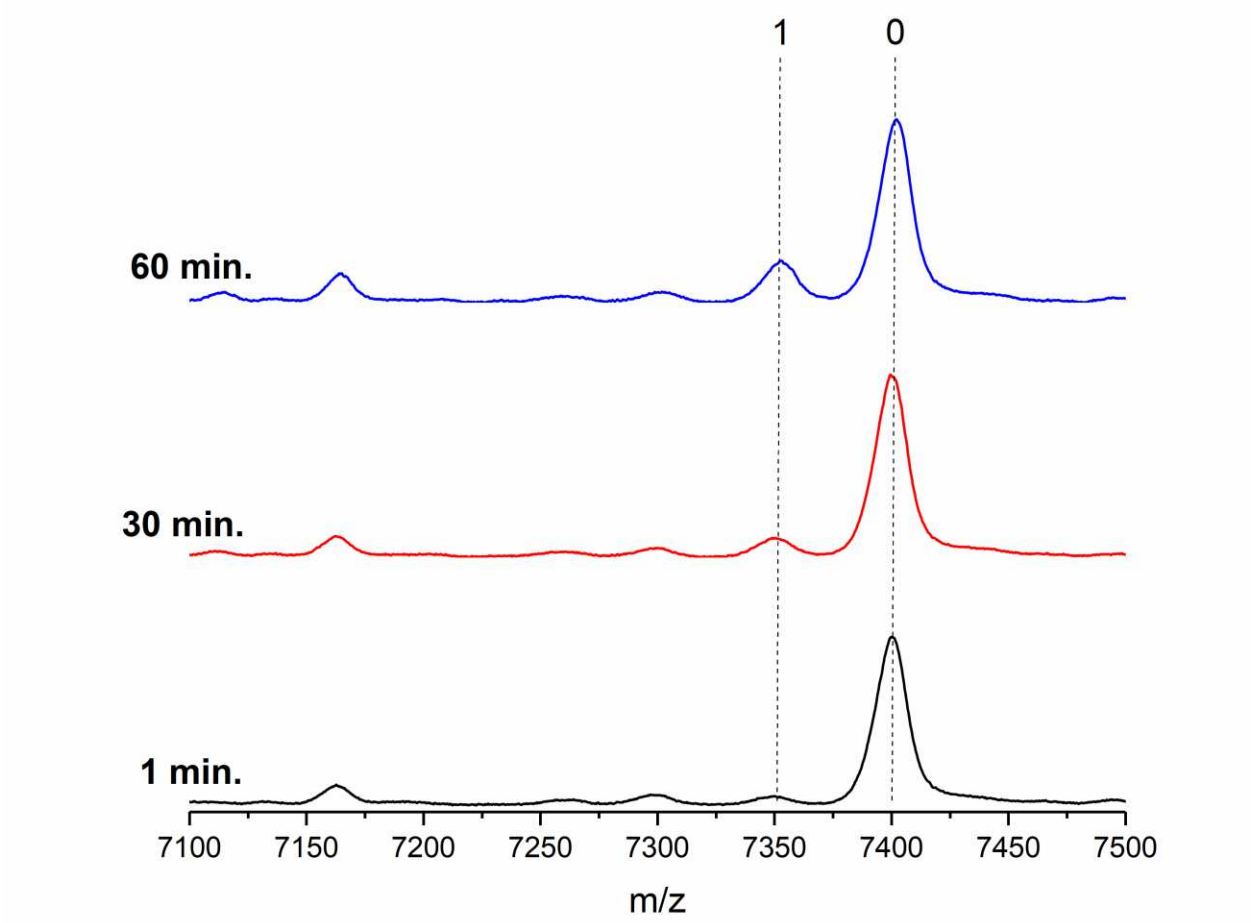


Figure 4.2. Evolution of the positive MALDI-MS spectrum of $Au_{25}(PET)_{18-x}(S\mathit{t}Bu)_x$ over time when stirred in di-*tert*-butyl sulfide, where *x* is the number of exchanged ligands. Other peaks in the spectrum result from fragmentation of the indicated products.

We also performed the reaction with diphenyl sulfide to further verify the identities of exchange species (figure C.2). After 16 hours, we observe a large number of peaks corresponding to phenylthiolate exchange with PET (29.52 observed average mass difference versus 28.06 calculated). While there is a larger discrepancy between the observed and calculated mass differences in this casse, this discrepancy might be caused by the unaccounted loss of a hydrogen atom. As such, it is possible that exchange occurs with the proposed ligand. It also possible, however, that aromatic rings might exchange directly onto the gold surface. Gold surfaces have been previously functionalized with

aromatic rings through a direct gold-carbon bond.[149–152] The mass difference between a PET ligand and a deprotonated benzene ring is similar to the mass difference for exchange of two *tert*-butyl thiolates with two phenylthiolate ligands (60.12 versus 59.04, respectively). Due to the small variation between these two mass differences, the two potential exchange products cannot be readily distinguished from one another. As such, it possible that the products observed are a result of exchange with aryl groups or a mixture of both exchange processes.

In exchange processes involving free thiol ligands, the hydrogen atom on the incoming ligand is believed to be transferred to the outgoing ligand while both species are coordinated to the cluster surface.[26] We hypothesized a similar pathway might occur in the present study where a thioether side chain is transferred to the outgoing ligand. To probe for this, we implemented tetrahydrothiophene (THT) as the thioether. A side chain transfer would trap the outgoing PET ligand by combining it with THT into a single molecule and products with increased mass would be observed. We do not observe any peaks in the mass spectrum corresponding to this potential product, however, even after allowing the reaction to proceed for upwards of 16 hours (figure 4.3).

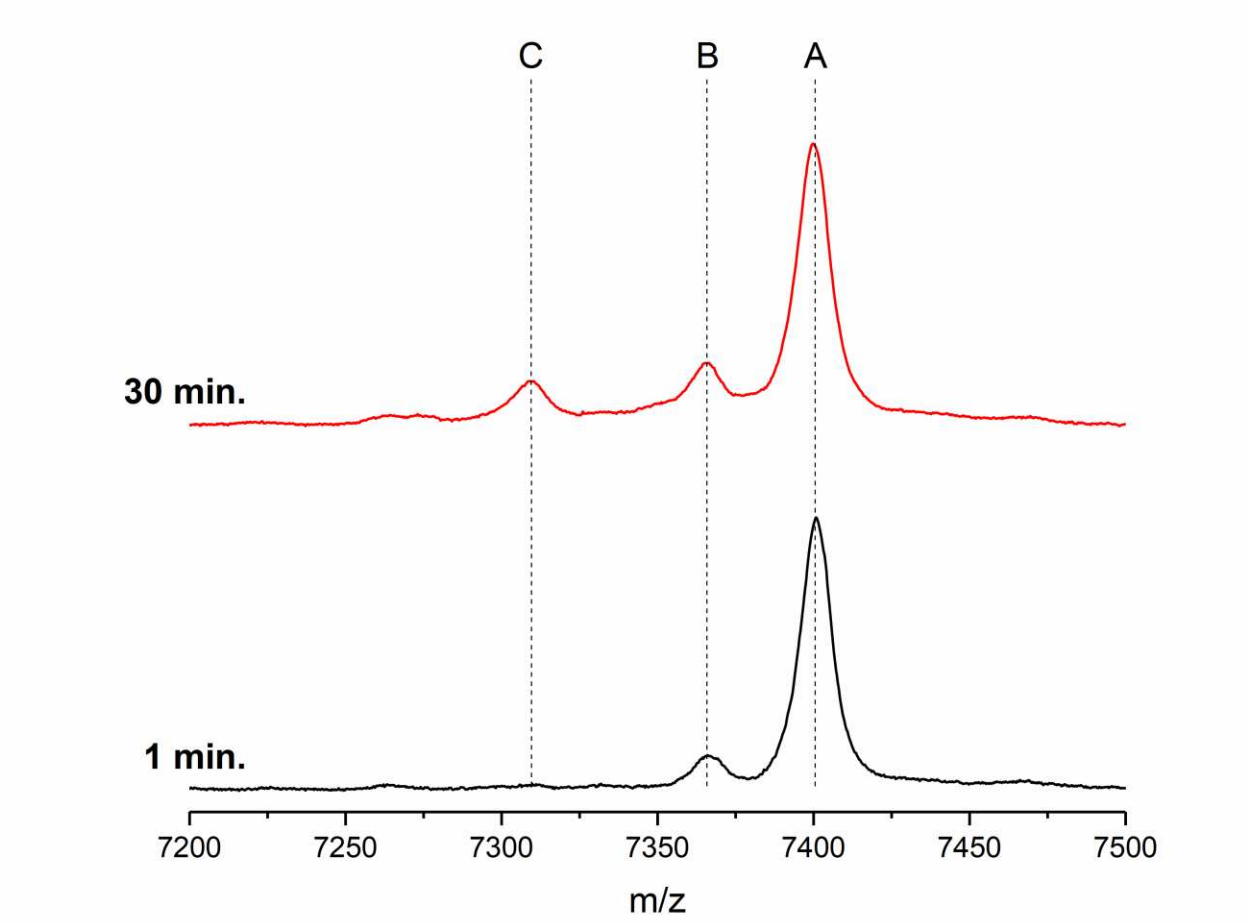


Figure 4.3. Evolution of the positive MALDI-MS spectrum of $Au_{25}(PET)_{18}$ over time when stirred in THT. A) $Au_{25}(PET)_{18}$ B) $Au_{25}(PET)_{17}(THT\ 1\text{-}oxide)_1$ C) $Au_{25}(PET)_{17}(SMe)_1$

Interestingly, we observe the formation of a different peak that is approximately 34 m/z lower than the starting cluster after 1 minute. This mass difference corresponds to exchange of PET for an oxidized form of THT. Oxidation can potentially occur at three different positions on THT: the sulfur atom, the α carbon, and the β carbon. As of this writing, there are no reports on the oxidation of THT to produce an alcohol group at either the α or β position. Therefore, the most likely candidate for exchange is THT 1-oxide (34.47 observed mass difference versus 34.06 calculated). Furthermore, we observe the appearance of a second distinct peak after the reaction proceeds for 30 minutes. The mass difference between this peak and others in the spectrum is inconsistent with that

observed for the previously mentioned sulfoxide-for-thiolate exchange, suggesting the concurrence of a second type of exchange. To our surprise, this second peak exhibits a mass difference relative to the $Au_{25}(PET)_{18}$ peak that is nearly identical to the mass difference observed when dimethyl sulfide is used (90.78 observed in THT and 90.73 observed in dimethyl sulfide). Single electron oxidation of THT produces several degradation products that are closely related to thioformaldehyde, which can be considered a precursor to methylthiolate.[145] Therefore, we propose the observed exchange product is the result of methylthiolate exchange with PET (90.78 observed mass difference versus 90.13 calculated).

4.4 Discussion

In the current work, we observe the formation of products resulting from ligand exchange on $Au_{25}(PET)_{18}$. When linear thioethers are employed, products that amount to thiolate-for-thiolate exchange are formed. In these reactions, the incoming thiolate appears to be derived from the thioether by cleavage of one of the carbon-sulfur bonds. Barrabés has previously suggested gold clusters might be capable of breaking and forming carbon-sulfur bonds as cyclohexanethiol was observed as a byproduct in an oxidation reaction of cyclehexane catalyzed by a gold cluster.[147] Gold surfaces have also been used to catalyze the transformation of dimethyl sulfide into ethylene gas, further demonstrating the ability of gold to cleave carbon-sulfur bonds.[144]

While the mechanism of this exchange remains unknown, the present results provide some insight. It has been proposed that gold converts dimethyl sulfide into ethylene by initial homolysis of a carbon-sulfur bond to form a methylthiol radical and a methyl radical.[148] A similar mechanistic pathway might be at work here as *tert*-butyl radicals are

relatively stable intermediates and phenyl radicals have been used to functionalize gold surfaces. Consequently, increasing the stability of any resulting radical intermediates might accelerate the rate of exchange. To this end, we note that dimethyl sulfide generates a higher degree of exchange than *tert*-butyl sulfide despite methyl radicals being less stable than *tert*-butyl radicals. Differences in steric factors might alter the kinetics of adsorption and other related steps and account for the observed results, however. Another hypothetical pathway involves the transfer of a thioether side chain to the outgoing ligand. This does not appear to be likely, though, as an appropriate product was not observed when a cyclic thioether (i.e.-THT) was used. It has been proposed that oxidation of dimethyl sulfide leads to the formation of methanethiol in certain bacteria species.[153] Since gold nanoclusters have been shown to oxidize thioethers to sulfoxides, initial oxidation of the the sulfur atom might lead to the observed exchange products. Further experiments are needed to investigate this, however.

When gold clusters are placed in THT, we observe the formation of a product that corresponds to exchange with THT 1-oxide. Previous works suggest that gold clusters selectively oxidize thioethers to sulfoxides as a result of weak interactions between sulfoxides and nanoclusters.[139,140,154,155] The ability to detect sulfoxide-for-thiolate exchange in these reactions indicates the sulfoxide-cluster interaction might be significantly stronger than what is currently suggested, however. To the best of our knowledge, this is also the first evidence that suggests sulfoxides might function as ligands on gold clusters.

In addition to sulfoxide exchange, we also observe methylthiolate exchange when using THT. Oxidized THT and thioformaldehyde derivatives can be detected

simultaneously after initial oxidation of THT, indicating the possibility for several reaction pathways to occur after initial oxidation.[156] The observation of two concurrent exchange processes in our work supports this idea and demonstrates the potential for gold clusters to undergo varying exchange pathways within a single reaction. While we demonstrate two possible exchange processes here, these results might not represent all possible exchanges.

Previous thioether oxidation reports have stated that gold clusters are stable under the reaction conditions and are highly recyclable.[139,140] Here, we observe multiple different ligand exchange processes involving species present in such reactions. It is especially worth noting that some of these exchanges are observed within a minute of combining the thioether and nanocluster. Therefore, we propose that thiolate-protected gold clusters are not fully stable in the presence of exogenous thioether functionalities. Bare gold nanoclusters (i.e.-nanoclusters which have had their ligands removed) might also unstable as the transformation of thioethers into thiolates could lead the formation of a ligand layer on the surface. Furthermore, this behavior might also lead to exchange with methionine residues in proteins and have implications for biofunctionalization of gold clusters and nanoparticles.

In one report of a nanocluster-catalyzed reaction, the use of dimethyl sulfoxide as a solvent led to higher conversion rates.[146] The authors attributed the increase in catalytic conversion to overall stabilization of the cluster by dimethyl sulfoxide, but did not implicate any specific process or interactions as the cause for the increased stabilization. The observation of sulfoxide ligand exchange in the current work might provide deeper insight

into the previously reported catalytic improvement. Additionally, this observation might inform the use of sulfoxide-containing solvents in future reactions.

Previous work of ours showed that oxidation reactions are likely catalyzed by cluster degradation products rather than intact clusters.[113] We did not investigate the presence of degradation products in the present work and only propose that the cluster ligand layer is subject to change over the course of a thioether oxidation reaction. As such, it is possible that cluster degradation products are actively involved in the conversion of thioethers into thiolate species. Regardless of whether the intact cluster is the active catalyst or a pre-catalyst though, ligand layer alterations might lead to changes in observed catalytic behavior in the long term.

In conclusion, we report multiple different ligand exchange reactions between gold nanoclusters and compounds present in thioether oxidation conditions. We also observe the first result that suggests the presence of sulfoxide ligands on a gold nanocluster which would indicate the selectivity in thioether oxidation reactions is a result of other factors. These exchanges indicate that gold clusters are not fully stable in the presence of thioether-containing compounds and that catalytic behavior might vary over the course of a reaction.

CHAPTER 5: CONFORMATIONAL POLYMORPHISM IN $Au_{25}(PET)_{18}^0$

5.1 Synopsis

The impact of surface ligand dynamics on gold nanocluster reactivity and properties is a new area of interest. While initial reports suggest that “rigidification” of the ligand layer can lead to increases in emission intensity, little is known about the impact that changes to ligand orientation might have on nanocluster behavior. In this chapter, we report multiple crystallographically-determined conformational polymorphs of $Au_{25}(PET)_{18}^0$. These structures vary from one another by changes in the anti/gauche conformations of individual ligands but not in the observe inter-ligand stereochemical relationships. Because of these differences in ligand conformation, variance in solvent accessibility of surface gold atoms is observed between structures. Interestingly, we observe a chiral ligand layer conformation in one structure, suggesting the potential for using crystal engineering to induce non-linear optical responses. These findings help inform understanding of site-selective ligand exchange reactions, catalytic activity, and optical responses of gold nanoclusters.

5.2 Introduction

The ability to generate crystals of gold nanoclusters over the last fifteen years has been integral to developing a deeper understanding on how nanoclusters function. Early crystal structures fundamentally changed the understanding of nanocluster structures.[39,104] To date, the production of crystal structures continues to verify formula assignment and inform about structural details in newly synthesized nanoclusters.[52] Later works utilized x-ray crystallography to investigate cluster processes such as site-selective

ligand exchange.[26,28] Furthermore, crystal structures are commonly utilized to produce models in computational efforts.[157,158]

Reports have a shown that properties of gold nanoclusters can be altered upon crystallization. Zhu et al. demonstrated crystallization-induced enhancement of emission intensity while Tang and co-workers observed a shift in the UV-Vis absorption and circular dichroism spectra for a Au_3 cluster after it was crystallized.[80,81] More interestingly, Maran reported differences in the magnetic response of individual $Au_{25}(PET)_{18}^0$ crystals.[159] When multiple crystals were analyzed simultaneously, the magnetic response varied even more, suggesting differences between the individual crystals present.

Crystallographic conformational polymorphism—the ability for a compound to exist in more than one isolable conformation in the crystalline state—is well-known to produce property differences between crystals of a compound. This phenomenon has been shown to influence bioavailability and stability in pharmaceutical drugs,[160,161] alter the physical size and shape of inorganic complex crystals,[162] induce conductivity in compounds containing extended π systems,[163] and alter the color and optical properties of organic molecules.[164,165] Furthermore, conformational polymorphism is predicted to alter dipole moments in a substantial number of cases.[166]

In a recent report, we crystallographically determined the first two examples of chiral ligand conformations on $Au_{25}L_{18}$, where L consists of achiral chalcogenate ligands.[29] The use of chiral ligands on gold nanoclusters is known to produce a second-order nonlinear response.[167] While $Au_{25}L_{18}$ does not exhibit similar behavior in solution due to the presence of centrosymmetry, the absence of an inversion center within the cluster in these structures suggests the potential for nonlinear optical responses once crystallized.

Experimental investigation into the effect of a chiral ligand layer conformation on nonlinear optical behavior in those samples was precluded by the additional presence of asymmetric ligand exchange, however. To this end, computational work has suggested a stable chiral ligand layer conformation for a thiolate protected Au_{25} cluster. Experimental reports for such a cluster has yet to be reported, however.

Herein, we report the solutions for two new $Au_{25}(PET)_{18}^{0}$ crystal structures along with higher quality versions of two previously published structures.[109,110] To our satisfaction, one new structure lacks centrosymmetry within the cluster due to the presence of a chiral ligand layer conformation. This structure represents the first example of a homoleptic Au_{25} cluster protected by achiral chalcogenate ligands where chirality is a result of crystallization. Symmetry is broken in this structure by a different stereochemical method than what is observed in our previous work. Solvent exposure calculations also show differences between structures, providing further insight into understanding ligand exchange and catalysis reactions on gold nanoclusters.

5.3 Results

$Au_{25}(PET)_{18}^{0}$ was obtained by oxidizing $Au_{25}(PET)_{18}^{-1}$ during the crystallization process. Four different habits of Au_{25} crystals were obtained by using differing crystallization methods. Full information about these methods can be found in appendix D. Single crystal x-ray diffraction data was collected by Dr. Pierre Le Magueres at Rigaku Americas Corporation using a XtaLAB Syngergy Custom FR-X MM007HF diffractometer. Full details about data collection can be found in appendix D. Structures were resolved in Olex2 using SHELXL for refinements.[168]

To quantitatively demonstrate conformational differences between crystal structures, we consider two types of ligand stereochemistry that have been previously described (figure 5.1).[107] First, we consider the stereochemistry of individual ligands. Each ligand adopts either a gauche conformation where the carbon-phenyl bond and the carbon-sulfur bond are at a 60^0 angle or an anti conformation where the angle is 180^0. For the purposes of discussion, small variations from these idealized geometries are ignored. Second, we consider the stereochemical relationships between ligands. $Au_{25}(PET)_{18}^0$ contains six ligand-gold-ligand-gold-ligand chains ("staples") on the outside of the icosahedral core, with each staple lying in one of the three coordinate planes (xy, xz, or yz). Each ligand rests on one side of the plane, and its relationship to adjacent ligands can be described as either cis (resting on the same side) or trans (resting on opposite sides).

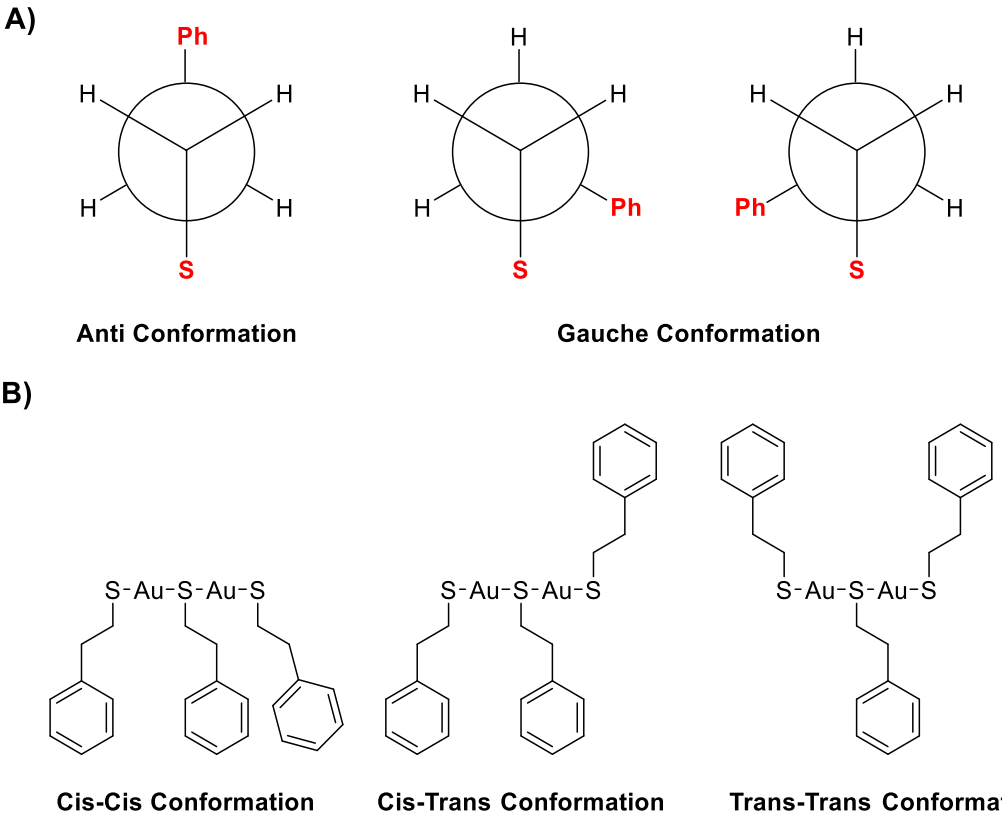
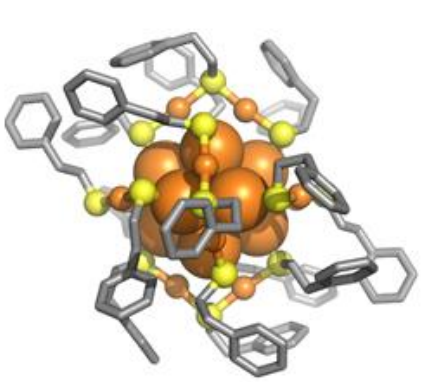
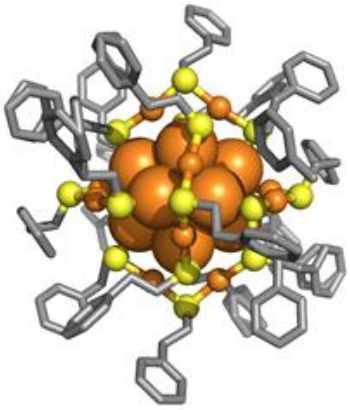


Figure 5.1. Possible conformational differences A) within a ligand and B) between ligands.

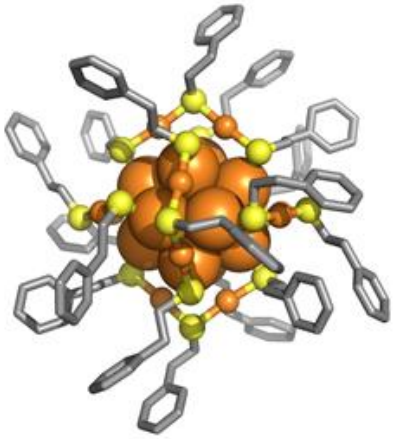
Each crystal habit produced a unique structure (figure 5.2). The cuboid and quadrilateral prism samples produced crystal structures which have been previously published, while the needle and thin platelet samples produced two novel structures.[109,110] Three different combinations of anti and gauche ligand conformations were observed within these structures. While two structures contain identical numbers of ligands in anti and gauche conformations, the two clusters differ in the spatial distribution of these ligand conformations. Interestingly, we only observe trans-trans relationships between ligands in each staple unit. This differs from previous computational predictions where three of the four lowest energy structures contain multiple staple units with cis-trans stereochemical relationships.[107]



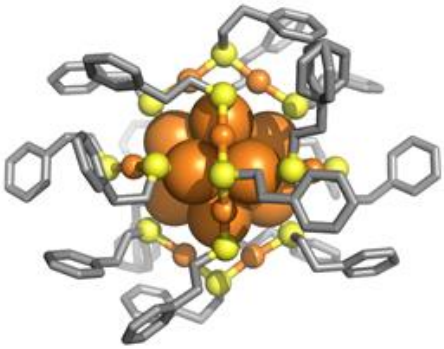
Thin Platelet



Quadrilateral Prism



Needle



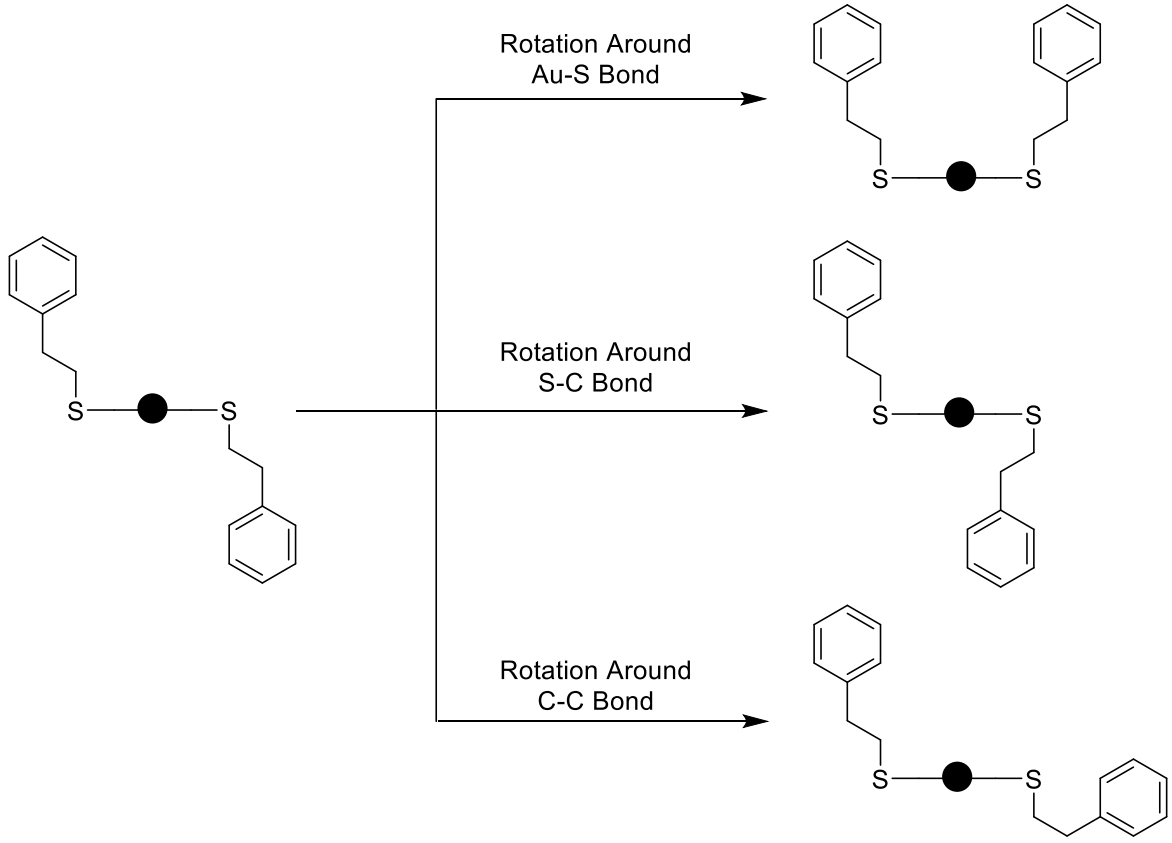
Cuboid

	Thin Platelet	Quadrilateral Prism	Needle	Cuboid
Anti	8	14	14	10
Gauche	10	4	4	8
Cis-Cis	0	0	0	0
Cis-Trans	0	0	0	0
Trans-Trans	6	6	6	6
Symmetric	Yes	Yes	No	Yes

Figure 5.2 Number of observed stereochemical relationships and symmetry elements in $Au_{25}(PET)_{18}^{0}$ crystal structures obtained from different crystal habits. Gold atoms are represented by orange spheres, sulfur atoms are represented by yellow spheres, and carbon bonds are represented by gray sticks. Hydrogen atoms have been removed for the purposes of clarity.

We have previously observed the absence of an inversion center in $Au_{25}(SeR)_{18-x}(SR)_x$ clusters due to a chiral conformation of the composite ligand layer. We observe a similar result in the present work as the needle-derived structure lacks centrosymmetry

within the cluster. In order to compare the current work with our previous results, we consider different stereochemical means of breaking ligand layer symmetry (scheme 5.1). The current structure lacks symmetry due to the rotation of ligands around the sulfur-carbon bonds relative to the ligands which would hypothetically be related by inversion symmetry. This differs from our previous results where symmetry was lost due to the rotation of ligands around the staple unit plane (i.e.-gold-sulfur bond rotation) relative to their hypothetical inversion-related ligand partners.



Scheme 5.1 Different stereochemical means of breaking inversion symmetry between ligand pairs. The centroid position is represented by a black dot.

Solvent accessibility of the cluster surface is generally considered to play an important role in ligand exchange and catalytic reactions.[26,27,83–86] To see if conformational polymorphism might have an impact on these types of reactions, we investigated each

crystal structure for solvent accessible gold atoms (table 5.1). Full details about these calculations can be found in appendix D. To help discuss these results, we employ the same nomenclature system that is used chapter 2 (figure 2.1).

Table 5.1. Calculated solvent accessibility values of surface gold atoms in each $Au_{25}(PET)_{18}^{0}$ structure. Gold atoms which are solvent accessible are highlighted in green. All values are in terms of $Å^2$.

	Thin Platelet	Quadrilateral Prism	Needle	Cuboid
D1-2	0.727	0.402	1.545	0
D1-4	0	0	0	0
D2-2	0.727	0.402	1.126	0
D2-4	0	0	0	0
D3-2	1.043	1.741	0.28	0
D3-4	0	0	0	0.902
D4-2	1.043	1.741	0.531	0
D4-4	0	0	0	0.902
D5-2	0.055	0.835	0.345	1.433
D5-4	0	0	0.771	0.061
D6-2	0.055	0.835	0.845	1.433
D6-4	0	0	0.733	0.061
TOTAL	3.650	5.960	6.180	4.790

In the thin platelet and quadrilateral prism structures, we observe no difference in which gold atoms are solvent accessible. However, we do observe differences in the degree of solvent accessibility at these different sites. Additionally, the quadrilateral prism structure contains more solvent exposed area relative to the thin platelet structure (5.960 $Å^2$ versus 3.650 $Å^2$). The needle structure exhibits solvent accessibility at the same positions as the thin platelet and quadrilateral prism structures, but also shows solvent exposure at two new additional positions (D5-4 and D6-4). Due to the chiral nature of the composite ligand layer conformation on this structure, gold atoms which are typically considered related by symmetry (e.g.-D1-2 and D2-2) contain different solvent accessibility values. Out of all the structures, the needle crystal structure surface is the most solvent exposed overall. The cuboid structure differs substantially from the other

structures as it contains the fewest number of solvent accessible gold atoms (i.e.-6 solvent exposed gold atoms). Three exposed atoms lie in close proximity to each other, while the other three similarly lie in close proximity on the opposite face of the nanocluster. This concentration of solvent accessibility to two general ends of the nanocluster is reminiscent of the hairy ball thereom that has been proposed for gold nanoparticles.[169] Overall, we observe a significant degree of variance in the locations and amount of solvent accessibility between these structures.

5.4 Discussion

We demonstrate multiple crystallographic ligand layer conformations on the well-studied $Au_{25}(PET)_{18}^0$ nanocluster system that exhibit differences in the number of crystal contact points. Recent studies indicate that crystal contact points serve a pivotal role in crystallization-induced property changes of metal nanoclusters.[80,81,170] As such, the present work suggests the possibility of using crystal engineering to optimize material properties of gold clusters for directed applications. Which properties might be affected by polymorphic behavior remains unknown, however. DFT calculations of $Au_{25}(PET)_{18}^0$ show the UV-Vis spectrum is not expected to be significantly impacted by changes to ligand layer geometry.[82] Conversely, these changes are expected to create a net dipole moment within the cluster. While Maran has proposed that variations between $Au_{25}(PET)_{18}^0$ crystals in magnetic response is a result of disordered microenvironments, it is possible these differences arise from polymorphic behavior.[159] Other material properties such as melting point, electrical conductivity, and thermal conductivity have yet to be investigated in any form.

Second-order nonlinear optical properties can be created in compounds lacking inversion symmetry. This behavior has often been produced in gold clusters with instrically chiral metal cores or those protected by chiral ligands.[22,158,171] While previous crystal structures and experimental results have shown $Au_{25}(PET)_{18}$ to be centrosymmetric and have no significant second-order nonlinear response, the presence of a chiral ligand conformation once crystallized might produce nonlinear optical properties.[104,109,110,167] While we previously showed a chiral ligand conformation on a related nanocluster, the work was limited as any resulting nonlinear optical would likely be due in part to chirality generated by asymmetric exchange of ligands on the surface.[29] Furthermore, it was uncertain if the chiral ligand conformation arose due to crystal packing effects or ligand exchange and isomerization processes. These concerns are eliminated in the current structure as all ligands are chemically identical and no exchange processes occur. Consequently, this structure allows for future investigations to determine the role of ligand conformation on nonlinear optical behavior.

An understanding of solvent accessibility has informed about site-selective ligand exchange to date.[26–29] Conformational variability has been experimentally observed by NMR and has been predicted computationally,[77] and our most recent report on site-selective exchange observed multiple polymorphs that differed in ligand conformation.[29] While we attempted to minimize the possibility of selective crystallization processes in that work, ligand exchange processes might have biased which results we obtained. The present structures are free of these concerns and clearly demonstrate the transient nature of solvent accessibility on gold nanocluster surfaces. However, additional work is required

to determine which conformations might be present in solution and if these conformations exist in an equal distribution.

Catalysis reactions involving gold nanoclusters are similarly dependent on cluster surface exposure for adsorbing reactants.[83–86] In this work, we observe differences between structures in regards to the number of solvent accessible gold atoms and in the total amount of surface exposure. Changes to either of these factors can potentially impact the kinetics of a catalytic reaction and therefore increase or decrease the observed turnover rate. While the identity of the active catalyst species in these reactions remains a mystery, the present results suggest the potential to tune heterogeneous catalytic reactions involving gold nanoclusters by crystal engineering methods.[113]

Currently, it is not clear what factors promote conformational polymorphism in gold nanoclusters and how these parameters might be manipulated to engineer cluster material properties. Calculations suggest a low energetic barrier to conformational changes of ligands on gold nanoclusters.[108] Consequently, methods for generating specific crystal habits might be highly sensitive and difficult to reproduce. Though we report the crystallization conditions used to obtain the habits observed in this work, we note that these conditions do not always produce the same habits. Furthermore, it is possible that the structures reported here are a subset of all possible isolable $Au_{25}(PET)_{18}^{0}$ structures. In particular, DFT calculations suggest eight unique ligand layer conformation possibilities that are similar in energy.[107]

In conclusion, we observe two previously reported and two novel conformational polymorphs of $Au_{25}(PET)_{18}^{0}$. These polymorphs exhibit differences in crystal contact points and solvent accessibility values. One structure is chiral which suggests potential

nonlinear optical behavior. These results indicate the possibility of crystal engineering to induce and alter material properties of gold nanocluster for directed applications in the future.

BIBLIOGRAPHY

(1) Faraday, M. X. The Bakerian Lecture. —Experimental Relations of Gold (and Other Metals) to Light. *Trans R Soc Lond 147*, 145–181.

(2) Ghosh, P.; Han, G.; De, M.; Kim, C. K.; Rotello, V. M. Gold Nanoparticles in Delivery Applications. *Adv. Drug Deliv. Rev.* **2008**, *60* (11), 1307–1315. https://doi.org/10.1016/j.addr.2008.03.016.

(3) Kennedy, L. C.; Bickford, L. R.; Lewinski, N. A.; Coughlin, A. J.; Hu, Y.; Day, E. S.; West, J. L.; Drezek, R. A. A New Era for Cancer Treatment: Gold-Nanoparticle-Mediated Thermal Therapies. *Small* **2011**, *7* (2), 169–183. https://doi.org/10.1002/smll.201000134.

(4) Calixto, G. M. F.; Bernegossi, J.; De Freitas, L. M.; Fontana, C. R.; Chorilli, M. Nanotechnology-Based Drug Delivery Systems for Photodynamic Therapy of Cancer: A Review. *Molecules* **2016**, *21* (3), 342. https://doi.org/10.3390/molecules21030342.

(5) Saha, K.; Agasti, S. S.; Kim, C.; Li, X.; Rotello, V. M. Gold Nanoparticles in Chemical and Biological Sensing. *Chem. Rev.* **2012**, *112* (5), 2739–2779. https://doi.org/10.1021/cr2001178.

(6) Hutter, E.; Maysinger, D. Gold Nanoparticles and Quantum Dots for Bioimaging. *Microsc. Res. Tech.* **2011**, *74* (7), 592–604. https://doi.org/10.1002/jemt.20928.

(7) Catchpole, K. R.; Polman, A. Plasmonic Solar Cells. *Opt. Express* **2008**, *16* (26), 21793–21800. https://doi.org/10.1364/OE.16.021793.

(8) Notarianni, M.; Vernon, K.; Chou, A.; Aljada, M.; Liu, J.; Motta, N. Plasmonic Effect of Gold Nanoparticles in Organic Solar Cells. *Sol. Energy* **2014**, *106*, 23–37. https://doi.org/10.1016/j.solener.2013.09.026.

(9) Corma, A.; Garcia, H. Supported Gold Nanoparticles as Catalysts for Organic Reactions. *Chem. Soc. Rev.* **2008**, *37* (9), 2096–2126. https://doi.org/10.1039/B707314N.

(10) Wang, S.; Meng, X.; Das, A.; Li, T.; Song, Y.; Cao, T.; Zhu, X.; Zhu, M.; Jin, R. A 200-Fold Quantum Yield Boost in the Photoluminescence of Silver-Doped AgxAu25−x Nanoclusters: The 13 Th Silver Atom Matters. *Angew. Chem. Int. Ed.* **2014**, *53* (9), 2376–2380. https://doi.org/10.1002/anie.201307480.

(11) Bhat, S.; Baksi, A.; Mudedla, S. K.; Natarajan, G.; Subramanian, V.; Pradeep, T. Au22Ir3(PET)18: An Unusual Alloy Cluster through Intercluster Reaction. *J. Phys. Chem. Lett.* **2017**, *8* (13), 2787–2793. https://doi.org/10.1021/acs.jpclett.7b01052.

(12) Guo, R.; Song, Y.; Wang, G.; Murray, R. W. Does Core Size Matter in the Kinetics of Ligand Exchanges of Monolayer-Protected Au Clusters? *J. Am. Chem. Soc.* **2005**, *127* (8), 2752–2757. https://doi.org/10.1021/ja044638c.

(13) Krishnadas, K. R.; Baksi, A.; Ghosh, A.; Natarajan, G.; Som, A.; Pradeep, T. Interparticle Reactions: An Emerging Direction in Nanomaterials Chemistry. *Acc. Chem. Res.* **2017**, *50* (8), 1988–1996. https://doi.org/10.1021/acs.accounts.7b00224.

(14) Tracy, J. B.; Crowe, M. C.; Parker, J. F.; Hampe, O.; Fields-Zinna, C. A.; Dass, A.; Murray, R. W. Electrospray Ionization Mass Spectrometry of Uniform and Mixed

Monolayer Nanoparticles: Au25[S(CH2)2Ph]18 and Au25[S(CH2)2Ph]18-x(SR)x. *J. Am. Chem. Soc.* **2007**, *129* (51), 16209–16215. https://doi.org/10.1021/ja076621a.

(15) Negishi, Y.; Chaki, N. K.; Shichibu, Y.; Whetten, R. L.; Tsukuda, T. Origin of Magic Stability of Thiolated Gold Clusters: A Case Study on Au25(SC6H13)18. *J. Am. Chem. Soc.* **2007**, *129* (37), 11322–11323. https://doi.org/10.1021/ja073580+.

(16) Wu, Z.; Gayathri, C.; Gil, R. R.; Jin, R. Probing the Structure and Charge State of Glutathione-Capped Au25(SG)18 Clusters by NMR and Mass Spectrometry. *J. Am. Chem. Soc.* **2009**, *131* (18), 6535–6542. https://doi.org/10.1021/ja900386s.

(17) Dass, A.; Theivendran, S.; Nimmala, P. R.; Kumara, C.; Jupally, V. R.; Fortunelli, A.; Sementa, L.; Barcaro, G.; Zuo, X.; Noll, B. C. Au133(SPh-TBu)52 Nanomolecules: X-Ray Crystallography, Optical, Electrochemical, and Theoretical Analysis. *J. Am. Chem. Soc.* **2015**, *137* (14), 4610–4613. https://doi.org/10.1021/ja513152h.

(18) Waszkielewicz, M.; Olesiak-Banska, J.; Comby-Zerbino, C.; Bertorelle, F.; Dagany, X.; Bansal, A. K.; Sajjad, M. T.; Samuel, I. D. W.; Sanader, Z.; Rozycka, M.; et al. PH-Induced Transformation of Ligated Au25 to Brighter Au23 Nanoclusters. *Nanoscale* **2018**, *10* (24), 11335–11341. https://doi.org/10.1039/C8NR00660A.

(19) Song, Y.; Abroshan, H.; Chai, J.; Kang, X.; Kim, H. J.; Zhu, M.; Jin, R. Molecular-like Transformation from PhSe-Protected Au25 to Au23 Nanocluster and Its Application. *Chem. Mater.* **2017**, *29* (7), 3055–3061. https://doi.org/10.1021/acs.chemmater.7b00058.

(20) Nasaruddin, R. R.; Yao, Q.; Chen, T.; Hülsey, M. J.; Yan, N.; Xie, J. Hydride-Induced Ligand Dynamic and Structural Transformation of Gold Nanoclusters during a Catalytic Reaction. *Nanoscale* **2018**, *10* (48), 23113–23121. https://doi.org/10.1039/C8NR07197G.

(21) Dainese, T.; Antonello, S.; Bogialli, S.; Fei, W.; Venzo, A.; Maran, F. Gold Fusion: From Au25(SR)18 to Au38(SR)24, the Most Unexpected Transformation of a Very Stable Nanocluster. *ACS Nano* **2018**, *12* (7), 7057–7066. https://doi.org/10.1021/acsnano.8b02780.

(22) Steerteghem, N. V.; Cleuvenbergen, S. V.; Deckers, S.; Kumara, C.; Dass, A.; Häkkinen, H.; Clays, K.; Verbiest, T.; Knoppe, S. Symmetry Breaking in Ligand-Protected Gold Clusters Probed by Nonlinear Optics. *Nanoscale* **2016**, *8* (24), 12123–12127. https://doi.org/10.1039/C6NR02251K.

(23) Dainese, T.; Antonello, S.; Gascón, J. A.; Pan, F.; Perera, N. V.; Ruzzi, M.; Venzo, A.; Zoleo, A.; Rissanen, K.; Maran, F. Au25(SEt)18, a Nearly Naked Thiolate-Protected Au25 Cluster: Structural Analysis by Single Crystal X-Ray Crystallography and Electron Nuclear Double Resonance. *ACS Nano* **2014**, *8* (4), 3904–3912. https://doi.org/10.1021/nn500805n.

(24) De Nardi, M.; Antonello, S.; Jiang, D.; Pan, F.; Rissanen, K.; Ruzzi, M.; Venzo, A.; Zoleo, A.; Maran, F. Gold Nanowired: A Linear (Au25)n Polymer from Au25 Molecular Clusters. *ACS Nano* **2014**, *8* (8), 8505–8512. https://doi.org/10.1021/nn5031143.

(25) Li, G.; Jin, R. Gold Nanocluster-Catalyzed Semihydrogenation: A Unique Activation Pathway for Terminal Alkynes. *J. Am. Chem. Soc.* **2014**, *136* (32), 11347–11354. https://doi.org/10.1021/ja503724j.

(26) Heinecke, C. L.; Ni, T. W.; Malola, S.; Mäkinen, V.; Wong, O. A.; Häkkinen, H.; Ackerson, C. J. Structural and Theoretical Basis for Ligand Exchange on Thiolate Monolayer Protected Gold Nanoclusters. *J. Am. Chem. Soc.* **2012**, *134* (32), 13316–13322. https://doi.org/10.1021/ja3032339.
(27) Ni, T. W.; Tofanelli, M. A.; Phillips, B. D.; Ackerson, C. J. Structural Basis for Ligand Exchange on Au25(SR)18. *Inorg. Chem.* **2014**, *53* (13), 6500–6502. https://doi.org/10.1021/ic5010819.
(28) Hossain, S.; Kurashige, W.; Wakayama, S.; Kumar, B.; Nair, L. V.; Niihori, Y.; Negishi, Y. Ligand Exchange Reactions in Thiolate-Protected Au25 Nanoclusters with Selenolates or Tellurolates: Preferential Exchange Sites and Effects on Electronic Structure. *J. Phys. Chem. C* **2016**, *120* (45), 25861–25869. https://doi.org/10.1021/acs.jpcc.6b08636.
(29) Hosier, C. A.; Ackerson, C. J. Regiochemistry of Thiolate for Selenolate Ligand Exchange on Gold Clusters. *J. Am. Chem. Soc.* **2019**, *141* (1), 309–314. https://doi.org/10.1021/jacs.8b10013.
(30) Yao, C.; Lin, Y.; Yuan, J.; Liao, L.; Zhu, M.; Weng, L.; Yang, J.; Wu, Z. Mono-Cadmium vs Mono-Mercury Doping of Au25 Nanoclusters. *J. Am. Chem. Soc.* **2015**, *137* (49), 15350–15353. https://doi.org/10.1021/jacs.5b09627.
(31) Tofanelli, M. A.; Ni, T. W.; Phillips, B. D.; Ackerson, C. J. Crystal Structure of the PdAu24(SR)180 Superatom. *Inorg. Chem.* **2016**, *55* (3), 999–1001. https://doi.org/10.1021/acs.inorgchem.5b02106.
(32) Liao, L.; Zhou, S.; Dai, Y.; Liu, L.; Yao, C.; Fu, C.; Yang, J.; Wu, Z. Mono-Mercury Doping of Au25 and the HOMO/LUMO Energies Evaluation Employing Differential Pulse Voltammetry. *J. Am. Chem. Soc.* **2015**, *137* (30), 9511–9514. https://doi.org/10.1021/jacs.5b03483.
(33) Knoppe, S.; Häkkinen, H.; Verbiest, T.; Clays, K. Role of Donor and Acceptor Substituents on the Nonlinear Optical Properties of Gold Nanoclusters. *J. Phys. Chem. C* **2018**, *122* (7), 4019–4028. https://doi.org/10.1021/acs.jpcc.7b12356.
(34) Knoppe, S.; Malola, S.; Lehtovaara, L.; Bürgi, T.; Häkkinen, H. Electronic Structure and Optical Properties of the Thiolate-Protected Au28(SMe)20 Cluster. *J. Phys. Chem. A* **2013**, *117* (40), 10526–10533. https://doi.org/10.1021/jp407494v.
(35) Choi, W.; Hu, G.; Kwak, K.; Kim, M.; Jiang, D.; Choi, J.-P.; Lee, D. Effects of Metal-Doping on Hydrogen Evolution Reaction Catalyzed by MAu24 and M2Au36 Nanoclusters (M = Pt, Pd). *ACS Appl. Mater. Interfaces* **2018**, *10* (51), 44645–44653. https://doi.org/10.1021/acsami.8b16178.
(36) Ebina, M.; Iwasa, T.; Harabuchi, Y.; Taketsugu, T. Time-Dependent Density Functional Theory Study on Higher Low-Lying Excited States of Au25(SR)18–. *J. Phys. Chem. C* **2018**, *122* (7), 4097–4104. https://doi.org/10.1021/acs.jpcc.7b12723.
(37) Nair, L. V.; Hossain, S.; Takagi, S.; Imai, Y.; Hu, G.; Wakayama, S.; Kumar, B.; Kurashige, W.; Jiang, D.; Negishi, Y. Hetero-Biicosahedral [Au24Pd(PPh3)10(SC2H4Ph)5Cl2]+ Nanocluster: Selective Synthesis and Optical and Electrochemical Properties. *Nanoscale* **2018**, *10* (40), 18969–18979. https://doi.org/10.1039/C8NR04078H.

(38) McPartlin, M.; Mason, R.; Malatesta, L. Novel Cluster Complexes of Gold(0)–Gold(I). *J. Chem. Soc. Chem. Commun.* **1969**, *0* (7), 334–334. https://doi.org/10.1039/C29690000334.
(39) Jadzinsky, P. D.; Calero, G.; Ackerson, C. J.; Bushnell, D. A.; Kornberg, R. D. Structure of a Thiol Monolayer-Protected Gold Nanoparticle at 1.1 Å Resolution. *Science* **2007**, *318* (5849), 430–433. https://doi.org/10.1126/science.1148624.
(40) Heaven, M. W.; Dass, A.; White, P. S.; Holt, K. M.; Murray, R. W. Crystal Structure of the Gold Nanoparticle [N(C8H17)4][Au25(SCH2CH2Ph)18]. *J. Am. Chem. Soc.* **2008**, *130* (12), 3754–3755. https://doi.org/10.1021/ja800561b.
(41) Qian, H.; Eckenhoff, W. T.; Zhu, Y.; Pintauer, T.; Jin, R. Total Structure Determination of Thiolate-Protected Au38 Nanoparticles. *J. Am. Chem. Soc.* **2010**, *132* (24), 8280–8281. https://doi.org/10.1021/ja103592z.
(42) Rambukwella, M.; Chang, L.; Ravishanker, A.; Fortunelli, A.; Stener, M.; Dass, A. Au36(SePh)24 Nanomolecules: Synthesis, Optical Spectroscopy and Theoretical Analysis. *Phys. Chem. Chem. Phys.* **2018**, *20* (19), 13255–13262. https://doi.org/10.1039/C8CP01564C.
(43) Kurashige, W.; Yamaguchi, M.; Nobusada, K.; Negishi, Y. Ligand-Induced Stability of Gold Nanoclusters: Thiolate versus Selenolate. *J. Phys. Chem. Lett.* **2012**, *3* (18), 2649–2652. https://doi.org/10.1021/jz301191t.
(44) Kurashige, W.; Yamazoe, S.; Kanehira, K.; Tsukuda, T.; Negishi, Y. Selenolate-Protected Au38 Nanoclusters: Isolation and Structural Characterization. *J. Phys. Chem. Lett.* **2013**, *4* (18), 3181–3185. https://doi.org/10.1021/jz401770y.
(45) Kurashige, W.; Yamazoe, S.; Yamaguchi, M.; Nishido, K.; Nobusada, K.; Tsukuda, T.; Negishi, Y. Au25 Clusters Containing Unoxidized Tellurolates in the Ligand Shell. *J. Phys. Chem. Lett.* **2014**, *5* (12), 2072–2076. https://doi.org/10.1021/jz500901f.
(46) Shichibu, Y.; Konishi, K. HCl-Induced Nuclearity Convergence in Diphosphine-Protected Ultrasmall Gold Clusters: A Novel Synthetic Route to “Magic-Number” Au13 Clusters. *Small* **2010**, *6* (11), 1216–1220. https://doi.org/10.1002/smll.200902398.
(47) Yang, S.; Chai, J.; Song, Y.; Kang, X.; Sheng, H.; Chong, H.; Zhu, M. A New Crystal Structure of Au36 with a Au14 Kernel Cocapped by Thiolate and Chloride. *J. Am. Chem. Soc.* **2015**, *137* (32), 10033–10035. https://doi.org/10.1021/jacs.5b06235.
(48) Sugiuchi, M.; Shichibu, Y.; Konishi, K. An Inherently Chiral Au24 Framework with Double-Helical Hexagold Strands. *Angew. Chem.* **2018**, *130* (26), 7981–7985. https://doi.org/10.1002/ange.201804087.
(49) Kang, X.; Xiang, J.; Lv, Y.; Du, W.; Yu, H.; Wang, S.; Zhu, M. Synthesis and Structure of Self-Assembled Pd2Au23(PPh3)10Br7 Nanocluster: Exploiting Factors That Promote Assembly of Icosahedral Nano-Building-Blocks. *Chem. Mater.* **2017**, *29* (16), 6856–6862. https://doi.org/10.1021/acs.chemmater.7b02015.
(50) Li, J.-J.; Guan, Z.-J.; Lei, Z.; Hu, F.; Wang, Q.-M. Same Magic Number but Different Arrangement: Alkynyl-Protected Au25 with D3 Symmetry. *Angew. Chem. Int. Ed.* **2019**, *58* (4), 1083–1087. https://doi.org/10.1002/anie.201811859.
(51) Wan, X.-K.; Guan, Z.-J.; Wang, Q.-M. Homoleptic Alkynyl-Protected Gold Nanoclusters: Au44(PhC≡C)28 and Au36(PhC≡C)24. *Angew. Chem. Int. Ed.* **2017**, *56* (38), 11494–11497. https://doi.org/10.1002/anie.201706021.

(52) Lei, Z.; Li, J.-J.; Wan, X.-K.; Zhang, W.-H.; Wang, Q.-M. Isolation and Total Structure Determination of an All-Alkynyl-Protected Gold Nanocluster Au144. *Angew. Chem. Int. Ed.* **2018**, *57* (28), 8639–8643. https://doi.org/10.1002/anie.201804481.
(53) Narouz, M. R.; Osten, K. M.; Unsworth, P. J.; Man, R. W. Y.; Salorinne, K.; Takano, S.; Tomihara, R.; Kaappa, S.; Malola, S.; Dinh, C. T.; et al. N-Heterocyclic Carbene-Functionalized Magic Number Gold Nanoclusters. **2018**. https://doi.org/10.26434/chemrxiv.7323989.v1.
(54) Narouz, M. R.; Takano, S.; Lummis, P. A.; Levchenko, T. I.; Nazemi, A.; Kaappa, S.; Malola, S.; Yousefalizadeh, S.; Stamplecoskie, K. G.; Häkkinen, H.; et al. N-Heterocyclic Carbene-Stabilized Au13 Superatom Clusters. **2018**. https://doi.org/10.26434/chemrxiv.7498748.v1.
(55) Nigra, M. M.; Yeh, A. J.; Okrut, A.; DiPasquale, A. G.; Yeh, S. W.; Solovyov, A.; Katz, A. Accessible Gold Clusters Using Calix[4]Arene N-Heterocyclic Carbene and Phosphine Ligands. *Dalton Trans.* **2013**, *42* (35), 12762–12771. https://doi.org/10.1039/C3DT50804H.
(56) Kang, X.; Zhu, M. Tailoring the Photoluminescence of Atomically Precise Nanoclusters. *Chem. Soc. Rev.* **2019**. https://doi.org/10.1039/C8CS00800K.
(57) Kwak, K.; Lee, D. Electrochemical Characterization of Water-Soluble Au25 Nanoclusters Enabled by Phase-Transfer Reaction. *J. Phys. Chem. Lett.* **2012**, *3* (17), 2476–2481. https://doi.org/10.1021/jz301059w.
(58) Li, G.; Abroshan, H.; Liu, C.; Zhuo, S.; Li, Z.; Xie, Y.; Kim, H. J.; Rosi, N. L.; Jin, R. Tailoring the Electronic and Catalytic Properties of Au25 Nanoclusters via Ligand Engineering. *ACS Nano* **2016**, *10* (8), 7998–8005. https://doi.org/10.1021/acsnano.6b03964.
(59) Wan, X.-K.; Wang, J.-Q.; Nan, Z.-A.; Wang, Q.-M. Ligand Effects in Catalysis by Atomically Precise Gold Nanoclusters. *Sci. Adv.* **2017**, *3* (10), e1701823. https://doi.org/10.1126/sciadv.1701823.
(60) Nasaruddin, R. R.; Chen, T.; Yan, N.; Xie, J. Roles of Thiolate Ligands in the Synthesis, Properties and Catalytic Application of Gold Nanoclusters. *Coord. Chem. Rev.* **2018**, *368*, 60–79. https://doi.org/10.1016/j.ccr.2018.04.016.
(61) Collins, C. B.; Tofanelli, M. A.; Crook, M. F.; Phillips, B. D.; Ackerson, C. J. Practical Stability of Au25(SR)18−1/0/+1. *RSC Adv.* **2017**, *7* (71), 45061–45065. https://doi.org/10.1039/C7RA07511A.
(62) Parrish, K. A.; King, M.; Ligare, M. R.; Johnson, G. E.; Hernández, H. Role of Sterics in Phosphine-Ligated Gold Clusters. *Phys. Chem. Chem. Phys.* **2019**, *21* (4), 1689–1699. https://doi.org/10.1039/C8CP04961K.
(63) Bertorelle, F.; Russier-Antoine, I.; Comby-Zerbino, C.; Chirot, F.; Dugourd, P.; Brevet, P.-F.; Antoine, R. Isomeric Effect of Mercaptobenzoic Acids on the Synthesis, Stability, and Optical Properties of Au25(MBA)18 Nanoclusters. *ACS Omega* **2018**, *3* (11), 15635–15642. https://doi.org/10.1021/acsomega.8b02615.
(64) Chen, Y.; Zeng, C.; Kauffman, D. R.; Jin, R. Tuning the Magic Size of Atomically Precise Gold Nanoclusters via Isomeric Methylbenzenethiols. *Nano Lett.* **2015**, *15* (5), 3603–3609. https://doi.org/10.1021/acs.nanolett.5b01122.
(65) Tero, T.-R.; Malola, S.; Koncz, B.; Pohjolainen, E.; Lautala, S.; Mustalahti, S.; Permi, P.; Groenhof, G.; Pettersson, M.; Häkkinen, H. Dynamic Stabilization of the Ligand–Metal Interface in Atomically Precise Gold Nanoclusters Au68 and Au144 Protected

by Meta-Mercaptobenzoic Acid. *ACS Nano* **2017**, *11* (12), 11872–11879. https://doi.org/10.1021/acsnano.7b07787.
(66) Ackerson, C. J.; Jadzinsky, P. D.; Sexton, J. Z.; Bushnell, D. A.; Kornberg, R. D. Synthesis and Bioconjugation of 2 and 3 Nm-Diameter Gold Nanoparticles. *Bioconjug. Chem.* **2010**, *21* (2), 214–218. https://doi.org/10.1021/bc900135d.
(67) Marjomäki, V.; Lahtinen, T.; Martikainen, M.; Koivisto, J.; Malola, S.; Salorinne, K.; Pettersson, M.; Häkkinen, H. Site-Specific Targeting of Enterovirus Capsid by Functionalized Monodisperse Gold Nanoclusters. *Proc. Natl. Acad. Sci.* **2014**, *111* (4), 1277–1281. https://doi.org/10.1073/pnas.1310973111.
(68) Kango, S.; Kalia, S.; Celli, A.; Njuguna, J.; Habibi, Y.; Kumar, R. Surface Modification of Inorganic Nanoparticles for Development of Organic–Inorganic Nanocomposites—A Review. *Prog. Polym. Sci.* **2013**, *38* (8), 1232–1261. https://doi.org/10.1016/j.progpolymsci.2013.02.003.
(69) Yuan, X.; Goswami, N.; Chen, W.; Yao, Q.; Xie, J. Insights into the Effect of Surface Ligands on the Optical Properties of Thiolated Au25 Nanoclusters. *Chem. Commun.* **2016**, *52* (30), 5234–5237. https://doi.org/10.1039/C6CC00857G.
(70) Nimmala, P. R.; Theivendran, S.; Barcaro, G.; Sementa, L.; Kumara, C.; Jupally, V. R.; Apra, E.; Stener, M.; Fortunelli, A.; Dass, A. Transformation of Au144(SCH2CH2Ph)60 to Au133(SPh-TBu)52 Nanomolecules: Theoretical and Experimental Study. *J. Phys. Chem. Lett.* **2015**, *6* (11), 2134–2139. https://doi.org/10.1021/acs.jpclett.5b00780.
(71) Zeng, C.; Liu, C.; Pei, Y.; Jin, R. Thiol Ligand-Induced Transformation of Au38(SC2H4Ph)24 to Au36(SPh-t-Bu)24. *ACS Nano* **2013**, *7* (7), 6138–6145. https://doi.org/10.1021/nn401971g.
(72) Higaki, T.; Liu, C.; Zhou, M.; Luo, T.-Y.; Rosi, N. L.; Jin, R. Tailoring the Structure of 58-Electron Gold Nanoclusters: Au103S2(S-Nap)41 and Its Implications. *J. Am. Chem. Soc.* **2017**, *139* (29), 9994–10001. https://doi.org/10.1021/jacs.7b04678.
(73) Dass, A.; Jones, T. C.; Theivendran, S.; Sementa, L.; Fortunelli, A. Core Size Interconversions of Au30(S-TBu)18 and Au36(SPhX)24. *J. Phys. Chem. C* **2017**, *121* (27), 14914–14919. https://doi.org/10.1021/acs.jpcc.7b03860.
(74) Meng, X.; Xu, Q.; Wang, S.; Zhu, M. Ligand-Exchange Synthesis of Selenophenolate-Capped Au25 Nanoclusters. *Nanoscale* **2012**, *4* (14), 4161–4165. https://doi.org/10.1039/C2NR30272A.
(75) Niihori, Y.; Kikuchi, Y.; Kato, A.; Matsuzaki, M.; Negishi, Y. Understanding Ligand-Exchange Reactions on Thiolate-Protected Gold Clusters by Probing Isomer Distributions Using Reversed-Phase High-Performance Liquid Chromatography. *ACS Nano* **2015**, *9* (9), 9347–9356. https://doi.org/10.1021/acsnano.5b03435.
(76) Salassa, G.; Sels, A.; Mancin, F.; Bürgi, T. Dynamic Nature of Thiolate Monolayer in Au25(SR)18 Nanoclusters. *ACS Nano* **2017**, *11* (12), 12609–12614. https://doi.org/10.1021/acsnano.7b06999.
(77) Salorinne, K.; Malola, S.; Wong, O. A.; Rithner, C. D.; Chen, X.; Ackerson, C. J.; Häkkinen, H. Conformation and Dynamics of the Ligand Shell of a Water-Soluble Au_{102} Nanoparticle. *Nat. Commun.* **2016**, *7*, 10401. https://doi.org/10.1038/ncomms10401.
(78) Chevrier, D. M.; Raich, L.; Rovira, C.; Das, A.; Luo, Z.; Yao, Q.; Chatt, A.; Xie, J.; Jin, R.; Akola, J.; et al. Molecular-Scale Ligand Effects in Small Gold–Thiolate

Nanoclusters. *J. Am. Chem. Soc.* **2018**, *140* (45), 15430–15436. https://doi.org/10.1021/jacs.8b09440.
(79) Lin, Y.; Charchar, P.; Christofferson, A. J.; Thomas, M. R.; Todorova, N.; Mazo, M. M.; Chen, Q.; Doutch, J.; Richardson, R.; Yarovsky, I.; et al. Surface Dynamics and Ligand–Core Interactions of Quantum Sized Photoluminescent Gold Nanoclusters. *J. Am. Chem. Soc.* **2018**, *140* (51), 18217–18226. https://doi.org/10.1021/jacs.8b04436.
(80) Chen, T.; Yang, S.; Chai, J.; Song, Y.; Fan, J.; Rao, B.; Sheng, H.; Yu, H.; Zhu, M. Crystallization-Induced Emission Enhancement: A Novel Fluorescent Au-Ag Bimetallic Nanocluster with Precise Atomic Structure. *Sci. Adv.* **2017**, *3* (8), e1700956. https://doi.org/10.1126/sciadv.1700956.
(81) Shi, L.; Zhu, L.; Guo, J.; Zhang, L.; Shi, Y.; Zhang, Y.; Hou, K.; Zheng, Y.; Zhu, Y.; Lv, J.; et al. Self-Assembly of Chiral Gold Clusters into Crystalline Nanocubes of Exceptional Optical Activity. *Angew. Chem. Int. Ed.* **2017**, *56* (48), 15397–15401. https://doi.org/10.1002/anie.201709827.
(82) Vanzan, M.; Corni, S. Role of Organic Ligands Orientation on the Geometrical and Optical Properties of Au25(SCH3)180. *J. Phys. Chem. A* **2018**, *122* (34), 6864–6872. https://doi.org/10.1021/acs.jpca.8b01797.
(83) Chen, H.; Liu, C.; Wang, M.; Zhang, C.; Luo, N.; Wang, Y.; Abroshan, H.; Li, G.; Wang, F. Visible Light Gold Nanocluster Photocatalyst: Selective Aerobic Oxidation of Amines to Imines. *ACS Catal.* **2017**, *7* (5), 3632–3638. https://doi.org/10.1021/acscatal.6b03509.
(84) Austin, N.; Zhao, S.; McKone, J. R.; Jin, R.; Mpourmpakis, G. Elucidating the Active Sites for CO2 Electroreduction on Ligand-Protected Au25 Nanoclusters. *Catal. Sci. Technol.* **2018**, *8* (15), 3795–3805. https://doi.org/10.1039/C8CY01099D.
(85) Wu, Z.; Jiang, D.; Mann, A. K. P.; Mullins, D. R.; Qiao, Z.-A.; Allard, L. F.; Zeng, C.; Jin, R.; Overbury, S. H. Thiolate Ligands as a Double-Edged Sword for CO Oxidation on CeO2 Supported Au25(SCH2CH2Ph)18 Nanoclusters. *J. Am. Chem. Soc.* **2014**, *136* (16), 6111–6122. https://doi.org/10.1021/ja5018706.
(86) Nasaruddin, R. R.; Yao, Q.; Chen, T.; Hülsey, M. J.; Yan, N.; Xie, J. Hydride-Induced Ligand Dynamic and Structural Transformation of Gold Nanoclusters during a Catalytic Reaction. *Nanoscale* **2018**, *10* (48), 23113–23121. https://doi.org/10.1039/C8NR07197G.
(87) Ackerson, C. J.; Jadzinsky, P. D.; Jensen, G. J.; Kornberg, R. D. Rigid, Specific, and Discrete Gold Nanoparticle/Antibody Conjugates. *J. Am. Chem. Soc.* **2006**, *128* (8), 2635–2640. https://doi.org/10.1021/ja0555668.
(88) Aubin-Tam, M.-E.; Hwang, W.; Hamad-Schifferli, K. Site-Directed Nanoparticle Labeling of Cytochrome c. *Proc. Natl. Acad. Sci.* **2009**, *106* (11), 4095–4100. https://doi.org/10.1073/pnas.0807299106.
(89) Mathew-Fenn, R. S.; Das, R.; Harbury, P. A. B. Remeasuring the Double Helix. *Science* **2008**, *322* (5900), 446–449. https://doi.org/10.1126/science.1158881.
(90) Polymer/Gold Hybrid Nanoparticles: From Synthesis to Cancer Theranostic Applications - RSC Advances (RSC Publishing).
(91) Mieszawska, A. J.; Mulder, W. J. M.; Fayad, Z. A.; Cormode, D. P. Multifunctional Gold Nanoparticles for Diagnosis and Therapy of Disease. *Mol. Pharm.* **2013**, *10* (3), 831–847. https://doi.org/10.1021/mp3005885.

(92) Kango et Al. - 2013 - Surface Modification of Inorganic Nanoparticles Fo.Pdf.
(93) Korala et Al. - 2017 - Ligand-Exchanged CZTS Nanocrystal Thin Films Does.Pdf.
(94) Kuno et Al. - 1997 - The Band Edge Luminescence of Surface Modified CdS.Pdf.
(95) Knoppe, S.; Dolamic, I.; Bürgi, T. Racemization of a Chiral Nanoparticle Evidences the Flexibility of the Gold–Thiolate Interface. *J. Am. Chem. Soc.* **2012**, *134* (31), 13114–13120. https://doi.org/10.1021/ja3053865.
(96) Carney, R. P.; DeVries, G. A.; Dubois, C.; Kim, H.; Kim, J. Y.; Singh, C.; Ghorai, P. K.; Tracy, J. B.; Stiles, R. L.; Murray, R. W.; et al. Size Limitations for the Formation of Ordered Striped Nanoparticles. *J. Am. Chem. Soc.* **2008**, *130* (3), 798–799. https://doi.org/10.1021/ja077383m.
(97) Boal, A. K.; Rotello, V. M. Radial Control of Recognition and Redox Processes with Multivalent Nanoparticle Hosts. *J. Am. Chem. Soc.* **2002**, *124* (18), 5019–5024. https://doi.org/10.1021/ja016894k.
(98) Ionita, P.; Volkov, A.; Jeschke, G.; Chechik, V. Lateral Diffusion of Thiol Ligands on the Surface of Au Nanoparticles: An Electron Paramagnetic Resonance Study. *Anal. Chem.* **2008**, *80* (1), 95–106. https://doi.org/10.1021/ac071266s.
(99) Kabsch, W. XDS. *Acta Crystallogr. D Biol. Crystallogr.* **2010**, *66* (2), 125–132. https://doi.org/10.1107/S0907444909047337.
(100) Sheldrick, G. M. A Short History of SHELX. *Acta Crystallogr. A* **2008**, *64* (1), 112–122. https://doi.org/10.1107/S0108767307043930.
(101) Natarajan, G.; Mathew, A.; Negishi, Y.; Whetten, R. L.; Pradeep, T. A Unified Framework for Understanding the Structure and Modifications of Atomically Precise Monolayer Protected Gold Clusters. *J. Phys. Chem. C* **2015**, *119* (49), 27768–27785. https://doi.org/10.1021/acs.jpcc.5b08193.
(102) Yee, C. K.; Ulman, A.; Ruiz, J. D.; Parikh, A.; White, H.; Rafailovich, M. Alkyl Selenide- and Alkyl Thiolate-Functionalized Gold Nanoparticles: Chain Packing and Bond Nature. *Langmuir* **2003**, *19* (22), 9450–9458. https://doi.org/10.1021/la020628i.
(103) de la Llave, E.; Scherlis, D. A. Selenium-Based Self-Assembled Monolayers: The Nature of Adsorbate−Surface Interactions. *Langmuir* **2010**, *26* (1), 173–178. https://doi.org/10.1021/la903660y.
(104) Heaven, M. W.; Dass, A.; White, P. S.; Holt, K. M.; Murray, R. W. Crystal Structure of the Gold Nanoparticle [N(C8H17)4][Au25(SCH2CH2Ph)18]. *J. Am. Chem. Soc.* **2008**, *130* (12), 3754–3755. https://doi.org/10.1021/ja800561b.
(105) Song, Y.; Zhong, J.; Yang, S.; Wang, S.; Cao, T.; Zhang, J.; Li, P.; Hu, D.; Pei, Y.; Zhu, M. Crystal Structure of Au25(SePh)18 Nanoclusters and Insights into Their Electronic, Optical and Catalytic Properties. *Nanoscale* **2014**, *6* (22), 13977–13985. https://doi.org/10.1039/C4NR04631E.
(106) Luo, Z.; Hou, J.; Menin, L.; Ong, Q. K.; Stellacci, F. Evolution of the Ligand Shell Morphology during Ligand Exchange Reactions on Gold Nanoparticles. *Angew. Chem. Int. Ed.* **2017**, *56* (43), 13521–13525. https://doi.org/10.1002/anie.201708190.
(107) Ouyang, R.; Jiang, D. Ligand-Conformation Energy Landscape of Thiolate-Protected Gold Nanoclusters. *J. Phys. Chem. C* **2015**, *119* (37), 21555–21560. https://doi.org/10.1021/acs.jpcc.5b06994.

(108) Pohjolainen, E.; Chen, X.; Malola, S.; Groenhof, G.; Häkkinen, H. A Unified AMBER-Compatible Molecular Mechanics Force Field for Thiolate-Protected Gold Nanoclusters. *J. Chem. Theory Comput.* **2016**, *12* (3), 1342–1350. https://doi.org/10.1021/acs.jctc.5b01053.
(109) Zhu, M.; Eckenhoff, W. T.; Pintauer, T.; Jin, R. Conversion of Anionic [Au25(SCH2CH2Ph)18]− Cluster to Charge Neutral Cluster via Air Oxidation. *J. Phys. Chem. C* **2008**, *112* (37), 14221–14224. https://doi.org/10.1021/jp805786p.
(110) Tofanelli, M. A.; Salorinne, K.; Ni, T. W.; Malola, S.; Newell, B.; Phillips, B.; Häkkinen, H.; Ackerson, C. J. Jahn–Teller Effects in Au25(SR)18. *Chem. Sci.* **2016**, *7* (3), 1882–1890. https://doi.org/10.1039/C5SC02134K.
(111) Krishnadas, K. R.; Baksi, A.; Ghosh, A.; Natarajan, G.; Som, A.; Pradeep, T. Interparticle Reactions: An Emerging Direction in Nanomaterials Chemistry. *Acc. Chem. Res.* **2017**, *50* (8), 1988–1996. https://doi.org/10.1021/acs.accounts.7b00224.
(112) Shang, L.; Nienhaus, G. U. Metal Nanoclusters: Protein Corona Formation and Implications for Biological Applications. *Int. J. Biochem. Cell Biol.* **2016**, *75*, 175–179. https://doi.org/10.1016/j.biocel.2015.09.007.
(113) Dreier, T. A.; Wong, O. A.; Ackerson, C. J. Oxidative Decomposition of Au25(SR)18 Clusters in a Catalytic Context. *Chem. Commun.* **2014**, *51* (7), 1240–1243. https://doi.org/10.1039/C4CC07832B.
(114) Tang, Q.; Jiang, D. Insights into the PhC≡C/Au Interface. *J. Phys. Chem. C* **2015**, *119* (20), 10804–10810. https://doi.org/10.1021/jp508883v.
(115) Bejarano, F.; Olavarria-Contreras, I. J.; Droghetti, A.; Rungger, I.; Rudnev, A.; Gutiérrez, D.; Mas-Torrent, M.; Veciana, J.; van der Zant, H. S. J.; Rovira, C.; et al. Robust Organic Radical Molecular Junctions Using Acetylene Terminated Groups for C–Au Bond Formation. *J. Am. Chem. Soc.* **2018**, *140* (5), 1691–1696. https://doi.org/10.1021/jacs.7b10019.
(116) Zaba, T.; Noworolska, A.; Bowers, C. M.; Breiten, B.; Whitesides, G. M.; Cyganik, P. Formation of Highly Ordered Self-Assembled Monolayers of Alkynes on Au(111) Substrate. *J. Am. Chem. Soc.* **2014**, *136* (34), 11918–11921. https://doi.org/10.1021/ja506647p.
(117) Lei, Z.; Wan, X.-K.; Yuan, S.-F.; Guan, Z.-J.; Wang, Q.-M. Alkynyl Approach toward the Protection of Metal Nanoclusters. *Acc. Chem. Res.* **2018**, *51* (10), 2465–2474. https://doi.org/10.1021/acs.accounts.8b00359.
(118) Maity, P.; Tsunoyama, H.; Yamauchi, M.; Xie, S.; Tsukuda, T. Organogold Clusters Protected by Phenylacetylene. *J. Am. Chem. Soc.* **2011**, *133* (50), 20123–20125. https://doi.org/10.1021/ja209236n.
(119) Maity, P.; Wakabayashi, T.; Ichikuni, N.; Tsunoyama, H.; Xie, S.; Yamauchi, M.; Tsukuda, T. Selective Synthesis of Organogold Magic Clusters Au54(CCPh)26. *Chem. Commun.* **2012**, *48* (49), 6085–6087. https://doi.org/10.1039/C2CC18153C.
(120) Maity, P.; Takano, S.; Yamazoe, S.; Wakabayashi, T.; Tsukuda, T. Binding Motif of Terminal Alkynes on Gold Clusters. *J. Am. Chem. Soc.* **2013**, *135* (25), 9450–9457. https://doi.org/10.1021/ja401798z.
(121) Sugiuchi, M.; Shichibu, Y.; Nakanishi, T.; Hasegawa, Y.; Konishi, K. Cluster–π Electronic Interaction in a Superatomic Au13 Cluster Bearing σ-Bonded Acetylide

Ligands. *Chem. Commun.* **2015**, *51* (70), 13519–13522. https://doi.org/10.1039/C5CC04312C.
(122) Wan, X.-K.; Tang, Q.; Yuan, S.-F.; Jiang, D.; Wang, Q.-M. Au19 Nanocluster Featuring a V-Shaped Alkynyl–Gold Motif. *J. Am. Chem. Soc.* **2015**, *137* (2), 652–655. https://doi.org/10.1021/ja512133a.
(123) Wang, J.-Q.; Guan, Z.-J.; Liu, W.-D.; Yang, Y.; Wang, Q.-M. Chiroptical Activity Enhancement via Structural Control: The Chiral Synthesis and Reversible Interconversion of Two Intrinsically Chiral Gold Nanoclusters. *J. Am. Chem. Soc.* **2019**, *141* (6), 2384–2390. https://doi.org/10.1021/jacs.8b11096.
(124) An Intermetallic Au24Ag20 Superatom Nanocluster Stabilized by Labile Ligands - Journal of the American Chemical Society (ACS Publications) https://pubs.acs.org/doi/abs/10.1021/jacs.5b01232 (accessed Feb 27, 2019).
(125) Zhu, Y.; Jin, R.; Sun, Y. Atomically Monodisperse Gold Nanoclusters Catalysts with Precise Core-Shell Structure. *Catalysts* **2011**, *1* (1), 3–17. https://doi.org/10.3390/catal1010003.
(126) Zhu, Y.; Qian, H.; Jin, R. Catalysis Opportunities of Atomically Precise Gold Nanoclusters. *J. Mater. Chem.* **2011**, *21* (19), 6793–6799. https://doi.org/10.1039/C1JM10082C.
(127) Heterogeneous Catalysis by Gold and Gold-Based Bimetal Nanoclusters. *Nano Today* **2018**, *18*, 86–102. https://doi.org/10.1016/j.nantod.2017.12.009.
(128) Fang, J.; Zhang, B.; Yao, Q.; Yang, Y.; Xie, J.; Yan, N. Recent Advances in the Synthesis and Catalytic Applications of Ligand-Protected, Atomically Precise Metal Nanoclusters. *Coord. Chem. Rev.* **2016**, *322*, 1–29. https://doi.org/10.1016/j.ccr.2016.05.003.
(129) Liu, J.; Krishna, K. S.; Losovyj, Y. B.; Chattopadhyay, S.; Lozova, N.; Miller, J. T.; Spivey, J. J.; Kumar, C. S. S. R. Ligand-Stabilized and Atomically Precise Gold Nanocluster Catalysis: A Case Study for Correlating Fundamental Electronic Properties with Catalysis. *Chem. – Eur. J.* **2013**, *19* (31), 10201–10208. https://doi.org/10.1002/chem.201300600.
(130) Nie, X.; Qian, H.; Ge, Q.; Xu, H.; Jin, R. CO Oxidation Catalyzed by Oxide-Supported Au25(SR)18 Nanoclusters and Identification of Perimeter Sites as Active Centers. *ACS Nano* **2012**, *6* (7), 6014–6022. https://doi.org/10.1021/nn301019f.
(131) Chong, H.; Li, P.; Wang, S.; Fu, F.; Xiang, J.; Zhu, M.; Li, Y. Au_{25} Clusters as Electron-Transfer Catalysts Induced the Intramolecular Cascade Reaction of 2-Nitrobenzonitrile. *Sci. Rep.* **2013**, *3*, 3214. https://doi.org/10.1038/srep03214.
(132) Chong, H.; Zhu, M. Catalytic Reduction by Quasi-Homogeneous Gold Nanoclusters in the Liquid Phase. *ChemCatChem* **2015**, *7* (15), 2296–2304. https://doi.org/10.1002/cctc.201500247.
(133) Li, G.; Liu, C.; Lei, Y.; Jin, R. Au25 Nanocluster-Catalyzed Ullmann-Type Homocoupling Reaction of Aryl Iodides. *Chem. Commun.* **2012**, *48* (98), 12005–12007. https://doi.org/10.1039/C2CC34765B.
(134) Li, Q.; Das, A.; Wang, S.; Chen, Y.; Jin, R. Highly Efficient Three-Component Coupling Reaction Catalysed by Atomically Precise Ligand-Protected Au38(SC2H4Ph)24 Nanoclusters. *Chem. Commun.* **2016**, *52* (99), 14298–14301. https://doi.org/10.1039/C6CC07825G.

(135) Li, G.; Jiang, D.; Liu, C.; Yu, C.; Jin, R. Oxide-Supported Atomically Precise Gold Nanocluster for Catalyzing Sonogashira Cross-Coupling. *J. Catal.* **2013**, *306*, 177–183. https://doi.org/10.1016/j.jcat.2013.06.017.
(136) Li, G.; Jiang, D.; Kumar, S.; Chen, Y.; Jin, R. Size Dependence of Atomically Precise Gold Nanoclusters in Chemoselective Hydrogenation and Active Site Structure. *ACS Catal.* **2014**, *4* (8), 2463–2469. https://doi.org/10.1021/cs500533h.
(137) Li, J.; Nasaruddin, R. R.; Feng, Y.; Yang, J.; Yan, N.; Xie, J. Tuning the Accessibility and Activity of Au25(SR)18 Nanocluster Catalysts through Ligand Engineering. *Chem. – Eur. J.* **2016**, *22* (42), 14816–14820. https://doi.org/10.1002/chem.201603247.
(138) Roles of Thiolate Ligands in the Synthesis, Properties and Catalytic Application of Gold Nanoclusters. *Coord. Chem. Rev.* **2018**, *368*, 60–79. https://doi.org/10.1016/j.ccr.2018.04.016.
(139) Li, Z.; Liu, C.; Abroshan, H.; Kauffman, D. R.; Li, G. Au38S2(SAdm)20 Photocatalyst for One-Step Selective Aerobic Oxidations. *ACS Catal.* **2017**, *7* (5), 3368–3374. https://doi.org/10.1021/acscatal.7b00239.
(140) Li, G.; Qian, H.; Jin, R. Gold Nanocluster-Catalyzed Selective Oxidation of Sulfide to Sulfoxide. *Nanoscale* **2012**, *4* (21), 6714–6717. https://doi.org/10.1039/C2NR32171H.
(141) Hermes, J. P.; Sander, F.; Peterle, T.; Urbani, R.; Pfohl, T.; Thompson, D.; Mayor, M. Gold Nanoparticles Stabilized by Thioether Dendrimers. *Chem. – Eur. J.* **2011**, *17* (48), 13473–13481. https://doi.org/10.1002/chem.201101837.
(142) Feineis, S.; Lutz, J.; Heffele, L.; Endl, E.; Albrecht, K.; Groll, J. Thioether–Polyglycidol as Multivalent and Multifunctional Coating System for Gold Nanoparticles. *Adv. Mater.* **2018**, *30* (8), 1704972. https://doi.org/10.1002/adma.201704972.
(143) Peters, E. H.; Lehmann, M.; Mayor, M. Gold Nanoparticles Stabilized by Single Tripodal Ligands. *Part. Part. Syst. Charact.* **2018**, *35* (4), 1800015. https://doi.org/10.1002/ppsc.201800015.
(144) Abdoul-Carime, H.; Bald, I.; Illenberger, E.; Kopyra, J. Selective Synthesis of Ethylene and Acetylene from Dimethyl Sulfide Cold Films Controlled by Slow Electrons. *J. Phys. Chem. C* **2018**, *122* (42), 24137–24142. https://doi.org/10.1021/acs.jpcc.8b07377.
(145) Duffield, A. M.; Budzikiewicz, H.; Djerassi, C. Mass Spectrometry in Structural and Stereochemical Problems. LXXI.1 A Study of the Influence of Different Heteroatoms on the Mass Spectrometric Fragmentation of Five-Membered Heterocycles2. *J. Am. Chem. Soc.* **1965**, *87* (13), 2920–2926. https://doi.org/10.1021/ja01091a023.
(146) Li, M.-B.; Tian, S.-K.; Wu, Z. Catalyzed Formation of α,β-Unsaturated Ketones or Aldehydes from Propargylic Acetates by a Recoverable and Recyclable Nanocluster Catalyst. *Nanoscale* **2014**, *6* (11), 5714–5717. https://doi.org/10.1039/C4NR00658E.
(147) Zhang, B.; Kaziz, S.; Li, H.; Hevia, M. G.; Wodka, D.; Mazet, C.; Bürgi, T.; Barrabés, N. Modulation of Active Sites in Supported Au38(SC2H4Ph)24 Cluster Catalysts: Effect of Atmosphere and Support Material. *J. Phys. Chem. C* **2015**, *119* (20), 11193–11199. https://doi.org/10.1021/jp512022v.

(148) Abdoul-Carime, H.; Rabilloud, F. Selective Desorption of Ethylene after Dimethyl Sulfide Reaction on Cold Gold Surface. *J. Phys. Chem. C* **2019**, *123* (3), 1874–1879. https://doi.org/10.1021/acs.jpcc.8b11311.
(149) Laurentius, L.; Stoyanov, S. R.; Gusarov, S.; Kovalenko, A.; Du, R.; Lopinski, G. P.; McDermott, M. T. Diazonium-Derived Aryl Films on Gold Nanoparticles: Evidence for a Carbon–Gold Covalent Bond. *ACS Nano* **2011**, *5* (5), 4219–4227. https://doi.org/10.1021/nn201110r.
(150) Tijunelyte, I.; Kherbouche, I.; Gam-Derouich, S.; Nguyen, M.; Lidgi-Guigui, N.; Chapelle, M. L. de la; Lamouri, A.; Lévi, G.; Aubard, J.; Chevillot-Biraud, A.; et al. Multi-Functionalization of Lithographically Designed Gold Nanodisks by Plasmon-Mediated Reduction of Aryl Diazonium Salts. *Nanoscale Horiz.* **2017**, *3* (1), 53–57. https://doi.org/10.1039/C7NH00113D.
(151) Guo, L.; Ma, L.; Zhang, Y.; Cheng, X.; Xu, Y.; Wang, J.; Wang, E.; Peng, Z. Spectroscopic Identification of the Au–C Bond Formation upon Electroreduction of an Aryl Diazonium Salt on Gold. *Langmuir* **2016**, *32* (44), 11514–11519. https://doi.org/10.1021/acs.langmuir.6b03206.
(152) Ahmad, R.; Boubekeur-Lecaque, L.; Nguyen, M.; Lau-Truong, S.; Lamouri, A.; Decorse, P.; Galtayries, A.; Pinson, J.; Felidj, N.; Mangeney, C. Tailoring the Surface Chemistry of Gold Nanorods through Au–C/Ag–C Covalent Bonds Using Aryl Diazonium Salts. *J. Phys. Chem. C* **2014**, *118* (33), 19098–19105. https://doi.org/10.1021/jp504040d.
(153) Visscher, P. T.; Taylor, B. F. A New Mechanism for the Aerobic Catabolism of Dimethyl Sulfide. *Appl Env. Microbiol* **1993**, *59* (11), 3784–3789.
(154) Kawasaki, H.; Kumar, S.; Li, G.; Zeng, C.; Kauffman, D. R.; Yoshimoto, J.; Iwasaki, Y.; Jin, R. Generation of Singlet Oxygen by Photoexcited Au25(SR)18 Clusters. *Chem. Mater.* **2014**, *26* (9), 2777–2788. https://doi.org/10.1021/cm500260z.
(155) Liu, C.; Yan, C.; Lin, J.; Yu, C.; Huang, J.; Li, G. One-Pot Synthesis of Au144(SCH2Ph)60 Nanoclusters and Their Catalytic Application. *J. Mater. Chem. A* **2015**, *3* (40), 20167–20173. https://doi.org/10.1039/C5TA05747G.
(156) Duffield, A. M.; Budzikiewicz, H.; Djerassi, C. Mass Spectrometry in Structural and Stereochemical Problems. LXXI.1 A Study of the Influence of Different Heteroatoms on the Mass Spectrometric Fragmentation of Five-Membered Heterocycles2. *J. Am. Chem. Soc.* **1965**, *87* (13), 2920–2926. https://doi.org/10.1021/ja01091a023.
(157) Knoppe, S.; Häkkinen, H.; Verbiest, T.; Clays, K. Role of Donor and Acceptor Substituents on the Nonlinear Optical Properties of Gold Nanoclusters. *J. Phys. Chem. C* **2018**, *122* (7), 4019–4028. https://doi.org/10.1021/acs.jpcc.7b12356.
(158) Knoppe, S.; Häkkinen, H.; Verbiest, T. Nonlinear Optical Properties of Thiolate-Protected Gold Clusters: A Theoretical Survey of the First Hyperpolarizabilities. *J. Phys. Chem. C* **2015**, *119* (49), 27676–27682. https://doi.org/10.1021/acs.jpcc.5b08341.
(159) Agrachev, M.; Antonello, S.; Dainese, T.; Ruzzi, M.; Zoleo, A.; Aprà, E.; Govind, N.; Fortunelli, A.; Sementa, L.; Maran, F. Magnetic Ordering in Gold Nanoclusters. *ACS Omega* **2017**, *2* (6), 2607–2617. https://doi.org/10.1021/acsomega.7b00472.
(160) Vippagunta, S. R.; Brittain, H. G.; Grant, D. J. W. Crystalline Solids. *Adv. Drug Deliv. Rev.* **2001**, *48* (1), 3–26. https://doi.org/10.1016/S0169-409X(01)00097-7.

(161) Wolff, H.-M.; Quere, L.; Riedner, J. Polymorphic Form of Rotigotine and Process for Production. US8232414B2, July 31, 2012.
(162) Chen, K.-J.; Tsai, Y.-C.; Suzaki, Y.; Osakada, K.; Miura, A.; Horie, M. Rapid and Reversible Photoinduced Switching of a Rotaxane Crystal. *Nat. Commun.* **2016**, *7*, 13321. https://doi.org/10.1038/ncomms13321.
(163) Chen, S.; Liu, H.; Li, Y.; Li, D.; Li, Y. Tuning Luminescence and Conductivity through Controlled Growth of Polymorphous Molecular Crystals. *Adv. Electron. Mater.* **2017**, *3* (11), 1700132. https://doi.org/10.1002/aelm.201700132.
(164) Yu, L. Polymorphism in Molecular Solids: An Extraordinary System of Red, Orange, and Yellow Crystals. *Acc. Chem. Res.* **2010**, *43* (9), 1257–1266. https://doi.org/10.1021/ar100040r.
(165) Liao, Q.; Wang, Z.; Gao, Q.; Zhang, Z.; Ren, J.; De, J.; Zhang, X.; Xu, Z.; Fu, H. The Effect of 1D- and 2D-Polymorphs on Organic Single-Crystal Optoelectronic Devices: Lasers and Field Effect Transistors. *J. Mater. Chem. C* **2018**, *6* (30), 7994–8002. https://doi.org/10.1039/C8TC01584H.
(166) Cruz-Cabeza, A. J.; Bernstein, J. Conformational Polymorphism. *Chem. Rev.* **2014**, *114* (4), 2170–2191. https://doi.org/10.1021/cr400249d.
(167) Knoppe, S.; Vanbel, M.; van Cleuvenbergen, S.; Vanpraet, L.; Bürgi, T.; Verbiest, T. Nonlinear Optical Properties of Thiolate-Protected Gold Clusters. *J. Phys. Chem. C* **2015**, *119* (11), 6221–6226. https://doi.org/10.1021/acs.jpcc.5b01475.
(168) Dolomanov, O. V.; Bourhis, L. J.; Gildea, R. J.; Howard, J. a. K.; Puschmann, H. OLEX2: A Complete Structure Solution, Refinement and Analysis Program. *J. Appl. Crystallogr.* **2009**, *42* (2), 339–341. https://doi.org/10.1107/S0021889808042726.
(169) DeVries, G. A.; Brunnbauer, M.; Hu, Y.; Jackson, A. M.; Long, B.; Neltner, B. T.; Uzun, O.; Wunsch, B. H.; Stellacci, F. Divalent Metal Nanoparticles. *Science* **2007**, *315* (5810), 358–361. https://doi.org/10.1126/science.1133162.
(170) Nag, A.; Chakraborty, P.; Bodiuzzaman, M.; Ahuja, T.; Antharjanam, S.; Pradeep, T. Polymorphism of Ag29(BDT)12(TPP)43− Cluster: Interactions of Secondary Ligands and Their Effect on Solid State Luminescence. *Nanoscale* **2018**, *10* (21), 9851–9855. https://doi.org/10.1039/C8NR02629G.
(171) Knoppe, S.; Verbiest, T. Resonance Enhancement of Nonlinear Optical Scattering in Monolayer-Protected Gold Clusters. *J. Am. Chem. Soc.* **2017**, *139* (42), 14853–14856. https://doi.org/10.1021/jacs.7b08338.
(172) Parker, J. F.; Weaver, J. E. F.; McCallum, F.; Fields-Zinna, C. A.; Murray, R. W. Synthesis of Monodisperse [Oct4N+][Au25(SR)18−] Nanoparticles, with Some Mechanistic Observations. *Langmuir* **2010**, *26* (16), 13650–13654. https://doi.org/10.1021/la1020466.

APPENDIX A: SUPPLEMENTARY TO CHAPTER 2

A.1 General Methods

Tetrachloroaurate trihydrate (Sigma-Aldrich, ACS reagent, ≥49.0% Au basis), tetra-*n*-octylammonium bromide (Acros Organics, 98% purity), sodium borohydride (Sigma-Aldrich, ≥98.0% purity), 2-phenylethanethiol (Sigma-Aldrich, ≥99% Purity), benzeneselenol (TCI America, >95% Purity), thiophenol (Alfa Aesar, 99+% Purity), tetrahydrofuran (Fisher Scientific, certified, stabilized with 0.025% butylated hydroxytoluene), dichloromethane (Sigma-Aldrich, ACS grade, ≥99.5%, stabilized with 40-150 ppm amylene), methanol (Fisher Scientific, certified ACS, 99.9% assay), *n*-butanol (Sigma-Aldrich, ≥99.9% Purity), *n*-pentanol (Sigma-Aldrich, 99.9+% Purity, ACS), and *trans*-2-[3-(4-*tert*-Butylphenyl)-2-methyl-2-propenyliden]malononitrile (Sigma Aldrich, ≥99.0% [HPLC]) were all used without further purification. Water was obtained using a Thermo Scientific Barnstead Nanopure set to 18.2 MΩ·cm.

A.2 Synthesis of $Au_{25}(PET)_{18}TOA$

This procedure was adapted from a previous report.[172] In brief, 2.0 g $HAuCl_4 \cdot 3H_2O$ and 3.12 g tetra-*n*-octylammonium bromide were added to 140 mL tetrahydrofuran in a 300 mL round bottom flask. The solution was stirred for 30 minutes until a dark orange color was observed. 3.6 mL of 2-phenylethanethiol was then added to flask, and the resulting solution was stirred overnight. A separate solution containing 1.94 g sodium borohydride and 48 mL H_2O was produced in a 125 mL Erlenmeyer flask. This solution was cooled to 0 ^oC prior to adding it to the gold-containing solution. The combined solutions were then stirred for 48 hours, followed by separation and evaporation of the

organic layer. The resulting brown oil was redissolved in several milliliters of dichloromethane and separated into four 50 mL conical vials. The conical vials were filled with methanol and placed in a centrifuge at 4000 RPM for 30 minutes. The supernatant was decanted and the precipitate was washed twice more by addition of methanol and centrifugation.

A.3 Synthesis of $Au_{25}(SePh)_{18}TOA$

Synthesis conditions were adapted from a previously published report.[74] In brief, 15.0 mg $Au_{25}(PET)_{18}TOA$ was added to 8.21 mL dichloromethane and 39.9 µL benzeneselenol in a 20 mL scintillation vial and stirred overnight at 4 °C. The solution was then evaporated to approximate dryness and was washed with excess methanol until the wash solution remained clear and free of odor and a fine black powder was obtained. This consisted of approximately ten washes with methanol. The product was then extracted with dichloromethane and evaporated to dryness.

A.4 Ligand Exchange Reactions on $Au_{25}(SePh)_{18}TOA$

Ligand exchange was performed on $Au_{25}(SePh)_{18}TOA$ by adding 6.0 mg (0.73 µmol) $Au_{25}(SePh)_{18}TOA$ to 1.47 mL dichloromethane in a 1.5 dram vial at room temperature. 0.074 µL thiophenol (0.080 mg, 0.73 µmol) was added to the solution containing the Au_{25} cluster and stirred for 30 minutes, after which the solvent was evaporated. The crude product was then washed with methanol to remove free ligands. This process was repeated until the wash remained free of color and smell, or approximately ten washes. The remaining crude product was subsequently extracted using dichloromethane and evaporated to dryness.

A similar procedure was used to generate a higher amount of ligand exchange, but using 7.5 μL (8.1 mg, 73 μmol) of thiophenol instead.

A.5 Synthesis of $Au_{25}(SePh)_{18-x}(SPh)_xTOA$ Crystals

The same procedure was used for crystallizing both 1 eq. PhSH exchange and 100 eq. PhSH exchange samples. Crystals were obtained by dissolving 10 mg $Au_{25}(SePh)_{18-x}(SPh)_xTOA$ in 1 mL dichloromethane in a 1.5 dram vial at room temperature. Approximately 2.5 mL *n*-pentanol was carefully added to the vial, making sure to minimize agitation of the nanocluster solution. The vial was sealed and allowed to sit for 5 days until the nanocluster solution and *n*-pentanol had fully mixed. The supernatant was then removed using a pipette, leaving dark rhombohedral crystals. Eight crystals were removed for single crystal x-ray diffraction analysis. The remaining material was recrystallized a second time with *n*-butanol as the anti-solvent to obtain crystal samples corresponding to 10 days of solution time. This process was repeated a third time with *n*-butanol as the anti-solvent to obtain crystal samples corresponding to 15 days of solution time.

A.6 MALDI-MS Data Collection and Spectra

2 mg *trans*-2-[3-(4-*tert*-Butylphenyl)-2-methyl-2-propenylidene]malononitrile was dissolved in 0.2 mL dichloromethane. To this solution was added 2.0 μL of nanocluster sample dissolved in dichloromethane. 0.2 μL of the combined solution was spotted on a metal plate for MALDI-MS and allowed dry for one hour. Data was collected using a Bruker Microflex LFR MALDI-TOF.

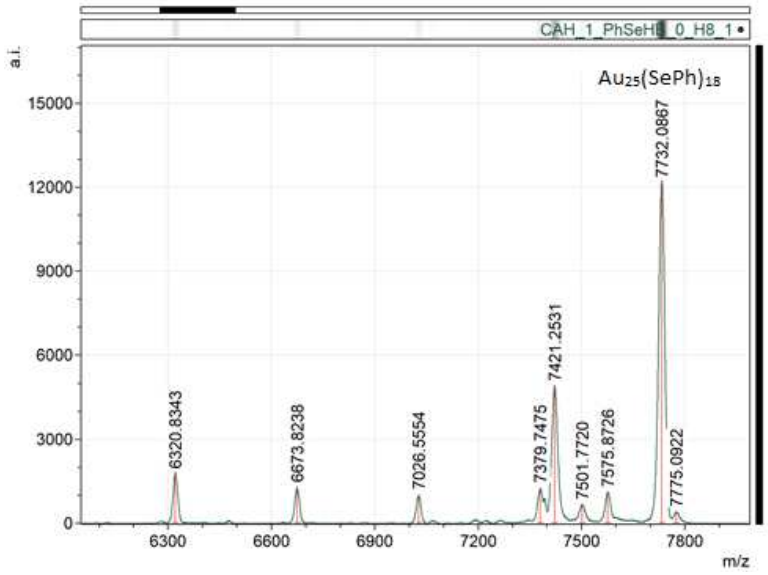


Figure A.1. MALDI-MS of $Au_{25}(SePh)_{18}TOA$. The peak corresponding to $Au_{25}(SePh)_{18}$ is labelled. All other peaks correspond to sodium adducts or fragmentation of $Au_{25}(SePh)_{18}$

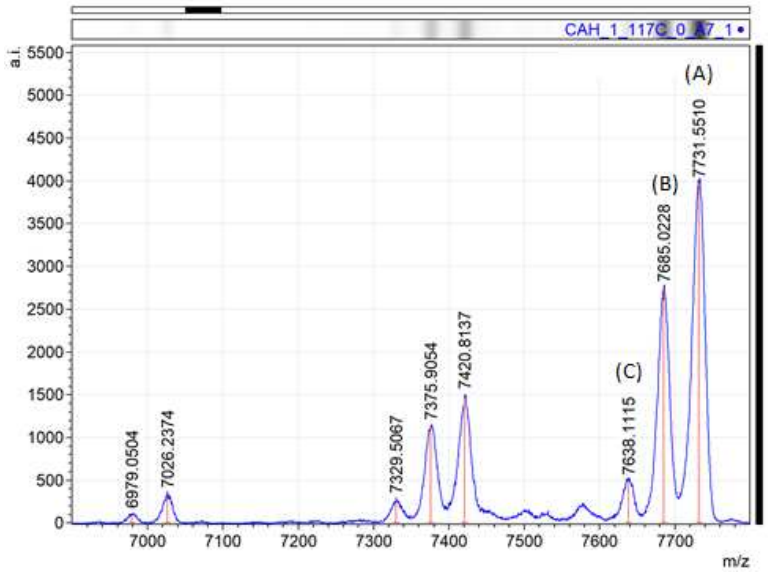


Figure A.2.: MALDI-MS result from exchange of $Au_{25}(SePh)_{18}TOA$ with 1 eq. PhSH after 30 minutes. Peak assignments are as follows: A) $Au_{25}(SePh)_{18}$ B) $Au_{25}(SePh)_{17}(SPh)_1$ C) $Au_{25}(SePh)_{16}(SPh)_2$. All other peaks correspond to fragmentation products of these compounds.

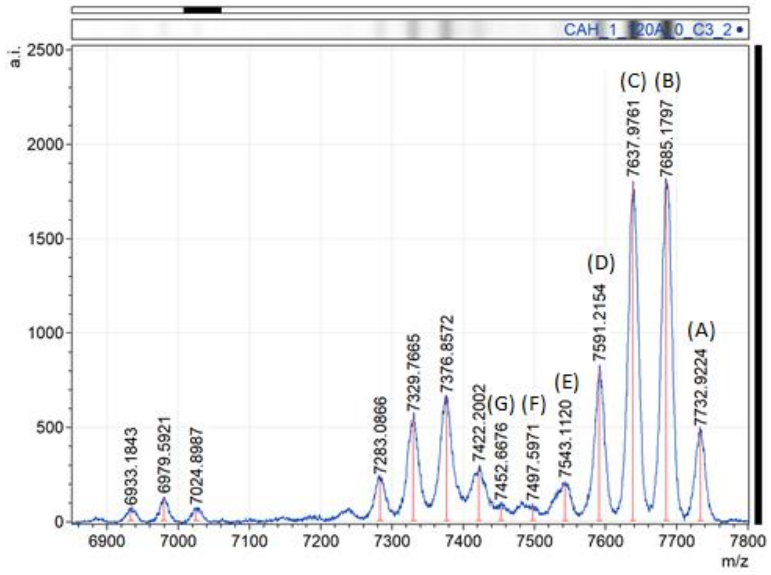


Figure A.3. MALDI-MS result from exchange of $Au_{25}(SePh)_{18}TOA$ with 100 eq. PhSH after 30 minutes. Peak assignments are as follows: A) $Au_{25}(SePh)_{18}$ B) $Au_{25}(SePh)_{17}(SPh)_1$ C)$Au_{25}(SePh)_{16}(SPh)_2$ D) $Au_{25}(SePh)_{15}(SPh)_3$ E) $Au_{25}(SePh)_{14}(SPh)_4$ F) $Au_{25}(SePh)_{13}(SPh)_5$ G) $Au_{25}(SePh)_{12}(SPh)_6$. All other peaks correspond to fragmentation products of these compounds.

A.7 Single Crystal X-Ray Diffraction Data Collection and Workup

Data was collected at ALS Beamline 4.2.2 using an RDI_CMOS 8M detector with a 1.000 Å wavelength (12398.419 eV) at a distance of 100nm. Data was integrated and corrected using XDS. Data was refined through XPREP (v. 6.12; Bruker AXS; Madison, WI, 1999) and SHELX was used for solving the structure.[100] An overload threshold of 65000 was utilized when integrating data. SHELXT was used for initial determination of gold atoms in the nanocluster. Further solving of the crystal structure with a full-matrix least-squared against F^2 using SHELXL-2014/7 in SHELXTL (Bruker). Each structure was initially modeled with only selenium at the chalcogen positions. Ligand exchange percentages were then determined by modeling potential substitutional disorder of Se/S at each chalcogen atom position using EXYZ and EADP commands. Disorder at all chalcogen atoms was refined simultaneously. Any free variables which refined to zero or

negative values were removed and the corresponding chalcogen atom was deemed to have no exchange. Positions which contained less than 4% exchange were deemed to have no exchange in accordance with previous practice and are shown as having zero percent exchange.[28]

A.8 Solvent Accessibility Calculations

Values were obtained utilizing the PyMOL Molecular Graphics system (version 2.0, Schrödinger LLC) using a dot_density of 4 and a probe radius of 1.8 corresponding to the van der Waals radius of sulfur. All atoms corresponding to the tetra-*n*-octylammonium counterion were temporarily removed from the model prior to determining solvent accessibility values when possible. Solvent accessibility values for all connected gold atoms were summed to provide the solvent accessibility values listed for each ligand in tables 1 and 2.

A.9 Crystallographic Ligand Exchange Results

Table A.1. Sulfur occupancy percentages at the chalcogen atom position of each ligand in crystal structures obtained after two crystallizations (10 days) post-exchange with 1 eq. PhSH.

	CH7-02	CH7-03	CH8-03
D1-1	4.5%	0%	0%
D1-3	11.7%	9.8%	7.9%
D1-5	8.7%	12.0%	9.7%
D2-1	5.6%	0%	0%
D2-3	9.9%	11.8%	12.3%
D2-5	0%	0%	0%
D3-1	0%	0%	0%
D3-3	11.1%	6.9%	14.3%
D3-5	0%	4.3%	0%
D4-1	8.8%	0%	0%
D4-3	12.7%	9.5%	14.3%
D4-5	6.6%	7.3%	5.0%
D5-1	0%	0%	0%
D5-3	5.5%	14.9%	7.4%
D5-5	21.3%	15.0%	20.1%
D6-1	0%	0%	0%
D6-3	0%	9.5%	0%
D6-5	21.0%	19.9%	20.3%

Table A.2. Sulfur occupancy percentages at the chalcogen atom position of each ligand in crystal structures obtained after three crystallizations (15 days) post-exchange with 1 eq. PhSH.

	CH13-01	CH14-02	CH14-03
D1-1	6.9%	0%	7.4%
D1-3	10.1%	12.4%	8.0%
D1-5	11.9%	16.0%	15.9%
D2-1	0%	5.4%	4.8%
D2-3	7.9%	10.2%	5.9%
D2-5	0%	0%	5.1%
D3-1	0%	8.1%	6.6%
D3-3	11.3%	8.9%	12.1%
D3-5	0%	4.5%	0%
D4-1	9.8%	9.2%	9.6%
D4-3	16.8%	9.3%	10.2%
D4-5	4.9%	0%	0%
D5-1	0%	0%	0%
D5-3	5.7%	9.8%	5.2%
D5-5	23.0%	11.6%	11.8%
D6-1	0%	0%	0%
D6-3	0%	5.6%	8.9%
D6-5	18.2%	14.3%	22.3%

Table A.3. Sulfur occupancy percentages at the chalcogen atom position of each ligand in crystal structures obtained after one crystallization (5 days) post-exchange with 100 eq. PhSH.

	CH5-01	CH6-03	CH6-04
D1-1	5.6%	0%	13.3%
D1-3	25.0%	29.4%	30.6%
D1-5	12.1%	0%	5.4%
D2-1	0%	0%	11.0%
D2-3	22.0%	30.3%	30.3%
D2-5	18.4%	12.4%	9.8%
D3-1	11.7%	8.9%	16.2%
D3-3	26.0%	26.9%	30.0%
D3-5	6.9%	7.5%	13.4%
D4-1	8.7%	8.6%	11.4%
D4-3	19.2%	22.2%	27.4%
D4-5	5.7%	11.3%	10.1%
D5-1	0%	0%	0%
D5-3	19.2%	20.3%	15.0%
D5-5	14.2%	20.5%	26.5%
D6-1	0%	5.3%	0%
D6-3	17.6%	21.6%	16.9%
D6-5	4.8%	14.6%	17.0%

Table A.4. Sulfur occupancy percentages at the chalcogen atom position of each ligand in crystal structures obtained after two crystallizations (10 days) post-exchange with 100 eq. PhSH.

	CH9-02	CH10-04
D1-1	12.1%	0%
D1-3	30.2%	20.2%
D1-5	0.0%	0%
D2-1	14%	5%
D2-3	32.2%	22.1%
D2-5	0.0%	0.0%
D3-1	17.6%	7.7%
D3-3	28.4%	27.9%
D3-5	0.0%	5.7%
D4-1	18.4%	10.9%
D4-3	33.3%	25.4%
D4-5	0.0%	4.0%
D5-1	0%	0%
D5-3	29.2%	34.6%
D5-5	44.9%	60.6%
D6-1	0%	0%
D6-3	31.4%	29.2%
D6-5	20.6%	44.9%

Table A.5. Sulfur occupancy percentages at the chalcogen atom position of each ligand in crystal structures obtained after three crystallizations (15 days) post-exchange with 100 eq. PhSH.

	CH11-02	CH12-01
D1-1	13.2%	7%
D1-3	31.8%	26.7%
D1-5	0%	0%
D2-1	13.2%	7.4%
D2-3	31.8%	26.7%
D2-5	0%	0.0%
D3-1	13.0%	0.0%
D3-3	28.5%	30.2%
D3-5	0%	0.0%
D4-1	13.0%	0.0%
D4-3	28.5%	30.2%
D4-5	0%	0.0%
D5-1	0%	0%
D5-3	25.6%	34.6%
D5-5	4.3%	16.3%
D6-1	0%	0.0%
D6-3	25.6%	34.6%
D6-5	4.3%	16.3%

Table A.6. Summary of data and structure refinement for crystal structures obtained after two crystallizations (10 days) post-exchange with 1 eq. PhSH.

Identification name	CH7-02	CH7-03	CH8-03
Empirical formula	$C_{129}H_{90}Au_{25}N$ $S_{1.35}Se_{16.65}$	$C_{128}H_{90}Au_{25}$ $S_{1.21}Se_{16.79}$	$C_{131}H_{90}Au_{25}N$ $S_{1.19}Se_{16.81}$
Formula weight	7935.96	7930.89	7967.81
Habit	Parallelepiped	Parallelepiped	Parallelepiped
Color	Black	Black	Black
Temperature (K)	100	100	100
Wavelength (Å)	1.000	1.000	1.000
Crystal system	Triclinic	Triclinic	Triclinic
Space group	P-1	P-1	P-1
a (Å)	16.555	16.550	16.558
b (Å)	20.257	20.272	20.277
c (Å)	23.831	23.826	23.823
α	83.18	83.16	83.13
β	80.08	80.06	80.10
γ	81.70	81.68	81.66
Volume (Å^3)	7754	7754	7759
Z	2	2	2
Independent reflections	11019	11808	10765
R(F) (I>2σ(I))	0.0493	0.0664	0.0572
wR(F2) (all data)	0.1417	0.1849	0.1598
GooF [all data]	1.033	1.037	1.051
min., max. e- dens. (e Å3)	1.255, -1.090	1.993, -1.775	1.350, -1.475

Table A.7. Summary of data and structure refinement for crystal structures obtained after three crystallizations (15 days) post-exchange with 1 eq. PhSH.

Identification name	CH13-01	CH14-02	CH14-03
Empirical formula	$C_{130}H_{90}Au_{25}N$ $S_{1.38}S_{16.62}$	$C_{120}H_{90}Au_{25}$ $S_{1.33}Se_{16.67}$	$C_{124}H_{90}Au_{25}N$ $S_{1.34}Se_{16.66}$
Formula weight	7946.94	7828.90	7862.46
Habit	Parallelepiped	Parallelepiped	Parallelepiped
Color	Black	Black	Black
Temperature (K)	100	100	100
Wavelength (Å)	1.000	1.000	1.000
Crystal system	Triclinic	Triclinic	Triclinic
Space group	P-1	P-1	P-1
a (Å)	16.548	16.552	16.574
b (Å)	20.264	20.297	20.332
c (Å)	23.797	23.828	23.845
α	83.25	83.14	83.19
β	80.14	80.05	79.85
γ	81.74	81.62	81.50
Volume ($Å^3$)	7745	7764	7787
Z	2	2	2
Independent reflections	11719	11959	11386
R(F) (I>2σ(I))	0.0602	0.0590	0.0652
wR(F2) (all data)	0.1680	0.1728	0.1841
GooF [all data]	1.060	1.077	1.053
min., max. e- dens. (e Å3)	1.653, -1.475	2.146, -2.033	1.900, -1.767

Table A.8. Summary of data and structure refinement for crystal structures obtained after one crystallization (5 days) post-exchange with 100 eq. PhSH.

Identification name	CH5-01	CH6-03	CH6-04
Empirical formula	$C_{120}H_{90}Au_{25}N$ $S_{2.20}Se_{15.80}$	$C_{124}H_{90}Au_{25}$ $S_{2.39}Se_{15.61}$	$C_{123}H_{90}Au_{25}N$ $S_{2.86}Se_{15.14}$
Formula weight	7788.38	7813.21	7793.45
Habit	Parallelepiped	Parallelepiped	Parallelepiped
Color	Black	Black	Black
Temperature (K)	100	100	100
Wavelength (Å)	1.000	1	1
Crystal system	Triclinic	Triclinic	Triclinic
Space group	P-1	P-1	P-1
a (Å)	16.587	16.612	16.597
b (Å)	20.288	20.297	20.304
c (Å)	23.765	23.736	23.758
α	83.27	83.17	83.35
β	80.28	80.2	80.26
γ	81.98	81.91	81.89
Volume (Å^3)	7769	7771	7777
Z	2	2	2
Independent reflections	11620	12139	12078
R(F) (I>2σ(I))	0.0612	0.0728	0.0635
wR(F2) (all data)	0.1897	0.2238	0.1908
GooF [all data]	1.099	1.078	1.095
min., max. e- dens. (e Å3)	1.70, -1.87	2.398, -1.942	1.920, -2.083

Table A.9. Summary of data and structure refinement for crystal structures obtained after two crystallizations (10 days) post-exchange with 100 eq. PhSH.

Identification name	CH9-02	CH10-04
Empirical formula	$C_{123}H_{90}Au_{25}NS_{3.12}Se_{14.88}$	$C_{120}H_{90}Au_{25}S_{2.79}Se_{15.21}$
Formula weight	7781.21	7828.90
Habit	Parallelepiped	Parallelepiped
Color	Black	Black
Temperature (K)	100	100
Wavelength (Å)	1.000	1.000
Crystal system	Triclinic	Triclinic
Space group	P-1	P-1
a (Å)	17.090	17.091
b (Å)	20.273	20.257
c (Å)	26.125	26.102
α	74.45	74.39
β	73.34	73.37
γ	67.65	67.63
Volume ($Å^3$)	7890	7875
Z	2	2
Independent reflections	11229	10760
R(F) (I>2σ(I))	0.0450	0.0671
wR(F2) (all data)	0.1293	0.1935
GooF [all data]	1.080	1.037
min., max. e- dens. (e Å3)	0.949, -0.828	1.620, -1.344

Table A.10. Summary of data and structure refinement for crystal structures obtained after three crystallizations (15 days) post-exchange with 100 eq. PhSH.

Identification name	CH11-02	CH12-01
Empirical formula	$C_{108}H_{90}Au_{25}NS_{2.38}Se_{15.62}$	$C_{108}H_{90}Au_{25}S_{2.36}Se_{15.64}$
Formula weight	7621.71	7622.65
Habit	Parallelepiped	Parallelepiped
Color	Black	Black
Temperature (K)	100	100
Wavelength (Å)	1.000	1.000
Crystal system	Triclinic	Triclinic
Space group	P-1	P-1
a (Å)	16.615	16.638
b (Å)	16.617	16.653
c (Å)	16.798	16.868
α	70.27	70.3
β	74.99	74.97
γ	62.56	62.52
Volume ($Å^3$)	3844	3873
Z	2	2
Independent reflections	5517	5339
R(F) (I>2σ(I))	0.0650	0.0561
wR(F2) (all data)	0.1732	0.1625
GooF [all data]	1.059	1.046
min., max. e- dens. (e Å3)	1.472, -1.331	1.379, -1.227

A.10 Crystallographic Information File for Crystal #1 100 Equivalents PhSH at 5 Days

The full CIF can be found at https://pubs.acs.org/doi/10.1021/jacs.8b10013

data_CH5-01

_audit_creation_method 'SHELXL-2014/7'
_shelx_SHELXL_version_number '2014/7'
_chemical_name_systematic ?
_chemical_name_common ?
_chemical_melting_point ?
_chemical_formula_moiety 'C108 H90 Au25 S2.20 Se15.80, C12 N'
_chemical_formula_sum

'C120 H90 Au25 N S2.20 Se15.80'
_chemical_formula_weight 7788.19

loop_
_atom_type_symbol
_atom_type_description
_atom_type_scat_dispersion_real
_atom_type_scat_dispersion_imag
_atom_type_scat_source
'Au' 'Au' -8.6060 9.5200
'International Tables Vol C Tables 4.2.6.8 and 6.1.1.4'
'Se' 'Se' -3.3840 0.5190
'International Tables Vol C Tables 4.2.6.8 and 6.1.1.4'
'C' 'C' 0.0080 0.0030
'International Tables Vol C Tables 4.2.6.8 and 6.1.1.4'
'S' 'S' 0.2070 0.2440
'International Tables Vol C Tables 4.2.6.8 and 6.1.1.4'
'H' 'H' 0.0000 0.0000
'International Tables Vol C Tables 4.2.6.8 and 6.1.1.4'
'N' 'N' 0.0140 0.0070
'International Tables Vol C Tables 4.2.6.8 and 6.1.1.4'

_space_group_crystal_system triclinic
_space_group_IT_number 2
_space_group_name_H-M_alt 'P -1'
_space_group_name_Hall '-P 1'

_shelx_space_group_comment
;
The symmetry employed for this shelxl refinement is uniquely defined
by the following loop, which should always be used as a source of
symmetry information in preference to the above space-group names.
They are only intended as comments.
;

loop_
_space_group_symop_operation_xyz
'x, y, z'
'-x, -y, -z'

_cell_length_a 16.587(3)
_cell_length_b 20.288(4)
_cell_length_c 23.765(5)
_cell_angle_alpha 83.27(3)
_cell_angle_beta 80.28(3)
_cell_angle_gamma 81.98(3)

```
_cell_volume                    7769(3)
_cell_formula_units_Z           2
_cell_measurement_temperature   100(2)
_cell_measurement_reflns_used   11620
_cell_measurement_theta_min     1.228
_cell_measurement_theta_max     28.766

_exptl_crystal_description      'Parallelogram prism'
_exptl_crystal_colour           Black
_exptl_crystal_density_meas     ?
_exptl_crystal_density_method   ?
_exptl_crystal_density_diffrn   3.329
_exptl_crystal_F_000            6729
_exptl_transmission_factor_min  ?
_exptl_transmission_factor_max  ?
_exptl_crystal_size_max         ?
_exptl_crystal_size_mid         ?
_exptl_crystal_size_min         ?
_exptl_absorpt_coefficient_mu   35.857
_shelx_estimated_absorpt_T_min  ?
_shelx_estimated_absorpt_T_max  ?
_exptl_absorpt_correction_type  ?
_exptl_absorpt_correction_T_min ?
_exptl_absorpt_correction_T_max ?
_exptl_absorpt_process_details  ?
_exptl_absorpt_special_details  ?
_diffrn_ambient_temperature     100(2)
_diffrn_radiation_wavelength    1.000
_diffrn_radiation_type          Synchrotron
_diffrn_source                  'Advanced Light Source Beamline 4.2.2'
_diffrn_measurement_device_type Synchrotron
_diffrn_measurement_method      ?
_diffrn_detector_area_resol_mean ?
_diffrn_reflns_number           22905
_diffrn_reflns_av_unetI/netI    0.1332
_diffrn_reflns_av_R_equivalents 0.0788
_diffrn_reflns_limit_h_min      -15
_diffrn_reflns_limit_h_max      15
_diffrn_reflns_limit_k_min      -18
_diffrn_reflns_limit_k_max      18
_diffrn_reflns_limit_l_min      -22
_diffrn_reflns_limit_l_max      22
_diffrn_reflns_theta_min        1.229
_diffrn_reflns_theta_max        27.858
_diffrn_reflns_theta_full       11.660
_diffrn_measured_fraction_theta_max 0.875
```

```
_diffrn_measured_fraction_theta_full  0.820
_diffrn_reflns_Laue_measured_fraction_max    0.875
_diffrn_reflns_Laue_measured_fraction_full   0.820
_diffrn_reflns_point_group_measured_fraction_max   0.875
_diffrn_reflns_point_group_measured_fraction_full  0.820
_reflns_number_total              11620
_reflns_number_gt                 8966
_reflns_threshold_expression      'I > 2\s(I)'
_reflns_Friedel_coverage          0.000
_reflns_Friedel_fraction_max      .
_reflns_Friedel_fraction_full     .

_reflns_special_details
;
 Reflections were merged by SHELXL according to the crystal
 class for the calculation of statistics and refinement.

 Structure factors included contributions from the .fab file.

 _reflns_Friedel_fraction is defined as the number of unique
 Friedel pairs measured divided by the number that would be
 possible theoretically, ignoring centric projections and
 systematic absences.
;

_computing_data_collection        ?
_computing_cell_refinement        ?
_computing_data_reduction         ?
_computing_structure_solution     ?
_computing_structure_refinement 'SHELXL-2014/7 (Sheldrick, 2014)'
_computing_molecular_graphics     ?
_computing_publication_material   ?
_refine_special_details           ?
_refine_ls_structure_factor_coef  Fsqd
_refine_ls_matrix_type            full
_refine_ls_weighting_scheme       calc
_refine_ls_weighting_details
'w=1/[\s^2^(Fo^2^)+(0.0697P)^2^+67.4455P] where P=(Fo^2^+2Fc^2^)/3'
_atom_sites_solution_primary      ?
_atom_sites_solution_secondary    ?
_atom_sites_solution_hydrogens    geom
_refine_ls_hydrogen_treatment     constr
_refine_ls_extinction_method      none
_refine_ls_extinction_coef        .
_refine_ls_number_reflns          11620
_refine_ls_number_parameters      1267
```

_refine_ls_number_restraints 972
_refine_ls_R_factor_all 0.0782
_refine_ls_R_factor_gt 0.0614
_refine_ls_wR_factor_ref 0.1890
_refine_ls_wR_factor_gt 0.1801
_refine_ls_goodness_of_fit_ref 1.090
_refine_ls_restrained_S_all 1.057
_refine_ls_shift/su_max 0.001
_refine_ls_shift/su_mean 0.000

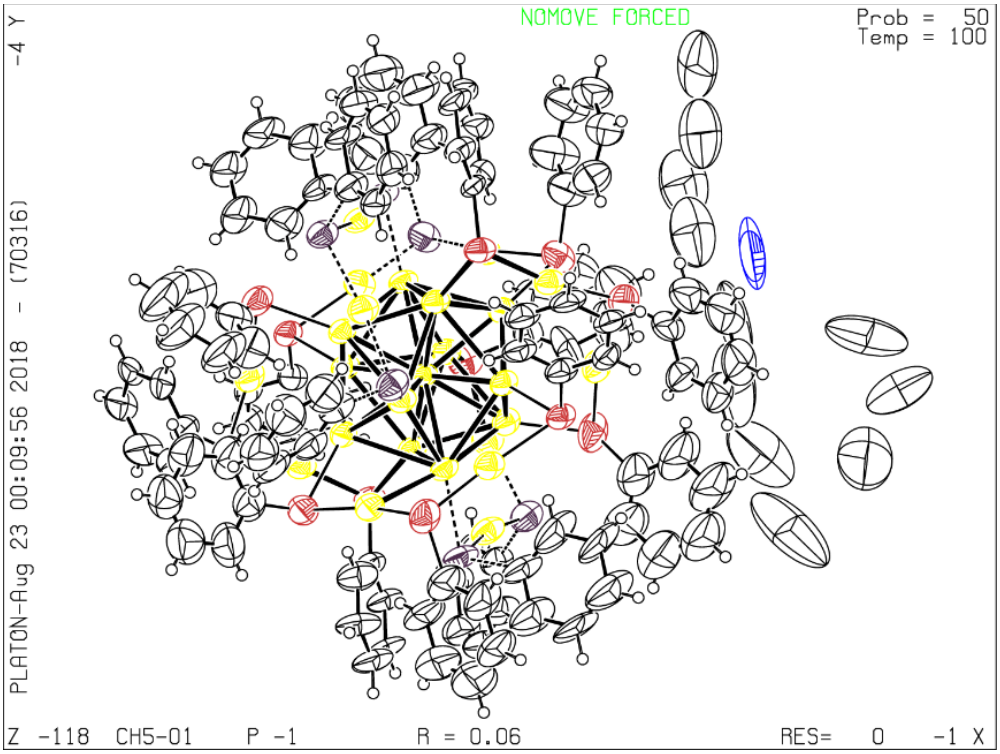


Figure A.4 ORTEP plot of crystal structure “CH5-01”.

A.11 Crystallographic Information File for Crystal #2 for 100 eq. 5 Days

The full CIF can be found at https://pubs.acs.org/doi/10.1021/jacs.8b10013

data_CH6-03

_audit_creation_method 'SHELXL-2014/7'
_shelx_SHELXL_version_number '2014/7'
_chemical_name_systematic ?
_chemical_name_common ?
_chemical_melting_point ?
_chemical_formula_moiety 'C108 H90 Au25 S2.22 Se15.78, C17 N'
_chemical_formula_sum

```
 'C125 H90 Au25 N S2.22 Se15.78'
_chemical_formula_weight          7847.30

loop_
 _atom_type_symbol
 _atom_type_description
 _atom_type_scat_dispersion_real
 _atom_type_scat_dispersion_imag
 _atom_type_scat_source
 'Au'  'Au'  -8.6060   9.5200
 'International Tables Vol C Tables 4.2.6.8 and 6.1.1.4'
 'Se'  'Se'  -3.3840   0.5190
 'International Tables Vol C Tables 4.2.6.8 and 6.1.1.4'
 'C'  'C'   0.0080   0.0030
 'International Tables Vol C Tables 4.2.6.8 and 6.1.1.4'
 'N'  'N'   0.0140   0.0070
 'International Tables Vol C Tables 4.2.6.8 and 6.1.1.4'
 'H'  'H'   0.0000   0.0000
 'International Tables Vol C Tables 4.2.6.8 and 6.1.1.4'
 'S'  'S'   0.2070   0.2440
 'International Tables Vol C Tables 4.2.6.8 and 6.1.1.4'

_space_group_crystal_system       triclinic
_space_group_IT_number           2
_space_group_name_H-M_alt        'P -1'
_space_group_name_Hall           '-P 1'

_shelx_space_group_comment
;
The symmetry employed for this shelxl refinement is uniquely defined
by the following loop, which should always be used as a source of
symmetry information in preference to the above space-group names.
They are only intended as comments.
;

loop_
 _space_group_symop_operation_xyz
 'x, y, z'
 '-x, -y, -z'

_cell_length_a                   16.612(3)
_cell_length_b                   20.297(4)
_cell_length_c                   23.736(5)
_cell_angle_alpha                  83.17(3)
_cell_angle_beta                 80.20(3)
_cell_angle_gamma                    81.91(3)
```

```
_cell_volume                    7771(3)
_cell_formula_units_Z           2
_cell_measurement_temperature   100(2)
_cell_measurement_reflns_used   12139
_cell_measurement_theta_min     1.228
_cell_measurement_theta_max     28.766

_exptl_crystal_description      'Parallelogram prism'
_exptl_crystal_colour           Black
_exptl_crystal_density_meas     ?
_exptl_crystal_density_method   ?
_exptl_crystal_density_diffrn   3.354
_exptl_crystal_F_000            6788
_exptl_transmission_factor_min  ?
_exptl_transmission_factor_max  ?
_exptl_crystal_size_max         ?
_exptl_crystal_size_mid         ?
_exptl_crystal_size_min         ?
_exptl_absorpt_coefficient_mu   35.852
_shelx_estimated_absorpt_T_min  ?
_shelx_estimated_absorpt_T_max  ?
_exptl_absorpt_correction_type  ?
_exptl_absorpt_correction_T_min ?
_exptl_absorpt_correction_T_max ?
_exptl_absorpt_process_details  ?
_exptl_absorpt_special_details  ?
_diffrn_ambient_temperature     100(2)
_diffrn_radiation_wavelength    1.000
_diffrn_radiation_type          Synchrotron
_diffrn_source                  'Advanced Light Source Beamline 4.2.2'
_diffrn_measurement_device_type Synchrotron
_diffrn_measurement_method      ?
_diffrn_detector_area_resol_mean ?
_diffrn_reflns_number           23651
_diffrn_reflns_av_unetI/netI    0.1267
_diffrn_reflns_av_R_equivalents 0.0737
_diffrn_reflns_limit_h_min      -15
_diffrn_reflns_limit_h_max      14
_diffrn_reflns_limit_k_min      -19
_diffrn_reflns_limit_k_max      19
_diffrn_reflns_limit_l_min      -22
_diffrn_reflns_limit_l_max      22
_diffrn_reflns_theta_min        1.231
_diffrn_reflns_theta_max        28.823
_diffrn_reflns_theta_full       11.660
_diffrn_measured_fraction_theta_max 0.833
```

```
_diffrn_measured_fraction_theta_full  0.760
_diffrn_reflns_Laue_measured_fraction_max    0.833
_diffrn_reflns_Laue_measured_fraction_full   0.760
_diffrn_reflns_point_group_measured_fraction_max   0.833
_diffrn_reflns_point_group_measured_fraction_full  0.760
_reflns_number_total              12139
_reflns_number_gt                 9809
_reflns_threshold_expression      'I > 2\s(I)'
_reflns_Friedel_coverage          0.000
_reflns_Friedel_fraction_max      .
_reflns_Friedel_fraction_full     .

_reflns_special_details
;
 Reflections were merged by SHELXL according to the crystal
 class for the calculation of statistics and refinement.

 Structure factors included contributions from the .fab file.

 _reflns_Friedel_fraction is defined as the number of unique
 Friedel pairs measured divided by the number that would be
 possible theoretically, ignoring centric projections and
 systematic absences.
;

_computing_data_collection        ?
_computing_cell_refinement        ?
_computing_data_reduction         ?
_computing_structure_solution     ?
_computing_structure_refinement 'SHELXL-2014/7 (Sheldrick, 2014)'
_computing_molecular_graphics     ?
_computing_publication_material   ?
_refine_special_details           ?
_refine_ls_structure_factor_coef  Fsqd
_refine_ls_matrix_type            full
_refine_ls_weighting_scheme       calc
_refine_ls_weighting_details
'w=1/[\s^2^(Fo^2^)+(0.1194P)^2^+78.7207P] where P=(Fo^2^+2Fc^2^)/3'
_atom_sites_solution_primary      ?
_atom_sites_solution_secondary    ?
_atom_sites_solution_hydrogens    geom
_refine_ls_hydrogen_treatment     constr
_refine_ls_extinction_method      none
_refine_ls_extinction_coef        .
_refine_ls_number_reflns          12139
_refine_ls_number_parameters      1302
```

_refine_ls_number_restraints 2673
_refine_ls_R_factor_all 0.0836
_refine_ls_R_factor_gt 0.0728
_refine_ls_wR_factor_ref 0.2238
_refine_ls_wR_factor_gt 0.2153
_refine_ls_goodness_of_fit_ref 1.078
_refine_ls_restrained_S_all 0.982
_refine_ls_shift/su_max 2.491
_refine_ls_shift/su_mean 0.003

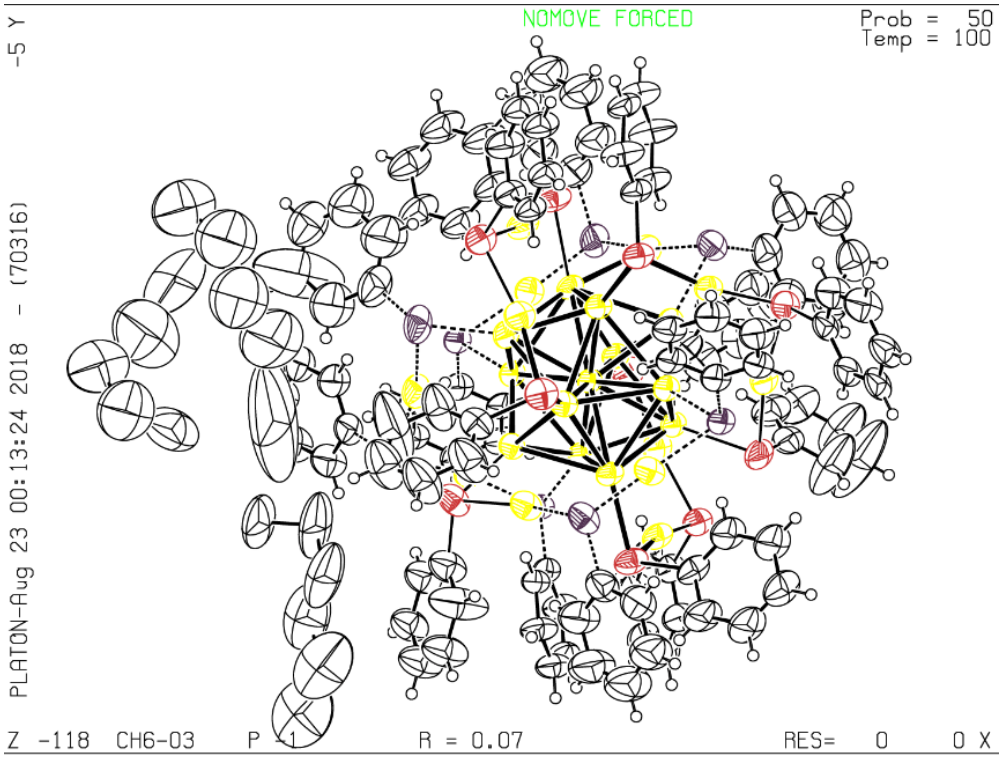


Figure A.5 ORTEP plot of crystal structure “CH6-03”.

A.12 Crystallographic Information File for Crystal #3 100 eq. 5 Days

The full CIF can be found at https://pubs.acs.org/doi/10.1021/jacs.8b10013

data_CH6-04

_audit_creation_method 'SHELXL-2014/7'
_shelx_SHELXL_version_number '2014/7'
_chemical_name_systematic ?
_chemical_name_common ?
_chemical_melting_point ?
_chemical_formula_moiety 'C108 H90 Au25 S2.97 Se15.03, C15 N'
_chemical_formula_sum

```
 'C123 H90 Au25 N S2.97 Se15.03'
_chemical_formula_weight          7788.10

loop_
 _atom_type_symbol
 _atom_type_description
 _atom_type_scat_dispersion_real
 _atom_type_scat_dispersion_imag
 _atom_type_scat_source
 'Au'  'Au'  -8.6060   9.5200
 'International Tables Vol C Tables 4.2.6.8 and 6.1.1.4'
 'Se'  'Se'  -3.3840   0.5190
 'International Tables Vol C Tables 4.2.6.8 and 6.1.1.4'
 'C'  'C'   0.0080   0.0030
 'International Tables Vol C Tables 4.2.6.8 and 6.1.1.4'
 'H'  'H'   0.0000   0.0000
 'International Tables Vol C Tables 4.2.6.8 and 6.1.1.4'
 'S'  'S'   0.2070   0.2440
 'International Tables Vol C Tables 4.2.6.8 and 6.1.1.4'
 'N'  'N'   0.0140   0.0070
 'International Tables Vol C Tables 4.2.6.8 and 6.1.1.4'

_space_group_crystal_system       triclinic
_space_group_IT_number           2
_space_group_name_H-M_alt        'P -1'
_space_group_name_Hall           '-P 1'

_shelx_space_group_comment
;
The symmetry employed for this shelxl refinement is uniquely defined
by the following loop, which should always be used as a source of
symmetry information in preference to the above space-group names.
They are only intended as comments.
;

loop_
 _space_group_symop_operation_xyz
 'x, y, z'
 '-x, -y, -z'

_cell_length_a                   16.597(3)
_cell_length_b                   20.304(4)
_cell_length_c                   23.758(5)
_cell_angle_alpha                  83.35(3)
_cell_angle_beta                 80.26(3)
_cell_angle_gamma                    81.89(3)
```

```
_cell_volume                    7777(3)
_cell_formula_units_Z           2
_cell_measurement_temperature   100(2)
_cell_measurement_reflns_used   12078
_cell_measurement_theta_min     1.228
_cell_measurement_theta_max     28.766

_exptl_crystal_description      'Parallelogram prism'
_exptl_crystal_colour           Black
_exptl_crystal_density_meas     ?
_exptl_crystal_density_method   ?
_exptl_crystal_density_diffrn   3.326
_exptl_crystal_F_000            6737
_exptl_transmission_factor_min  ?
_exptl_transmission_factor_max  ?
_exptl_crystal_size_max         ?
_exptl_crystal_size_mid         ?
_exptl_crystal_size_min         ?
_exptl_absorpt_coefficient_mu   35.793
_shelx_estimated_absorpt_T_min  ?
_shelx_estimated_absorpt_T_max  ?
_exptl_absorpt_correction_type  ?
_exptl_absorpt_correction_T_min ?
_exptl_absorpt_correction_T_max ?
_exptl_absorpt_process_details  ?
_exptl_absorpt_special_details  ?
_diffrn_ambient_temperature     100(2)
_diffrn_radiation_wavelength    1.000
_diffrn_radiation_type          Synchrotron
_diffrn_source                  'Advanced Light Source Beamline 4.2.2'
_diffrn_measurement_device_type Synchrotron
_diffrn_measurement_method      ?
_diffrn_detector_area_resol_mean ?
_diffrn_reflns_number           23553
_diffrn_reflns_av_unetI/netI    0.1273
_diffrn_reflns_av_R_equivalents 0.0656
_diffrn_reflns_limit_h_min      -15
_diffrn_reflns_limit_h_max      13
_diffrn_reflns_limit_k_min      -19
_diffrn_reflns_limit_k_max      19
_diffrn_reflns_limit_l_min      -22
_diffrn_reflns_limit_l_max      22
_diffrn_reflns_theta_min        1.229
_diffrn_reflns_theta_max        28.721
_diffrn_reflns_theta_full       11.660
_diffrn_measured_fraction_theta_max 0.836
```

```
_diffrn_measured_fraction_theta_full  0.731
_diffrn_reflns_Laue_measured_fraction_max    0.836
_diffrn_reflns_Laue_measured_fraction_full   0.731
_diffrn_reflns_point_group_measured_fraction_max   0.836
_diffrn_reflns_point_group_measured_fraction_full  0.731
_reflns_number_total              12078
_reflns_number_gt                 10094
_reflns_threshold_expression      'I > 2\s(I)'
_reflns_Friedel_coverage          0.000
_reflns_Friedel_fraction_max      .
_reflns_Friedel_fraction_full     .

_reflns_special_details
;
 Reflections were merged by SHELXL according to the crystal
 class for the calculation of statistics and refinement.

 Structure factors included contributions from the .fab file.

 _reflns_Friedel_fraction is defined as the number of unique
 Friedel pairs measured divided by the number that would be
 possible theoretically, ignoring centric projections and
 systematic absences.
;

_computing_data_collection        ?
_computing_cell_refinement        ?
_computing_data_reduction         ?
_computing_structure_solution     ?
_computing_structure_refinement 'SHELXL-2014/7 (Sheldrick, 2014)'
_computing_molecular_graphics     ?
_computing_publication_material   ?
_refine_special_details           ?
_refine_ls_structure_factor_coef  Fsqd
_refine_ls_matrix_type            full
_refine_ls_weighting_scheme       calc
_refine_ls_weighting_details
'w=1/[\s^2^(Fo^2^)+(0.0578P)^2^+85.4881P] where P=(Fo^2^+2Fc^2^)/3'
_atom_sites_solution_primary      ?
_atom_sites_solution_secondary    ?
_atom_sites_solution_hydrogens    geom
_refine_ls_hydrogen_treatment     constr
_refine_ls_extinction_method      none
_refine_ls_extinction_coef        .
_refine_ls_number_reflns          12078
_refine_ls_number_parameters      1305
```

_refine_ls_number_restraints 803
_refine_ls_R_factor_all 0.0714
_refine_ls_R_factor_gt 0.0635
_refine_ls_wR_factor_ref 0.1908
_refine_ls_wR_factor_gt 0.1820
_refine_ls_goodness_of_fit_ref 1.095
_refine_ls_restrained_S_all 1.070
_refine_ls_shift/su_max 0.001
_refine_ls_shift/su_mean 0.000

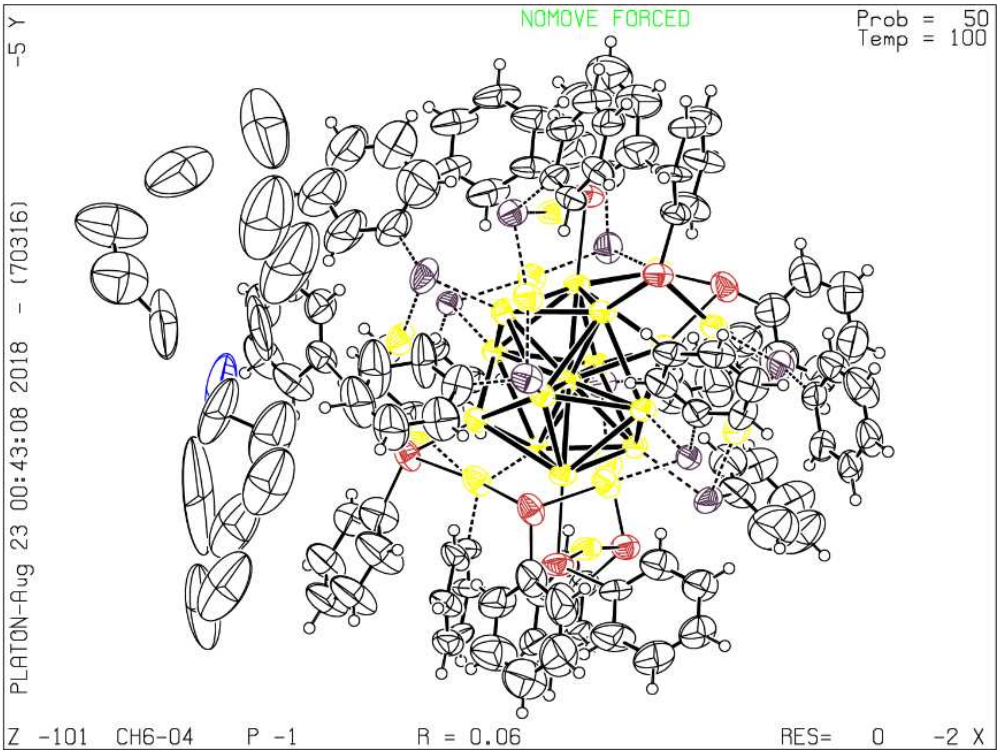


Figure A.6 ORTEP plot of crystal structure “CH6-04”.

A.13 Crystallographic Information File for Crystal #1 100 eq. 10 Days

The full CIF can be found at https://pubs.acs.org/doi/10.1021/jacs.8b10013

data_CH9-02

_audit_creation_method 'SHELXL-2014/7'
_shelx_SHELXL_version_number '2014/7'
_chemical_name_systematic ?
_chemical_name_common ?
_chemical_melting_point ?
_chemical_formula_moiety 'C108 H90 Au25 S3.12 Se14.88, C15 N'
_chemical_formula_sum

```
 'C123 H90 Au25 N S3.12 Se14.88'
_chemical_formula_weight          7781.07

loop_
 _atom_type_symbol
 _atom_type_description
 _atom_type_scat_dispersion_real
 _atom_type_scat_dispersion_imag
 _atom_type_scat_source
 'Au'  'Au'  -8.6060   9.5200
 'International Tables Vol C Tables 4.2.6.8 and 6.1.1.4'
 'Se'  'Se'  -3.3840   0.5190
 'International Tables Vol C Tables 4.2.6.8 and 6.1.1.4'
 'C'  'C'   0.0080   0.0030
 'International Tables Vol C Tables 4.2.6.8 and 6.1.1.4'
 'H'  'H'   0.0000   0.0000
 'International Tables Vol C Tables 4.2.6.8 and 6.1.1.4'
 'S'  'S'   0.2070   0.2440
 'International Tables Vol C Tables 4.2.6.8 and 6.1.1.4'
 'N'  'N'   0.0140   0.0070
 'International Tables Vol C Tables 4.2.6.8 and 6.1.1.4'

_space_group_crystal_system       triclinic
_space_group_IT_number           2
_space_group_name_H-M_alt        'P -1'
_space_group_name_Hall           '-P 1'

_shelx_space_group_comment
;
The symmetry employed for this shelxl refinement is uniquely defined
by the following loop, which should always be used as a source of
symmetry information in preference to the above space-group names.
They are only intended as comments.
;

loop_
 _space_group_symop_operation_xyz
 'x, y, z'
 '-x, -y, -z'

_cell_length_a                 17.090(3)
_cell_length_b                 20.273(4)
_cell_length_c                 26.125(5)
_cell_angle_alpha                74.45(3)
_cell_angle_beta                 73.34(3)
_cell_angle_gamma                  67.65(3)
```

```
_cell_volume                    7890(4)
_cell_formula_units_Z           2
_cell_measurement_temperature   100(2)
_cell_measurement_reflns_used   11229
_cell_measurement_theta_min     1.228
_cell_measurement_theta_max     28.766

_exptl_crystal_description      'Parallelogram prism'
_exptl_crystal_colour           Black
_exptl_crystal_density_meas     ?
_exptl_crystal_density_method   ?
_exptl_crystal_density_diffrn   3.275
_exptl_crystal_F_000            6732
_exptl_transmission_factor_min  ?
_exptl_transmission_factor_max  ?
_exptl_crystal_size_max         ?
_exptl_crystal_size_mid         ?
_exptl_crystal_size_min         ?
_exptl_absorpt_coefficient_mu   35.275
_shelx_estimated_absorpt_T_min  ?
_shelx_estimated_absorpt_T_max  ?
_exptl_absorpt_correction_type  ?
_exptl_absorpt_correction_T_min ?
_exptl_absorpt_correction_T_max ?
_exptl_absorpt_process_details  ?
_exptl_absorpt_special_details  ?
_diffrn_ambient_temperature     100(2)
_diffrn_radiation_wavelength    1.000
_diffrn_radiation_type          Synchrotron
_diffrn_source                  'Advanced Light Source Beamline 4.2.2'
_diffrn_measurement_device_type 'RDI_CMOS 8M'
_diffrn_measurement_method      ?
_diffrn_detector_area_resol_mean ?
_diffrn_reflns_number           21699
_diffrn_reflns_av_unetI/netI    0.0782
_diffrn_reflns_av_R_equivalents 0.0362
_diffrn_reflns_limit_h_min      -16
_diffrn_reflns_limit_h_max      16
_diffrn_reflns_limit_k_min      -19
_diffrn_reflns_limit_k_max      18
_diffrn_reflns_limit_l_min      -24
_diffrn_reflns_limit_l_max      24
_diffrn_reflns_theta_min        1.164
_diffrn_reflns_theta_max        28.810
_diffrn_reflns_theta_full       11.660
_diffrn_measured_fraction_theta_max 0.758
```

```
_diffrn_measured_fraction_theta_full  0.623
_diffrn_reflns_Laue_measured_fraction_max    0.758
_diffrn_reflns_Laue_measured_fraction_full   0.623
_diffrn_reflns_point_group_measured_fraction_max   0.758
_diffrn_reflns_point_group_measured_fraction_full  0.623
_reflns_number_total              11229
_reflns_number_gt                 9953
_reflns_threshold_expression      'I > 2\s(I)'
_reflns_Friedel_coverage          0.000
_reflns_Friedel_fraction_max      .
_reflns_Friedel_fraction_full     .

_reflns_special_details
;
 Reflections were merged by SHELXL according to the crystal
 class for the calculation of statistics and refinement.

 Structure factors included contributions from the .fab file.

 _reflns_Friedel_fraction is defined as the number of unique
 Friedel pairs measured divided by the number that would be
 possible theoretically, ignoring centric projections and
 systematic absences.
;

_computing_data_collection        ?
_computing_cell_refinement        ?
_computing_data_reduction         ?
_computing_structure_solution     ?
_computing_structure_refinement 'SHELXL-2014/7 (Sheldrick, 2014)'
_computing_molecular_graphics     ?
_computing_publication_material   ?
_refine_special_details           ?
_refine_ls_structure_factor_coef  Fsqd
_refine_ls_matrix_type            full
_refine_ls_weighting_scheme       calc
_refine_ls_weighting_details
'w=1/[\s^2^(Fo^2^)+(0.0001P)^2^+80.7426P] where P=(Fo^2^+2Fc^2^)/3'
_atom_sites_solution_primary      ?
_atom_sites_solution_secondary    ?
_atom_sites_solution_hydrogens    geom
_refine_ls_hydrogen_treatment     constr
_refine_ls_extinction_method      none
_refine_ls_extinction_coef        .
_refine_ls_number_reflns          11229
_refine_ls_number_parameters      1330
```

_refine_ls_number_restraints 2892
_refine_ls_R_factor_all 0.0500
_refine_ls_R_factor_gt 0.0450
_refine_ls_wR_factor_ref 0.1293
_refine_ls_wR_factor_gt 0.1214
_refine_ls_goodness_of_fit_ref 1.080
_refine_ls_restrained_S_all 0.989
_refine_ls_shift/su_max 0.001
_refine_ls_shift/su_mean 0.000

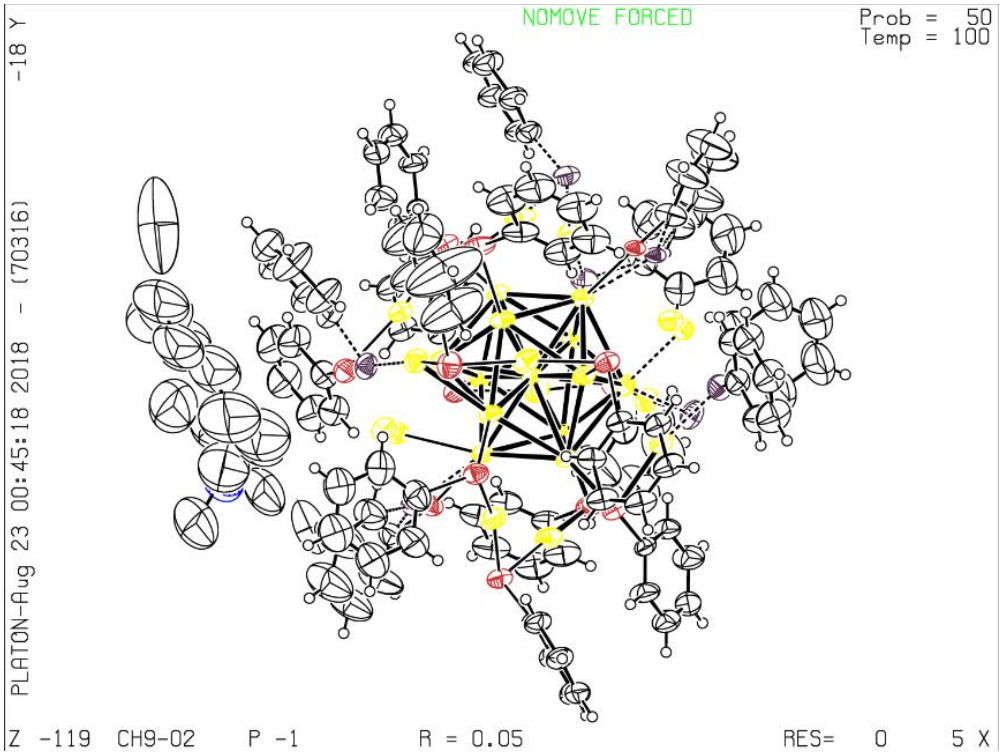


Figure A.7 ORTEP plot of crystal structure “CH9-02”.

A.14 Crystallographic Information File for Crystal #2 100 eq. 10 Days

The full CIF can be found at https://pubs.acs.org/doi/10.1021/jacs.8b10013

data_CH10-04

_audit_creation_method 'SHELXL-2014/7'
_shelx_SHELXL_version_number '2014/7'
_chemical_name_systematic ?
_chemical_name_common ?
_chemical_melting_point ?
_chemical_formula_moiety 'C108 H90 Au25 N S2.79 Se15.21, C12'
_chemical_formula_sum

```
 'C120 H90 Au25 N S2.79 Se15.21'
_chemical_formula_weight          7760.52

loop_
 _atom_type_symbol
 _atom_type_description
 _atom_type_scat_dispersion_real
 _atom_type_scat_dispersion_imag
 _atom_type_scat_source
 'Au'  'Au'  -8.6060   9.5200
 'International Tables Vol C Tables 4.2.6.8 and 6.1.1.4'
 'Se'  'Se'  -3.3840   0.5190
 'International Tables Vol C Tables 4.2.6.8 and 6.1.1.4'
 'C'  'C'   0.0080   0.0030
 'International Tables Vol C Tables 4.2.6.8 and 6.1.1.4'
 'H'  'H'   0.0000   0.0000
 'International Tables Vol C Tables 4.2.6.8 and 6.1.1.4'
 'S'  'S'   0.2070   0.2440
 'International Tables Vol C Tables 4.2.6.8 and 6.1.1.4'
 'N'  'N'   0.0140   0.0070
 'International Tables Vol C Tables 4.2.6.8 and 6.1.1.4'

_space_group_crystal_system       triclinic
_space_group_IT_number           2
_space_group_name_H-M_alt        'P -1'
_space_group_name_Hall           '-P 1'

_shelx_space_group_comment
;
The symmetry employed for this shelxl refinement is uniquely defined
by the following loop, which should always be used as a source of
symmetry information in preference to the above space-group names.
They are only intended as comments.
;

loop_
 _space_group_symop_operation_xyz
 'x, y, z'
 '-x, -y, -z'

_cell_length_a                 17.091(3)
_cell_length_b                 20.257(4)
_cell_length_c                 26.102(5)
_cell_angle_alpha                74.39(3)
_cell_angle_beta                 73.37(3)
_cell_angle_gamma                  67.63(3)
```

```
_cell_volume                    7876(4)
_cell_formula_units_Z           2
_cell_measurement_temperature   100(2)
_cell_measurement_reflns_used   10760
_cell_measurement_theta_min     1.228
_cell_measurement_theta_max     28.766

_exptl_crystal_description      'Parallelogram prism'
_exptl_crystal_colour           Black
_exptl_crystal_density_meas     ?
_exptl_crystal_density_method   ?
_exptl_crystal_density_diffrn   3.273
_exptl_crystal_F_000            6708
_exptl_transmission_factor_min  ?
_exptl_transmission_factor_max  ?
_exptl_crystal_size_max         ?
_exptl_crystal_size_mid         ?
_exptl_crystal_size_min         ?
_exptl_absorpt_coefficient_mu   35.350
_shelx_estimated_absorpt_T_min  ?
_shelx_estimated_absorpt_T_max  ?
_exptl_absorpt_correction_type  ?
_exptl_absorpt_correction_T_min ?
_exptl_absorpt_correction_T_max ?
_exptl_absorpt_process_details  ?
_exptl_absorpt_special_details  ?
_diffrn_ambient_temperature     100(2)
_diffrn_radiation_wavelength    1.000
_diffrn_radiation_type          Synchrotron
_diffrn_source                  'Advanced Light Source Beamline 4.2.2'
_diffrn_measurement_device_type Synchrotron
_diffrn_measurement_method      ?
_diffrn_detector_area_resol_mean ?
_diffrn_reflns_number           20159
_diffrn_reflns_av_unetI/netI    0.1034
_diffrn_reflns_av_R_equivalents 0.0536
_diffrn_reflns_limit_h_min      -15
_diffrn_reflns_limit_h_max      15
_diffrn_reflns_limit_k_min      -17
_diffrn_reflns_limit_k_max      19
_diffrn_reflns_limit_l_min      -24
_diffrn_reflns_limit_l_max      24
_diffrn_reflns_theta_min        1.165
_diffrn_reflns_theta_max        28.795
_diffrn_reflns_theta_full       11.660
_diffrn_measured_fraction_theta_max 0.729
```

```
_diffrn_measured_fraction_theta_full  0.589
_diffrn_reflns_Laue_measured_fraction_max    0.729
_diffrn_reflns_Laue_measured_fraction_full   0.589
_diffrn_reflns_point_group_measured_fraction_max   0.729
_diffrn_reflns_point_group_measured_fraction_full  0.589
_reflns_number_total              10760
_reflns_number_gt                 9661
_reflns_threshold_expression      'I > 2\s(I)'
_reflns_Friedel_coverage          0.000
_reflns_Friedel_fraction_max      .
_reflns_Friedel_fraction_full     .

_reflns_special_details
;
 Reflections were merged by SHELXL according to the crystal
 class for the calculation of statistics and refinement.

 Structure factors included contributions from the .fab file.

 _reflns_Friedel_fraction is defined as the number of unique
 Friedel pairs measured divided by the number that would be
 possible theoretically, ignoring centric projections and
 systematic absences.
;

_computing_data_collection        ?
_computing_cell_refinement        ?
_computing_data_reduction         ?
_computing_structure_solution     ?
_computing_structure_refinement 'SHELXL-2014/7 (Sheldrick, 2014)'
_computing_molecular_graphics     ?
_computing_publication_material   ?
_refine_special_details           ?
_refine_ls_structure_factor_coef  Fsqd
_refine_ls_matrix_type            full
_refine_ls_weighting_scheme       calc
_refine_ls_weighting_details
'w=1/[\s^2^(Fo^2^)+(0.0991P)^2^+105.0066P] where P=(Fo^2^+2Fc^2^)/3'
_atom_sites_solution_primary      ?
_atom_sites_solution_secondary    ?
_atom_sites_solution_hydrogens    geom
_refine_ls_hydrogen_treatment     constr
_refine_ls_extinction_method      none
_refine_ls_extinction_coef        .
_refine_ls_number_reflns          10760
_refine_ls_number_parameters      1293
```

_refine_ls_number_restraints 2685
_refine_ls_R_factor_all 0.0716
_refine_ls_R_factor_gt 0.0671
_refine_ls_wR_factor_ref 0.1935
_refine_ls_wR_factor_gt 0.1886
_refine_ls_goodness_of_fit_ref 1.037
_refine_ls_restrained_S_all 0.935
_refine_ls_shift/su_max 0.001
_refine_ls_shift/su_mean 0.000

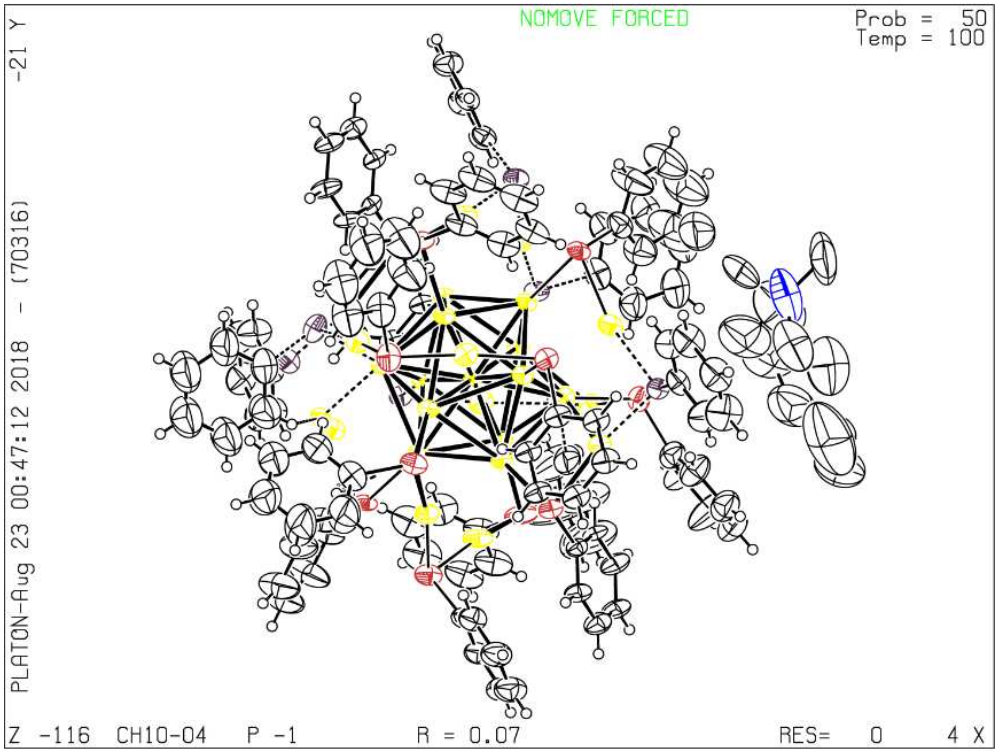


Figure A.8 ORTEP plot of crystal structure “CH10-04”.

A.15 Crystallographic Information File for Crystal #1 100 eq. 15 Days

The full CIF can be found at https://pubs.acs.org/doi/10.1021/jacs.8b10013

data_CH11-02

_audit_creation_method 'SHELXL-2014/7'
_shelx_SHELXL_version_number '2014/7'
_chemical_name_systematic ?
_chemical_name_common ?
_chemical_melting_point ?
_chemical_formula_moiety 'C108 H90 Au25 S2.38 Se15.62'
_chemical_formula_sum

```
 'C108 H90 Au25 S2.38 Se15.62'
_chemical_formula_weight          7621.62

loop_
 _atom_type_symbol
 _atom_type_description
 _atom_type_scat_dispersion_real
 _atom_type_scat_dispersion_imag
 _atom_type_scat_source
 'Au'  'Au'  -8.6060   9.5200
 'International Tables Vol C Tables 4.2.6.8 and 6.1.1.4'
 'Se'  'Se'  -3.3840   0.5190
 'International Tables Vol C Tables 4.2.6.8 and 6.1.1.4'
 'C'  'C'   0.0080   0.0030
 'International Tables Vol C Tables 4.2.6.8 and 6.1.1.4'
 'S'  'S'   0.2070   0.2440
 'International Tables Vol C Tables 4.2.6.8 and 6.1.1.4'
 'H'  'H'   0.0000   0.0000
 'International Tables Vol C Tables 4.2.6.8 and 6.1.1.4'

_space_group_crystal_system       triclinic
_space_group_IT_number            2
_space_group_name_H-M_alt         'P -1'
_space_group_name_Hall            '-P 1'

_shelx_space_group_comment
;
The symmetry employed for this shelxl refinement is uniquely defined
by the following loop, which should always be used as a source of
symmetry information in preference to the above space-group names.
They are only intended as comments.
;

loop_
 _space_group_symop_operation_xyz
 'x, y, z'
 '-x, -y, -z'

_cell_length_a                    16.615(3)
_cell_length_b                    16.617(3)
_cell_length_c                    16.798(3)
_cell_angle_alpha                   70.27(3)
_cell_angle_beta                  74.99(3)
_cell_angle_gamma                     62.56(3)
_cell_volume                      3844.6(18)
_cell_formula_units_Z             1
```

```
_cell_measurement_temperature     100(2)
_cell_measurement_reflns_used     5517
_cell_measurement_theta_min       1.228
_cell_measurement_theta_max       28.766

_exptl_crystal_description        'Parallelogram prism'
_exptl_crystal_colour             Black
_exptl_crystal_density_meas       ?
_exptl_crystal_density_method     ?
_exptl_crystal_density_diffrn     3.292
_exptl_crystal_F_000              3282
_exptl_transmission_factor_min    ?
_exptl_transmission_factor_max    ?
_exptl_crystal_size_max           ?
_exptl_crystal_size_mid           ?
_exptl_crystal_size_min           ?
_exptl_absorpt_coefficient_mu     36.217
_shelx_estimated_absorpt_T_min    ?
_shelx_estimated_absorpt_T_max    ?
_exptl_absorpt_correction_type    ?
_exptl_absorpt_correction_T_min   ?
_exptl_absorpt_correction_T_max   ?
_exptl_absorpt_process_details    ?
_exptl_absorpt_special_details    ?
_diffrn_ambient_temperature       100(2)
_diffrn_radiation_wavelength      1.000
_diffrn_radiation_type            Synchrotron
_diffrn_source                    'Advanced Light Source Beamline 4.2.2'
_diffrn_measurement_device_type   Synchrotron
_diffrn_measurement_method        ?
_diffrn_detector_area_resol_mean  ?
_diffrn_reflns_number             10422
_diffrn_reflns_av_unetI/netI      0.1068
_diffrn_reflns_av_R_equivalents   0.0687
_diffrn_reflns_limit_h_min        -15
_diffrn_reflns_limit_h_max        15
_diffrn_reflns_limit_k_min        -15
_diffrn_reflns_limit_k_max        15
_diffrn_reflns_limit_l_min        -16
_diffrn_reflns_limit_l_max        14
_diffrn_reflns_theta_min          3.654
_diffrn_reflns_theta_max          28.878
_diffrn_reflns_theta_full         11.660
_diffrn_measured_fraction_theta_max   0.760
_diffrn_measured_fraction_theta_full  0.402
_diffrn_reflns_Laue_measured_fraction_max    0.760
```

```
_diffrn_reflns_Laue_measured_fraction_full   0.402
_diffrn_reflns_point_group_measured_fraction_max   0.760
_diffrn_reflns_point_group_measured_fraction_full  0.402
_reflns_number_total              5517
_reflns_number_gt                 5186
_reflns_threshold_expression      'I > 2\s(I)'
_reflns_Friedel_coverage          0.000
_reflns_Friedel_fraction_max      .
_reflns_Friedel_fraction_full     .

_reflns_special_details
;
 Reflections were merged by SHELXL according to the crystal
 class for the calculation of statistics and refinement.

 Structure factors included contributions from the .fab file.

 _reflns_Friedel_fraction is defined as the number of unique
 Friedel pairs measured divided by the number that would be
 possible theoretically, ignoring centric projections and
 systematic absences.
;

_computing_data_collection        ?
_computing_cell_refinement        ?
_computing_data_reduction         ?
_computing_structure_solution     ?
_computing_structure_refinement 'SHELXL-2014/7 (Sheldrick, 2014)'
_computing_molecular_graphics     ?
_computing_publication_material   ?
_refine_special_details           ?
_refine_ls_structure_factor_coef  Fsqd
_refine_ls_matrix_type            full
_refine_ls_weighting_scheme       calc
_refine_ls_weighting_details
'w=1/[\s^2^(Fo^2^)+(0.0406P)^2^+115.9552P] where P=(Fo^2^+2Fc^2^)/3'
_atom_sites_solution_primary      ?
_atom_sites_solution_secondary    ?
_atom_sites_solution_hydrogens    geom
_refine_ls_hydrogen_treatment     constr
_refine_ls_extinction_method      none
_refine_ls_extinction_coef        .
_refine_ls_number_reflns          5517
_refine_ls_number_parameters      563
_refine_ls_number_restraints      324
_refine_ls_R_factor_all           0.0682
```

_refine_ls_R_factor_gt 0.0650
_refine_ls_wR_factor_ref 0.1732
_refine_ls_wR_factor_gt 0.1707
_refine_ls_goodness_of_fit_ref 1.059
_refine_ls_restrained_S_all 1.036
_refine_ls_shift/su_max 0.000
_refine_ls_shift/su_mean 0.000

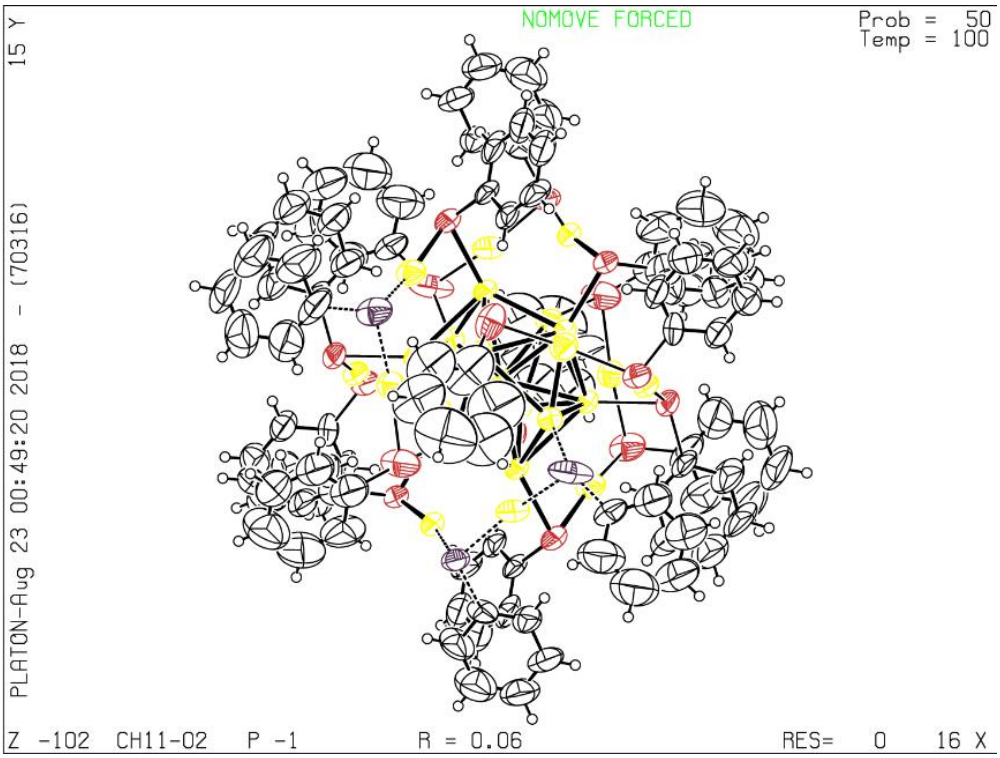


Figure A.9 ORTEP plot of crystal structure “CH11-02”.

A.16 Crystallographic Information Files for Crystal #2 100 eq. 15 Days

The full CIF can be found at https://pubs.acs.org/doi/10.1021/jacs.8b10013

data_CH12-01

_audit_creation_method 'SHELXL-2014/7'
_shelx_SHELXL_version_number '2014/7'
_chemical_name_systematic ?
_chemical_name_common ?
_chemical_melting_point ?
_chemical_formula_moiety 'C108 H90 Au25 S2.36 Se15.64'
_chemical_formula_sum
'C108 H90 Au25 S2.36 Se15.64'
_chemical_formula_weight 7622.55

```
loop_
 _atom_type_symbol
 _atom_type_description
 _atom_type_scat_dispersion_real
 _atom_type_scat_dispersion_imag
 _atom_type_scat_source
 'Au'  'Au'  -8.6060   9.5200
 'International Tables Vol C Tables 4.2.6.8 and 6.1.1.4'
 'Se'  'Se'  -3.3840   0.5190
 'International Tables Vol C Tables 4.2.6.8 and 6.1.1.4'
 'C'  'C'   0.0080   0.0030
 'International Tables Vol C Tables 4.2.6.8 and 6.1.1.4'
 'S'  'S'   0.2070   0.2440
 'International Tables Vol C Tables 4.2.6.8 and 6.1.1.4'
 'H'  'H'   0.0000   0.0000
 'International Tables Vol C Tables 4.2.6.8 and 6.1.1.4'

_space_group_crystal_system      triclinic
_space_group_IT_number           2
_space_group_name_H-M_alt        'P -1'
_space_group_name_Hall           '-P 1'

_shelx_space_group_comment
;
The symmetry employed for this shelxl refinement is uniquely defined
by the following loop, which should always be used as a source of
symmetry information in preference to the above space-group names.
They are only intended as comments.
;

loop_
 _space_group_symop_operation_xyz
 'x, y, z'
 '-x, -y, -z'

_cell_length_a                   16.638(3)
_cell_length_b                   16.653(3)
_cell_length_c                   16.868(3)
_cell_angle_alpha                  70.30(3)
_cell_angle_beta                 74.97(3)
_cell_angle_gamma                  62.52(3)
_cell_volume                     3873.5(18)
_cell_formula_units_Z            1
_cell_measurement_temperature    100(2)
_cell_measurement_reflns_used    5339
```

_cell_measurement_theta_min 1.228
_cell_measurement_theta_max 27.858

_exptl_crystal_description 'Parallelogram prism'
_exptl_crystal_colour Black
_exptl_crystal_density_meas ?
_exptl_crystal_density_method ?
_exptl_crystal_density_diffrn 3.268
_exptl_crystal_F_000 3283
_exptl_transmission_factor_min ?
_exptl_transmission_factor_max ?
_exptl_crystal_size_max ?
_exptl_crystal_size_mid ?
_exptl_crystal_size_min ?
_exptl_absorpt_coefficient_mu 35.947
_shelx_estimated_absorpt_T_min ?
_shelx_estimated_absorpt_T_max ?
_exptl_absorpt_correction_type ?
_exptl_absorpt_correction_T_min ?
_exptl_absorpt_correction_T_max ?
_exptl_absorpt_process_details ?
_exptl_absorpt_special_details ?
_diffrn_ambient_temperature 100(2)
_diffrn_radiation_wavelength 1.000
_diffrn_radiation_type Synchrotron
_diffrn_source 'Advanced Light Source Beamline 4.2.2'
_diffrn_measurement_device_type Synchrotron
_diffrn_measurement_method ?
_diffrn_detector_area_resol_mean ?
_diffrn_reflns_number 10125
_diffrn_reflns_av_unetI/netI 0.1300
_diffrn_reflns_av_R_equivalents 0.0625
_diffrn_reflns_limit_h_min -15
_diffrn_reflns_limit_h_max 15
_diffrn_reflns_limit_k_min -15
_diffrn_reflns_limit_k_max 15
_diffrn_reflns_limit_l_min -15
_diffrn_reflns_limit_l_max 15
_diffrn_reflns_theta_min 3.638
_diffrn_reflns_theta_max 28.801
_diffrn_reflns_theta_full 11.660
_diffrn_measured_fraction_theta_max 0.736
_diffrn_measured_fraction_theta_full 0.384
_diffrn_reflns_Laue_measured_fraction_max 0.736
_diffrn_reflns_Laue_measured_fraction_full 0.384
_diffrn_reflns_point_group_measured_fraction_max 0.736

```
_diffrn_reflns_point_group_measured_fraction_full  0.384
_reflns_number_total              5339
_reflns_number_gt                 4908
_reflns_threshold_expression      'I > 2\s(I)'
_reflns_Friedel_coverage          0.000
_reflns_Friedel_fraction_max      .
_reflns_Friedel_fraction_full     .

_reflns_special_details
;
 Reflections were merged by SHELXL according to the crystal
 class for the calculation of statistics and refinement.

 Structure factors included contributions from the .fab file.

 _reflns_Friedel_fraction is defined as the number of unique
 Friedel pairs measured divided by the number that would be
 possible theoretically, ignoring centric projections and
 systematic absences.
;

_computing_data_collection        ?
_computing_cell_refinement        ?
_computing_data_reduction         ?
_computing_structure_solution     ?
_computing_structure_refinement 'SHELXL-2014/7 (Sheldrick, 2014)'
_computing_molecular_graphics     ?
_computing_publication_material   ?
_refine_special_details           ?
_refine_ls_structure_factor_coef  Fsqd
_refine_ls_matrix_type            full
_refine_ls_weighting_scheme       calc
_refine_ls_weighting_details
'w=1/[\s^2^(Fo^2^)+57.6182P] where P=(Fo^2^+2Fc^2^)/3'
_atom_sites_solution_primary      ?
_atom_sites_solution_secondary    ?
_atom_sites_solution_hydrogens    geom
_refine_ls_hydrogen_treatment     constr
_refine_ls_extinction_method      none
_refine_ls_extinction_coef        .
_refine_ls_number_reflns          5339
_refine_ls_number_parameters      579
_refine_ls_number_restraints      973
_refine_ls_R_factor_all           0.0599
_refine_ls_R_factor_gt            0.0561
_refine_ls_wR_factor_ref          0.1625
```

_refine_ls_wR_factor_gt 0.1579
_refine_ls_goodness_of_fit_ref 1.046
_refine_ls_restrained_S_all 1.806
_refine_ls_shift/su_max 3.586
_refine_ls_shift/su_mean 0.019

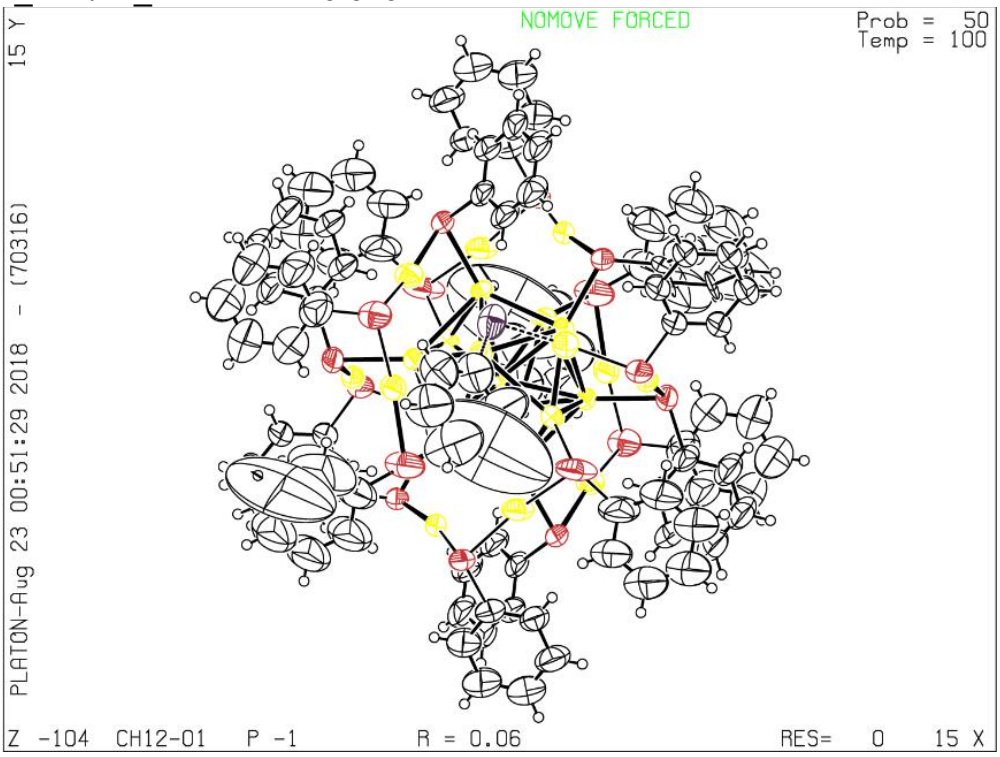


Figure A.10 ORTEP plot for crystal structure “CH12-01”.

A.17 Crystallographic Information File for Crystal #1 1 eq. 10 Days

The full CIF can be found at https://pubs.acs.org/doi/10.1021/jacs.8b10013

data_CH7-02

_audit_creation_method 'SHELXL-2014/7'
_shelx_SHELXL_version_number '2014/7'
_chemical_name_systematic ?
_chemical_name_common ?
_chemical_melting_point ?
_chemical_formula_moiety 'C108 H90 Au25 S1.35 Se16.65, C21 N'
_chemical_formula_sum
'C129 H90 Au25 N S1.35 Se16.65'
_chemical_formula_weight 7936.14

loop_
_atom_type_symbol

```
 _atom_type_description
 _atom_type_scat_dispersion_real
 _atom_type_scat_dispersion_imag
 _atom_type_scat_source
'Au'  'Au'  -8.6060   9.5200
'International Tables Vol C Tables 4.2.6.8 and 6.1.1.4'
'Se'  'Se'  -3.3840   0.5190
'International Tables Vol C Tables 4.2.6.8 and 6.1.1.4'
'C'  'C'   0.0080   0.0030
'International Tables Vol C Tables 4.2.6.8 and 6.1.1.4'
'N'  'N'   0.0140   0.0070
'International Tables Vol C Tables 4.2.6.8 and 6.1.1.4'
'H'  'H'   0.0000   0.0000
'International Tables Vol C Tables 4.2.6.8 and 6.1.1.4'
'S'  'S'   0.2070   0.2440
 'International Tables Vol C Tables 4.2.6.8 and 6.1.1.4'

_space_group_crystal_system      triclinic
_space_group_IT_number           2
_space_group_name_H-M_alt        'P -1'
_space_group_name_Hall           '-P 1'

_shelx_space_group_comment
;
The symmetry employed for this shelxl refinement is uniquely defined
by the following loop, which should always be used as a source of
symmetry information in preference to the above space-group names.
They are only intended as comments.
;

loop_
 _space_group_symop_operation_xyz
 'x, y, z'
 '-x, -y, -z'

_cell_length_a                 16.555(3)
_cell_length_b                 20.257(4)
_cell_length_c                 23.831(5)
_cell_angle_alpha                83.18(3)
_cell_angle_beta                 80.08(3)
_cell_angle_gamma                  81.70(3)
_cell_volume                   7754(3)
_cell_formula_units_Z            2
_cell_measurement_temperature    100(2)
_cell_measurement_reflns_used    11019
_cell_measurement_theta_min      1.228
```

```
_cell_measurement_theta_max       28.766

_exptl_crystal_description        'Parallelogram prism'
_exptl_crystal_colour             Black
_exptl_crystal_density_meas       ?
_exptl_crystal_density_method     ?
_exptl_crystal_density_diffrn     3.399
_exptl_crystal_F_000              6867
_exptl_transmission_factor_min    ?
_exptl_transmission_factor_max    ?
_exptl_crystal_size_max           ?
_exptl_crystal_size_mid           ?
_exptl_crystal_size_min           ?
_exptl_absorpt_coefficient_mu     35.968
_shelx_estimated_absorpt_T_min    ?
_shelx_estimated_absorpt_T_max    ?
_exptl_absorpt_correction_type    ?
_exptl_absorpt_correction_T_min   ?
_exptl_absorpt_correction_T_max   ?
_exptl_absorpt_process_details    ?
_exptl_absorpt_special_details    ?
_diffrn_ambient_temperature       100(2)
_diffrn_radiation_wavelength      1.000
_diffrn_radiation_type            Synchrotron
_diffrn_source                    'Advanced Light Source Beamline 4.2.2'
_diffrn_measurement_device_type   Synchrotron
_diffrn_measurement_method        ?
_diffrn_detector_area_resol_mean  ?
_diffrn_reflns_number             21093
_diffrn_reflns_av_unetI/netI      0.1022
_diffrn_reflns_av_R_equivalents   0.0475
_diffrn_reflns_limit_h_min        -15
_diffrn_reflns_limit_h_max        15
_diffrn_reflns_limit_k_min        -19
_diffrn_reflns_limit_k_max        19
_diffrn_reflns_limit_l_min        -22
_diffrn_reflns_limit_l_max        22
_diffrn_reflns_theta_min          1.226
_diffrn_reflns_theta_max          28.798
_diffrn_reflns_theta_full         11.660
_diffrn_measured_fraction_theta_max   0.760
_diffrn_measured_fraction_theta_full  0.593
_diffrn_reflns_Laue_measured_fraction_max    0.760
_diffrn_reflns_Laue_measured_fraction_full   0.593
_diffrn_reflns_point_group_measured_fraction_max   0.760
_diffrn_reflns_point_group_measured_fraction_full  0.593
```

```
_reflns_number_total              11019
_reflns_number_gt                 10218
_reflns_threshold_expression      'I > 2\s(I)'
_reflns_Friedel_coverage          0.000
_reflns_Friedel_fraction_max      .
_reflns_Friedel_fraction_full     .

_reflns_special_details
;
 Reflections were merged by SHELXL according to the crystal
 class for the calculation of statistics and refinement.

 Structure factors included contributions from the .fab file.

 _reflns_Friedel_fraction is defined as the number of unique
 Friedel pairs measured divided by the number that would be
 possible theoretically, ignoring centric projections and
 systematic absences.
;

_computing_data_collection        ?
_computing_cell_refinement        ?
_computing_data_reduction         ?
_computing_structure_solution     ?
_computing_structure_refinement 'SHELXL-2014/7 (Sheldrick, 2014)'
_computing_molecular_graphics     ?
_computing_publication_material   ?
_refine_special_details           ?
_refine_ls_structure_factor_coef  Fsqd
_refine_ls_matrix_type            full
_refine_ls_weighting_scheme       calc
_refine_ls_weighting_details
'w=1/[\s^2^(Fo^2^)+124.0166P] where P=(Fo^2^+2Fc^2^)/3'
_atom_sites_solution_primary      ?
_atom_sites_solution_secondary    ?
_atom_sites_solution_hydrogens    geom
_refine_ls_hydrogen_treatment     constr
_refine_ls_extinction_method      none
_refine_ls_extinction_coef        .
_refine_ls_number_reflns          11019
_refine_ls_number_parameters      1357
_refine_ls_number_restraints      2763
_refine_ls_R_factor_all           0.0529
_refine_ls_R_factor_gt            0.0493
_refine_ls_wR_factor_ref          0.1417
_refine_ls_wR_factor_gt           0.1352
```

_refine_ls_goodness_of_fit_ref 1.033
_refine_ls_restrained_S_all 0.928
_refine_ls_shift/su_max 0.001
_refine_ls_shift/su_mean 0.000

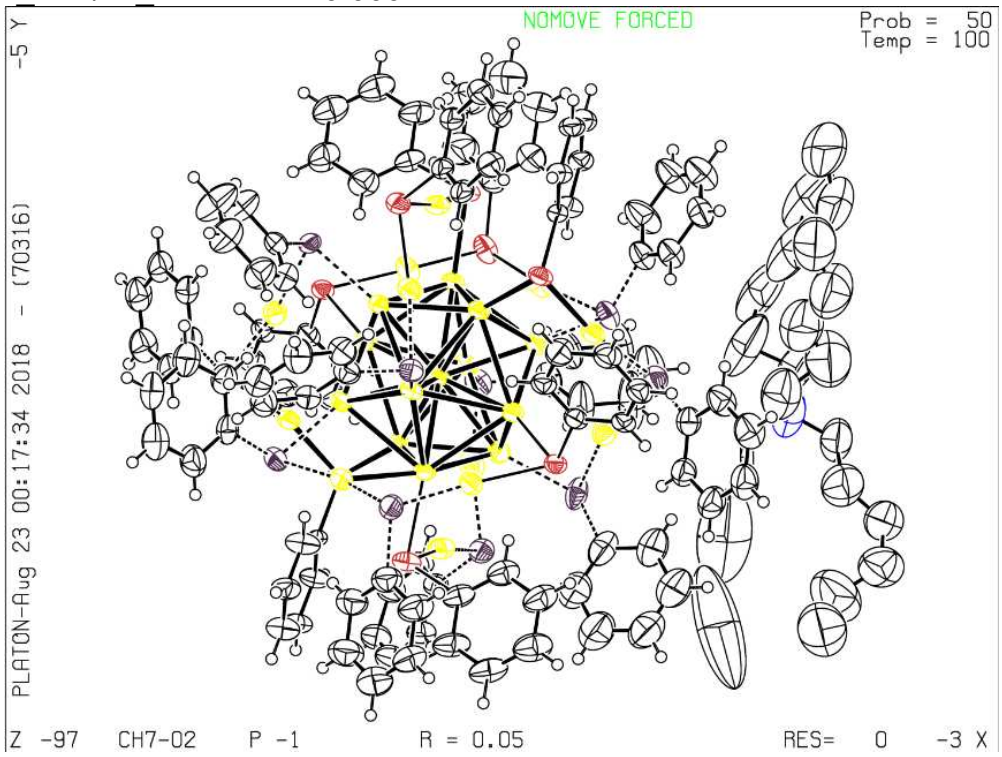


Figure A.11 ORTEP plot of crystal structure “CH7-02”.

A.18 Crystallographic Information File for Crystal #2 1 eq. 10 Days

The full CIF can be found at https://pubs.acs.org/doi/10.1021/jacs.8b10013

data_CH7-03

_audit_creation_method 'SHELXL-2014/7'
_shelx_SHELXL_version_number '2014/7'
_chemical_name_systematic ?
_chemical_name_common ?
_chemical_melting_point ?
_chemical_formula_moiety 'C108 H90 Au25 S1.21 Se16.79, C20 N'
_chemical_formula_sum
'C128 H90 Au25 N S1.21 Se16.79'
_chemical_formula_weight 7930.70

loop_
_atom_type_symbol
_atom_type_description

```
 _atom_type_scat_dispersion_real
 _atom_type_scat_dispersion_imag
 _atom_type_scat_source
'Au'  'Au'  -8.6060   9.5200
'International Tables Vol C Tables 4.2.6.8 and 6.1.1.4'
'Se'  'Se'  -3.3840   0.5190
'International Tables Vol C Tables 4.2.6.8 and 6.1.1.4'
'C'  'C'   0.0080   0.0030
'International Tables Vol C Tables 4.2.6.8 and 6.1.1.4'
'N'  'N'   0.0140   0.0070
'International Tables Vol C Tables 4.2.6.8 and 6.1.1.4'
'H'  'H'   0.0000   0.0000
'International Tables Vol C Tables 4.2.6.8 and 6.1.1.4'
'S'  'S'   0.2070   0.2440
'International Tables Vol C Tables 4.2.6.8 and 6.1.1.4'

_space_group_crystal_system      triclinic
_space_group_IT_number           2
_space_group_name_H-M_alt        'P -1'
_space_group_name_Hall           '-P 1'

_shelx_space_group_comment
;
The symmetry employed for this shelxl refinement is uniquely defined
by the following loop, which should always be used as a source of
symmetry information in preference to the above space-group names.
They are only intended as comments.
;

loop_
 _space_group_symop_operation_xyz
 'x, y, z'
 '-x, -y, -z'

_cell_length_a                 16.550(3)
_cell_length_b                 20.272(4)
_cell_length_c                 23.826(5)
_cell_angle_alpha                83.16(3)
_cell_angle_beta                 80.06(3)
_cell_angle_gamma                81.68(3)
_cell_volume                   7755(3)
_cell_formula_units_Z            2
_cell_measurement_temperature    100(2)
_cell_measurement_reflns_used    11808
_cell_measurement_theta_min      1.228
_cell_measurement_theta_max      28.766
```

```
_exptl_crystal_description        'Parallelogram prism'
_exptl_crystal_colour             Black
_exptl_crystal_density_meas       ?
_exptl_crystal_density_method     ?
_exptl_crystal_density_diffrn     3.396
_exptl_crystal_F_000              6860
_exptl_transmission_factor_min    ?
_exptl_transmission_factor_max    ?
_exptl_crystal_size_max           ?
_exptl_crystal_size_mid           ?
_exptl_crystal_size_min           ?
_exptl_absorpt_coefficient_mu     35.969
_shelx_estimated_absorpt_T_min    ?
_shelx_estimated_absorpt_T_max    ?
_exptl_absorpt_correction_type    ?
_exptl_absorpt_correction_T_min   ?
_exptl_absorpt_correction_T_max   ?
_exptl_absorpt_process_details    ?
_exptl_absorpt_special_details    ?
_diffrn_ambient_temperature       100(2)
_diffrn_radiation_wavelength      1.000
_diffrn_radiation_type            Synchrotron
_diffrn_source                    'Advanced Light Source Beamline 4.2.2'
_diffrn_measurement_device_type   Synchrotron
_diffrn_measurement_method        ?
_diffrn_detector_area_resol_mean  ?
_diffrn_reflns_number             22651
_diffrn_reflns_av_unetI/netI      0.1519
_diffrn_reflns_av_R_equivalents   0.0796
_diffrn_reflns_limit_h_min        -15
_diffrn_reflns_limit_h_max        15
_diffrn_reflns_limit_k_min        -19
_diffrn_reflns_limit_k_max        19
_diffrn_reflns_limit_l_min        -22
_diffrn_reflns_limit_l_max        22
_diffrn_reflns_theta_min          1.227
_diffrn_reflns_theta_max          28.755
_diffrn_reflns_theta_full         11.660
_diffrn_measured_fraction_theta_max   0.817
_diffrn_measured_fraction_theta_full  0.691
_diffrn_reflns_Laue_measured_fraction_max    0.817
_diffrn_reflns_Laue_measured_fraction_full   0.691
_diffrn_reflns_point_group_measured_fraction_max   0.817
_diffrn_reflns_point_group_measured_fraction_full  0.691
_reflns_number_total              11808
```

```
_reflns_number_gt                10436
_reflns_threshold_expression      'I > 2\s(I)'
_reflns_Friedel_coverage          0.000
_reflns_Friedel_fraction_max      .
_reflns_Friedel_fraction_full     .

_reflns_special_details
;
 Reflections were merged by SHELXL according to the crystal
 class for the calculation of statistics and refinement.

 Structure factors included contributions from the .fab file.

 _reflns_Friedel_fraction is defined as the number of unique
 Friedel pairs measured divided by the number that would be
 possible theoretically, ignoring centric projections and
 systematic absences.
;

_computing_data_collection        ?
_computing_cell_refinement        ?
_computing_data_reduction         ?
_computing_structure_solution     ?
_computing_structure_refinement 'SHELXL-2014/7 (Sheldrick, 2014)'
_computing_molecular_graphics     ?
_computing_publication_material   ?
_refine_special_details           ?
_refine_ls_structure_factor_coef  Fsqd
_refine_ls_matrix_type            full
_refine_ls_weighting_scheme       calc
_refine_ls_weighting_details
'w=1/[\s^2^(Fo^2^)+(0.0486P)^2^+91.9871P] where P=(Fo^2^+2Fc^2^)/3'
_atom_sites_solution_primary      ?
_atom_sites_solution_secondary    ?
_atom_sites_solution_hydrogens    geom
_refine_ls_hydrogen_treatment     constr
_refine_ls_extinction_method      none
_refine_ls_extinction_coef        .
_refine_ls_number_reflns          11808
_refine_ls_number_parameters      1344
_refine_ls_number_restraints      2619
_refine_ls_R_factor_all           0.0714
_refine_ls_R_factor_gt            0.0664
_refine_ls_wR_factor_ref          0.1849
_refine_ls_wR_factor_gt           0.1807
_refine_ls_goodness_of_fit_ref    1.037
```

_refine_ls_restrained_S_all 0.957
_refine_ls_shift/su_max 0.001
_refine_ls_shift/su_mean 0.000

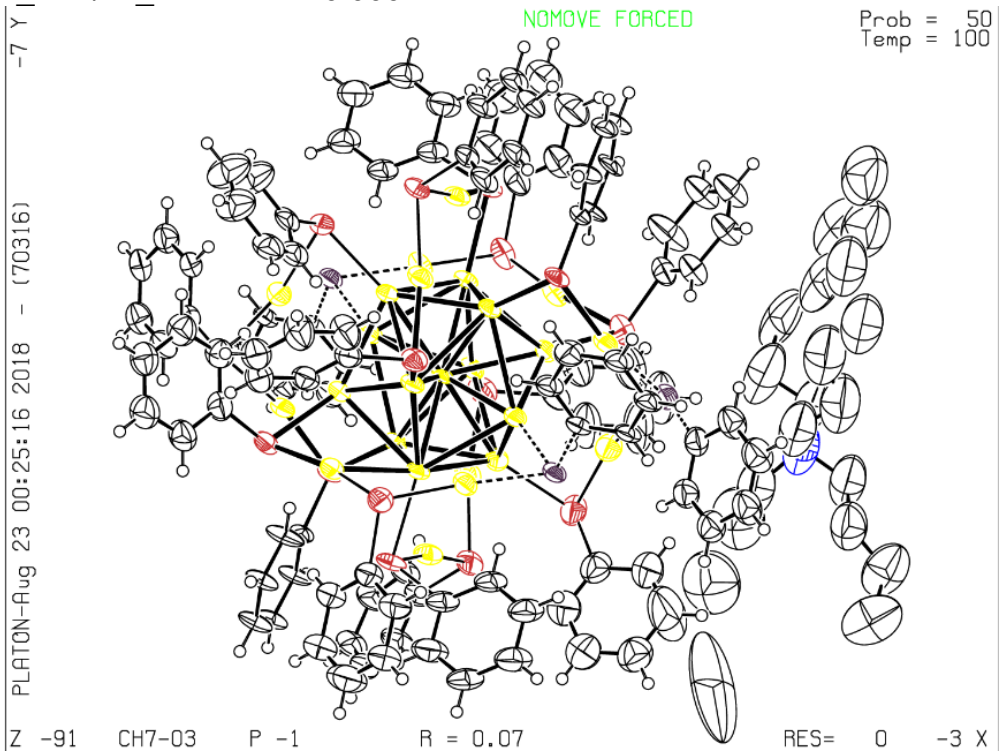


Figure A.12 ORTEP plot for crystal structure “CH7-03”.

A.19 Crystallographic Information File for Crystal #3 1 eq. 10 Days

The full CIF can be found at https://pubs.acs.org/doi/10.1021/jacs.8b10013

data_CH8-03

_audit_creation_method 'SHELXL-2014/7'
_shelx_SHELXL_version_number '2014/7'
_chemical_name_systematic ?
_chemical_name_common ?
_chemical_melting_point ?
_chemical_formula_moiety 'C108 H90 Au25 S1.19 Se16.81, C23 N'
_chemical_formula_sum
'C131 H90 Au25 N S1.19 Se16.81'
_chemical_formula_weight 7967.67

loop_
_atom_type_symbol
_atom_type_description
_atom_type_scat_dispersion_real

```
 _atom_type_scat_dispersion_imag
 _atom_type_scat_source
'Au'  'Au'  -8.6060   9.5200
'International Tables Vol C Tables 4.2.6.8 and 6.1.1.4'
'Se'  'Se'  -3.3840   0.5190
'International Tables Vol C Tables 4.2.6.8 and 6.1.1.4'
'C'  'C'   0.0080   0.0030
'International Tables Vol C Tables 4.2.6.8 and 6.1.1.4'
'N'  'N'   0.0140   0.0070
'International Tables Vol C Tables 4.2.6.8 and 6.1.1.4'
'H'  'H'   0.0000   0.0000
'International Tables Vol C Tables 4.2.6.8 and 6.1.1.4'
'S'  'S'   0.2070   0.2440
'International Tables Vol C Tables 4.2.6.8 and 6.1.1.4'

_space_group_crystal_system       triclinic
_space_group_IT_number           2
_space_group_name_H-M_alt        'P -1'
_space_group_name_Hall           '-P 1'

_shelx_space_group_comment
;
The symmetry employed for this shelxl refinement is uniquely defined
by the following loop, which should always be used as a source of
symmetry information in preference to the above space-group names.
They are only intended as comments.
;

loop_
 _space_group_symop_operation_xyz
 'x, y, z'
 '-x, -y, -z'

_cell_length_a                 16.558(3)
_cell_length_b                 20.277(4)
_cell_length_c                 23.823(5)
_cell_angle_alpha                83.13(3)
_cell_angle_beta                 80.10(3)
_cell_angle_gamma                81.66(3)
_cell_volume                   7759(3)
_cell_formula_units_Z            2
_cell_measurement_temperature     100(2)
_cell_measurement_reflns_used     10765
_cell_measurement_theta_min       1.228
_cell_measurement_theta_max       28.766
```

```
_exptl_crystal_description       'Parallelogram prism'
_exptl_crystal_colour            Black
_exptl_crystal_density_meas      ?
_exptl_crystal_density_method    ?
_exptl_crystal_density_diffrn    3.410
_exptl_crystal_F_000             6897
_exptl_transmission_factor_min   ?
_exptl_transmission_factor_max   ?
_exptl_crystal_size_max          ?
_exptl_crystal_size_mid          ?
_exptl_crystal_size_min          ?
_exptl_absorpt_coefficient_mu    35.950
_shelx_estimated_absorpt_T_min   ?
_shelx_estimated_absorpt_T_max   ?
_exptl_absorpt_correction_type   ?
_exptl_absorpt_correction_T_min  ?
_exptl_absorpt_correction_T_max  ?
_exptl_absorpt_process_details   ?
_exptl_absorpt_special_details   ?
_diffrn_ambient_temperature      100(2)
_diffrn_radiation_wavelength     1.000
_diffrn_radiation_type           Synchrotron
_diffrn_source                   'Advanced Light Source Beamline 4.2.2'
_diffrn_measurement_device_type  Synchrotron
_diffrn_measurement_method       ?
_diffrn_detector_area_resol_mean ?
_diffrn_reflns_number            20393
_diffrn_reflns_av_unetI/netI     0.0982
_diffrn_reflns_av_R_equivalents  0.0483
_diffrn_reflns_limit_h_min       -15
_diffrn_reflns_limit_h_max       15
_diffrn_reflns_limit_k_min       -19
_diffrn_reflns_limit_k_max       19
_diffrn_reflns_limit_l_min       -22
_diffrn_reflns_limit_l_max       22
_diffrn_reflns_theta_min         1.227
_diffrn_reflns_theta_max         28.761
_diffrn_reflns_theta_full        11.660
_diffrn_measured_fraction_theta_max  0.744
_diffrn_measured_fraction_theta_full 0.567
_diffrn_reflns_Laue_measured_fraction_max  0.744
_diffrn_reflns_Laue_measured_fraction_full  0.567
_diffrn_reflns_point_group_measured_fraction_max  0.744
_diffrn_reflns_point_group_measured_fraction_full 0.567
_reflns_number_total             10765
_reflns_number_gt                9984
```

```
_reflns_threshold_expression      'I > 2\s(I)'
_reflns_Friedel_coverage          0.000
_reflns_Friedel_fraction_max      .
_reflns_Friedel_fraction_full     .

_reflns_special_details
;
 Reflections were merged by SHELXL according to the crystal
 class for the calculation of statistics and refinement.

 Structure factors included contributions from the .fab file.

 _reflns_Friedel_fraction is defined as the number of unique
 Friedel pairs measured divided by the number that would be
 possible theoretically, ignoring centric projections and
 systematic absences.
;

_computing_data_collection        ?
_computing_cell_refinement        ?
_computing_data_reduction         ?
_computing_structure_solution     ?
_computing_structure_refinement 'SHELXL-2014/7 (Sheldrick, 2014)'
_computing_molecular_graphics     ?
_computing_publication_material   ?
_refine_special_details           ?
_refine_ls_structure_factor_coef  Fsqd
_refine_ls_matrix_type            full
_refine_ls_weighting_scheme       calc
_refine_ls_weighting_details
'w=1/[\s^2^(Fo^2^)+(0.0558P)^2^+152.3082P] where P=(Fo^2^+2Fc^2^)/3'
_atom_sites_solution_primary      ?
_atom_sites_solution_secondary    ?
_atom_sites_solution_hydrogens    geom
_refine_ls_hydrogen_treatment     constr
_refine_ls_extinction_method      none
_refine_ls_extinction_coef        .
_refine_ls_number_reflns          10765
_refine_ls_number_parameters      1372
_refine_ls_number_restraints      2673
_refine_ls_R_factor_all           0.0605
_refine_ls_R_factor_gt            0.0572
_refine_ls_wR_factor_ref          0.1598
_refine_ls_wR_factor_gt           0.1567
_refine_ls_goodness_of_fit_ref    1.051
_refine_ls_restrained_S_all       0.950
```

_refine_ls_shift/su_max 0.100
_refine_ls_shift/su_mean 0.000

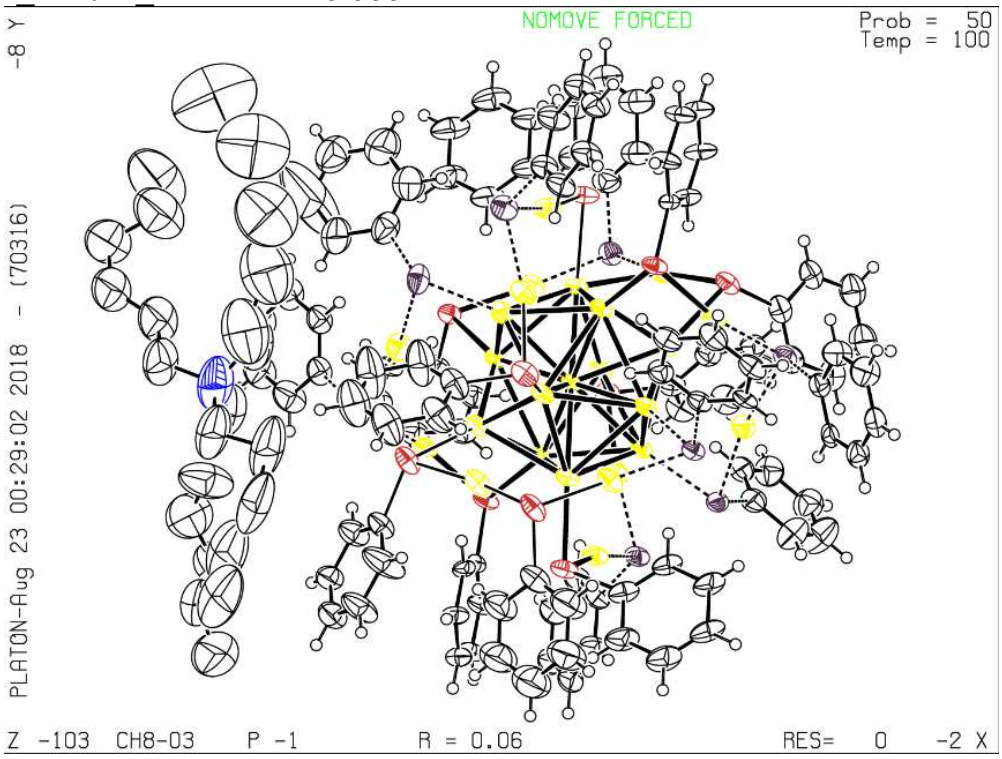


Figure A.13 ORTEP plot for crystal structure “CH8-03”.

A.20 Crystallographic Information File for Crystal #1 1 eq. 15 Days

The full CIF can be found at https://pubs.acs.org/doi/10.1021/jacs.8b10013

data_CH13-01

_audit_creation_method 'SHELXL-2014/7'
_shelx_SHELXL_version_number '2014/7'
_chemical_name_systematic ?
_chemical_name_common ?
_chemical_melting_point ?
_chemical_formula_moiety 'C108 H90 Au25 S1.36 Se16.64, C25 N'
_chemical_formula_sum
'C133 H90 Au25 N S1.36 Se16.64'
_chemical_formula_weight 7983.71

loop_
_atom_type_symbol
_atom_type_description
_atom_type_scat_dispersion_real
_atom_type_scat_dispersion_imag

```
 _atom_type_scat_source
 'Au'  'Au'  -8.6060   9.5200
 'International Tables Vol C Tables 4.2.6.8 and 6.1.1.4'
 'Se'  'Se'  -3.3840   0.5190
 'International Tables Vol C Tables 4.2.6.8 and 6.1.1.4'
 'C'  'C'   0.0080   0.0030
 'International Tables Vol C Tables 4.2.6.8 and 6.1.1.4'
 'N'  'N'   0.0140   0.0070
 'International Tables Vol C Tables 4.2.6.8 and 6.1.1.4'
 'S'  'S'   0.2070   0.2440
 'International Tables Vol C Tables 4.2.6.8 and 6.1.1.4'
 'H'  'H'   0.0000   0.0000
 'International Tables Vol C Tables 4.2.6.8 and 6.1.1.4'

_space_group_crystal_system      triclinic
_space_group_IT_number           2
_space_group_name_H-M_alt        'P -1'
_space_group_name_Hall           '-P 1'

_shelx_space_group_comment
;
The symmetry employed for this shelxl refinement is uniquely defined
by the following loop, which should always be used as a source of
symmetry information in preference to the above space-group names.
They are only intended as comments.
;

loop_
 _space_group_symop_operation_xyz
 'x, y, z'
 '-x, -y, -z'

_cell_length_a                   16.548(3)
_cell_length_b                   20.264(4)
_cell_length_c                   23.797(5)
_cell_angle_alpha                  83.25(3)
_cell_angle_beta                 80.14(3)
_cell_angle_gamma                  81.74(3)
_cell_volume                     7745(3)
_cell_formula_units_Z            2
_cell_measurement_temperature    100(2)
_cell_measurement_reflns_used    11719
_cell_measurement_theta_min      1.228
_cell_measurement_theta_max      28.766

_exptl_crystal_description       'Parallelogram prism'
```

```
_exptl_crystal_colour            Black
_exptl_crystal_density_meas      ?
_exptl_crystal_density_method    ?
_exptl_crystal_density_diffrn    3.423
_exptl_crystal_F_000             6915
_exptl_transmission_factor_min   ?
_exptl_transmission_factor_max   ?
_exptl_crystal_size_max          ?
_exptl_crystal_size_mid          ?
_exptl_crystal_size_min          ?
_exptl_absorpt_coefficient_mu    36.010
_shelx_estimated_absorpt_T_min   ?
_shelx_estimated_absorpt_T_max   ?
_exptl_absorpt_correction_type   ?
_exptl_absorpt_correction_T_min  ?
_exptl_absorpt_correction_T_max  ?
_exptl_absorpt_process_details   ?
_exptl_absorpt_special_details   ?
_diffrn_ambient_temperature      100(2)
_diffrn_radiation_wavelength     1.000
_diffrn_radiation_type           Synchrotron
_diffrn_source                   'Advanced Light Source Beamline 4.2.2'
_diffrn_measurement_device_type  Synchrotron
_diffrn_measurement_method       ?
_diffrn_detector_area_resol_mean ?
_diffrn_reflns_number            22652
_diffrn_reflns_av_unetI/netI     0.1156
_diffrn_reflns_av_R_equivalents  0.0641
_diffrn_reflns_limit_h_min       -15
_diffrn_reflns_limit_h_max       15
_diffrn_reflns_limit_k_min       -18
_diffrn_reflns_limit_k_max       19
_diffrn_reflns_limit_l_min       -22
_diffrn_reflns_limit_l_max       22
_diffrn_reflns_theta_min         1.435
_diffrn_reflns_theta_max         28.770
_diffrn_reflns_theta_full        11.660
_diffrn_measured_fraction_theta_max  0.811
_diffrn_measured_fraction_theta_full 0.696
_diffrn_reflns_Laue_measured_fraction_max   0.811
_diffrn_reflns_Laue_measured_fraction_full  0.696
_diffrn_reflns_point_group_measured_fraction_max  0.811
_diffrn_reflns_point_group_measured_fraction_full 0.696
_reflns_number_total             11719
_reflns_number_gt                10075
_reflns_threshold_expression     'I > 2\s(I)'
```

```
_reflns_Friedel_coverage          0.000
_reflns_Friedel_fraction_max      .
_reflns_Friedel_fraction_full     .

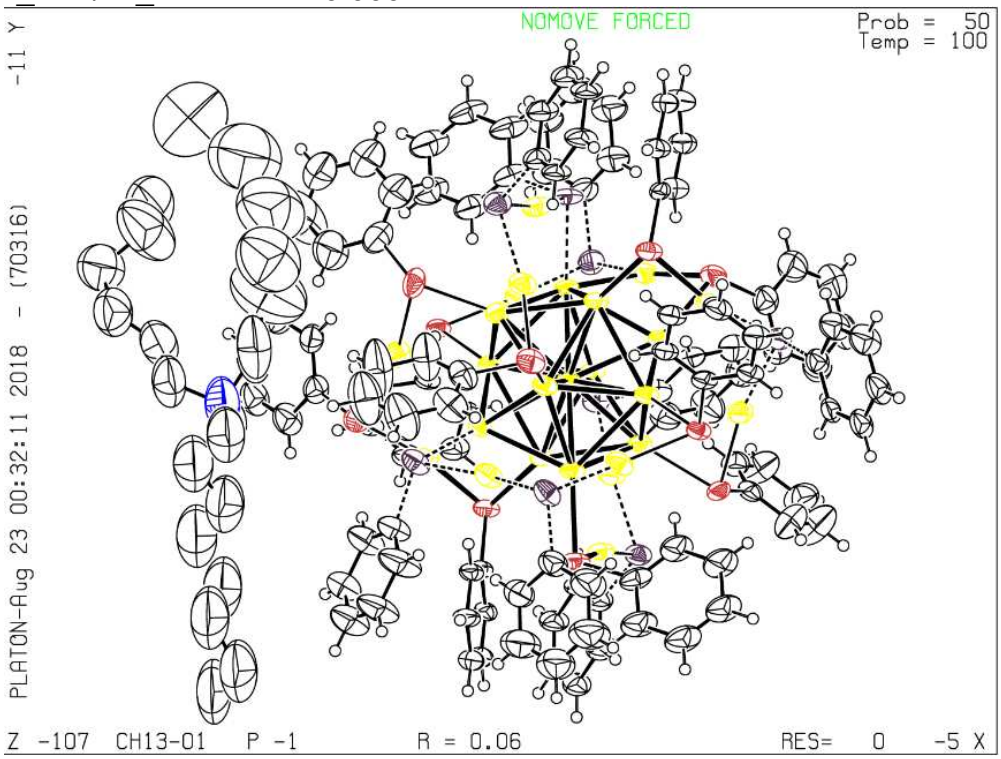
_reflns_special_details
;
 Reflections were merged by SHELXL according to the crystal
 class for the calculation of statistics and refinement.

 Structure factors included contributions from the .fab file.

 _reflns_Friedel_fraction is defined as the number of unique
 Friedel pairs measured divided by the number that would be
 possible theoretically, ignoring centric projections and
 systematic absences.
;

_computing_data_collection        ?
_computing_cell_refinement        ?
_computing_data_reduction         ?
_computing_structure_solution     ?
_computing_structure_refinement 'SHELXL-2014/7 (Sheldrick, 2014)'
_computing_molecular_graphics     ?
_computing_publication_material   ?
_refine_special_details           ?
_refine_ls_structure_factor_coef  Fsqd
_refine_ls_matrix_type            full
_refine_ls_weighting_scheme       calc
_refine_ls_weighting_details
'w=1/[\s^2^(Fo^2^)+(0.0364P)^2^+148.0441P] where P=(Fo^2^+2Fc^2^)/3'
_atom_sites_solution_primary      ?
_atom_sites_solution_secondary    ?
_atom_sites_solution_hydrogens    geom
_refine_ls_hydrogen_treatment     constr
_refine_ls_extinction_method      none
_refine_ls_extinction_coef        .
_refine_ls_number_reflns          11719
_refine_ls_number_parameters      1365
_refine_ls_number_restraints      2754
_refine_ls_R_factor_all           0.0668
_refine_ls_R_factor_gt            0.0602
_refine_ls_wR_factor_ref          0.1680
_refine_ls_wR_factor_gt           0.1634
_refine_ls_goodness_of_fit_ref    1.060
_refine_ls_restrained_S_all       0.957
_refine_ls_shift/su_max           0.001
```

_refine_ls_shift/su_mean 0.000



Figures A.14 ORTEP plot for crystal structure “CH13-01”.

A.21 Crystallographic Information File for Crystal #2 1 eq. 15 Days

The full CIF can be found at https://pubs.acs.org/doi/10.1021/jacs.8b10013

data_CH14-02

_audit_creation_method 'SHELXL-2014/7'
_shelx_SHELXL_version_number '2014/7'
_chemical_name_systematic ?
_chemical_name_common ?
_chemical_melting_point ?
_chemical_formula_moiety 'C108 H90 Au25 S1.34 Se16.66'
_chemical_formula_sum
'C122 H90 Au25 N S1.34 Se16.66'
_chemical_formula_weight 7852.54

loop_
_atom_type_symbol
_atom_type_description
_atom_type_scat_dispersion_real
_atom_type_scat_dispersion_imag
_atom_type_scat_source

```
 'Au'  'Au'  -8.6060   9.5200
 'International Tables Vol C Tables 4.2.6.8 and 6.1.1.4'
 'Se'  'Se'  -3.3840   0.5190
 'International Tables Vol C Tables 4.2.6.8 and 6.1.1.4'
 'C'  'C'   0.0080   0.0030
 'International Tables Vol C Tables 4.2.6.8 and 6.1.1.4'
 'N'  'N'   0.0140   0.0070
 'International Tables Vol C Tables 4.2.6.8 and 6.1.1.4'
 'S'  'S'   0.2070   0.2440
 'International Tables Vol C Tables 4.2.6.8 and 6.1.1.4'
 'H'  'H'   0.0000   0.0000
 'International Tables Vol C Tables 4.2.6.8 and 6.1.1.4'

_space_group_crystal_system      triclinic
_space_group_IT_number           2
_space_group_name_H-M_alt        'P -1'
_space_group_name_Hall           '-P 1'

_shelx_space_group_comment
;
The symmetry employed for this shelxl refinement is uniquely defined
by the following loop, which should always be used as a source of
symmetry information in preference to the above space-group names.
They are only intended as comments.
;

loop_
 _space_group_symop_operation_xyz
 'x, y, z'
 '-x, -y, -z'

_cell_length_a                 16.552(3)
_cell_length_b                 20.297(4)
_cell_length_c                 23.828(5)
_cell_angle_alpha                83.14(3)
_cell_angle_beta                 80.05(3)
_cell_angle_gamma                81.62(3)
_cell_volume                   7764(3)
_cell_formula_units_Z            2
_cell_measurement_temperature    100(2)
_cell_measurement_reflns_used    11958
_cell_measurement_theta_min      1.228
_cell_measurement_theta_max      28.766

_exptl_crystal_description       'Parallelogram prism'
_exptl_crystal_colour            Black
```

```
_exptl_crystal_density_meas       ?
_exptl_crystal_density_method     ?
_exptl_crystal_density_diffrn     3.359
_exptl_crystal_F_000              6784
_exptl_transmission_factor_min    ?
_exptl_transmission_factor_max    ?
_exptl_crystal_size_max           ?
_exptl_crystal_size_mid           ?
_exptl_crystal_size_min           ?
_exptl_absorpt_coefficient_mu     35.917
_shelx_estimated_absorpt_T_min    ?
_shelx_estimated_absorpt_T_max    ?
_exptl_absorpt_correction_type    ?
_exptl_absorpt_correction_T_min   ?
_exptl_absorpt_correction_T_max   ?
_exptl_absorpt_process_details    ?
_exptl_absorpt_special_details    ?
_diffrn_ambient_temperature       100(2)
_diffrn_radiation_wavelength      1.000
_diffrn_radiation_type            Synchrotron
_diffrn_source                    'Advanced Light Source Beamline 4.2.2'
_diffrn_measurement_device_type   Synchrotron
_diffrn_measurement_method        ?
_diffrn_detector_area_resol_mean  ?
_diffrn_reflns_number             23202
_diffrn_reflns_av_unetI/netI      0.1042
_diffrn_reflns_av_R_equivalents   0.0538
_diffrn_reflns_limit_h_min        -15
_diffrn_reflns_limit_h_max        15
_diffrn_reflns_limit_k_min        -18
_diffrn_reflns_limit_k_max        19
_diffrn_reflns_limit_l_min        -21
_diffrn_reflns_limit_l_max        22
_diffrn_reflns_theta_min          1.226
_diffrn_reflns_theta_max          28.760
_diffrn_reflns_theta_full         11.660
_diffrn_measured_fraction_theta_max   0.826
_diffrn_measured_fraction_theta_full  0.718
_diffrn_reflns_Laue_measured_fraction_max    0.826
_diffrn_reflns_Laue_measured_fraction_full   0.718
_diffrn_reflns_point_group_measured_fraction_max   0.826
_diffrn_reflns_point_group_measured_fraction_full  0.718
_reflns_number_total              11959
_reflns_number_gt                 10188
_reflns_threshold_expression      'I > 2\s(I)'
_reflns_Friedel_coverage          0.000
```

```
_reflns_Friedel_fraction_max      .
_reflns_Friedel_fraction_full     .

_reflns_special_details
;
 Reflections were merged by SHELXL according to the crystal
 class for the calculation of statistics and refinement.

 Structure factors included contributions from the .fab file.

 _reflns_Friedel_fraction is defined as the number of unique
 Friedel pairs measured divided by the number that would be
 possible theoretically, ignoring centric projections and
 systematic absences.
;

_computing_data_collection        ?
_computing_cell_refinement        ?
_computing_data_reduction         ?
_computing_structure_solution     ?
_computing_structure_refinement 'SHELXL-2014/7 (Sheldrick, 2014)'
_computing_molecular_graphics     ?
_computing_publication_material   ?
_refine_special_details           ?
_refine_ls_structure_factor_coef  Fsqd
_refine_ls_matrix_type            full
_refine_ls_weighting_scheme       calc
_refine_ls_weighting_details
'w=1/[\s^2^(Fo^2^)+(0.0794P)^2^+70.7030P] where P=(Fo^2^+2Fc^2^)/3'
_atom_sites_solution_primary      ?
_atom_sites_solution_secondary    ?
_atom_sites_solution_hydrogens    geom
_refine_ls_hydrogen_treatment     constr
_refine_ls_extinction_method      none
_refine_ls_extinction_coef        .
_refine_ls_number_reflns          11959
_refine_ls_number_parameters      1277
_refine_ls_number_restraints      2745
_refine_ls_R_factor_all           0.0658
_refine_ls_R_factor_gt            0.0590
_refine_ls_wR_factor_ref          0.1728
_refine_ls_wR_factor_gt           0.1672
_refine_ls_goodness_of_fit_ref    1.077
_refine_ls_restrained_S_all       0.973
_refine_ls_shift/su_max           0.001
_refine_ls_shift/su_mean          0.000
```

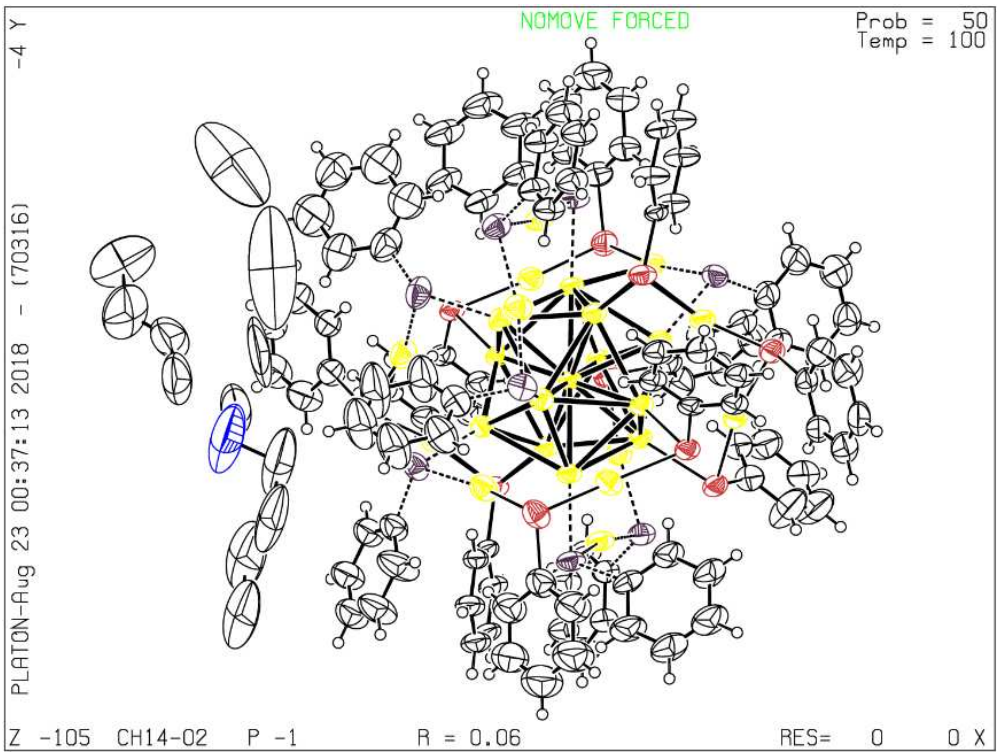


Figure A.15 ORTEP plot for crystal structure “CH14-02”.

A.22 Crystallographic Information File for Crystal #3 1 eq. 15 Days

The full CIF can be found at https://pubs.acs.org/doi/10.1021/jacs.8b10013

data_CH14-03

_audit_creation_method 'SHELXL-2014/7'
_shelx_SHELXL_version_number '2014/7'
_chemical_name_systematic ?
_chemical_name_common ?
_chemical_melting_point ?
_chemical_formula_moiety 'C108 H90 Au25 S1.34 Se16.66, C16 N'
_chemical_formula_sum
'C124 H90 Au25 N S1.34 Se16.66'
_chemical_formula_weight 7876.56

loop_
_atom_type_symbol
_atom_type_description
_atom_type_scat_dispersion_real
_atom_type_scat_dispersion_imag
_atom_type_scat_source
'Se' 'Se' -3.3840 0.5190

```
 'International Tables Vol C Tables 4.2.6.8 and 6.1.1.4'
 'Au'  'Au'  -8.6060   9.5200
 'International Tables Vol C Tables 4.2.6.8 and 6.1.1.4'
 'C'  'C'   0.0080   0.0030
 'International Tables Vol C Tables 4.2.6.8 and 6.1.1.4'
 'H'  'H'   0.0000   0.0000
 'International Tables Vol C Tables 4.2.6.8 and 6.1.1.4'
 'S'  'S'   0.2070   0.2440
 'International Tables Vol C Tables 4.2.6.8 and 6.1.1.4'
 'N'  'N'   0.0140   0.0070
 'International Tables Vol C Tables 4.2.6.8 and 6.1.1.4'

_space_group_crystal_system      triclinic
_space_group_IT_number           2
_space_group_name_H-M_alt        'P -1'
_space_group_name_Hall           '-P 1'

_shelx_space_group_comment
;
The symmetry employed for this shelxl refinement is uniquely defined
by the following loop, which should always be used as a source of
symmetry information in preference to the above space-group names.
They are only intended as comments.
;

loop_
 _space_group_symop_operation_xyz
 'x, y, z'
 '-x, -y, -z'

_cell_length_a                   16.574(3)
_cell_length_b                   20.332(4)
_cell_length_c                   23.845(5)
_cell_angle_alpha                  83.19(3)
_cell_angle_beta                 79.85(3)
_cell_angle_gamma                  81.50(3)
_cell_volume                     7787(3)
_cell_formula_units_Z            2
_cell_measurement_temperature    100(2)
_cell_measurement_reflns_used    11386
_cell_measurement_theta_min      1.228
_cell_measurement_theta_max      28.766

_exptl_crystal_description       'Parallelogram prism'
_exptl_crystal_colour            Black
_exptl_crystal_density_meas      ?
```

```
_exptl_crystal_density_method     ?
_exptl_crystal_density_diffrn     3.359
_exptl_crystal_F_000              6808
_exptl_transmission_factor_min    ?
_exptl_transmission_factor_max    ?
_exptl_crystal_size_max           ?
_exptl_crystal_size_mid           ?
_exptl_crystal_size_min           ?
_exptl_absorpt_coefficient_mu     35.810
_shelx_estimated_absorpt_T_min    ?
_shelx_estimated_absorpt_T_max    ?
_exptl_absorpt_correction_type    ?
_exptl_absorpt_correction_T_min   ?
_exptl_absorpt_correction_T_max   ?
_exptl_absorpt_process_details    ?
_exptl_absorpt_special_details    ?
_diffrn_ambient_temperature       100(2)
_diffrn_radiation_wavelength      1.000
_diffrn_radiation_type            Synchrotron
_diffrn_source                    'Advanced Light Source Beamline 4.2.2'
_diffrn_measurement_device_type   Synchrotron
_diffrn_measurement_method        ?
_diffrn_detector_area_resol_mean  ?
_diffrn_reflns_number             22119
_diffrn_reflns_av_unetI/netI      0.1468
_diffrn_reflns_av_R_equivalents   0.0771
_diffrn_reflns_limit_h_min        -15
_diffrn_reflns_limit_h_max        15
_diffrn_reflns_limit_k_min        -18
_diffrn_reflns_limit_k_max        18
_diffrn_reflns_limit_l_min        -21
_diffrn_reflns_limit_l_max        22
_diffrn_reflns_theta_min          1.431
_diffrn_reflns_theta_max          27.858
_diffrn_reflns_theta_full         11.660
_diffrn_measured_fraction_theta_max   0.855
_diffrn_measured_fraction_theta_full  0.706
_diffrn_reflns_Laue_measured_fraction_max    0.855
_diffrn_reflns_Laue_measured_fraction_full   0.706
_diffrn_reflns_point_group_measured_fraction_max   0.855
_diffrn_reflns_point_group_measured_fraction_full  0.706
_reflns_number_total              11386
_reflns_number_gt                 9234
_reflns_threshold_expression      'I > 2\s(I)'
_reflns_Friedel_coverage          0.000
_reflns_Friedel_fraction_max      .
```

_reflns_Friedel_fraction_full .

_reflns_special_details
;
Reflections were merged by SHELXL according to the crystal
class for the calculation of statistics and refinement.

Structure factors included contributions from the .fab file.

_reflns_Friedel_fraction is defined as the number of unique
Friedel pairs measured divided by the number that would be
possible theoretically, ignoring centric projections and
systematic absences.
;

_computing_data_collection ?
_computing_cell_refinement ?
_computing_data_reduction ?
_computing_structure_solution ?
_computing_structure_refinement 'SHELXL-2014/7 (Sheldrick, 2014)'
_computing_molecular_graphics ?
_computing_publication_material ?
_refine_special_details ?
_refine_ls_structure_factor_coef Fsqd
_refine_ls_matrix_type full
_refine_ls_weighting_scheme calc
_refine_ls_weighting_details
'w=1/[\s^2^(Fo^2^)+88.7911P] where P=(Fo^2^+2Fc^2^)/3'
_atom_sites_solution_primary ?
_atom_sites_solution_secondary ?
_atom_sites_solution_hydrogens geom
_refine_ls_hydrogen_treatment constr
_refine_ls_extinction_method none
_refine_ls_extinction_coef .
_refine_ls_number_reflns 11386
_refine_ls_number_parameters 1302
_refine_ls_number_restraints 2658
_refine_ls_R_factor_all 0.0766
_refine_ls_R_factor_gt 0.0652
_refine_ls_wR_factor_ref 0.1841
_refine_ls_wR_factor_gt 0.1746
_refine_ls_goodness_of_fit_ref 1.053
_refine_ls_restrained_S_all 0.959
_refine_ls_shift/su_max 0.001
_refine_ls_shift/su_mean 0.000

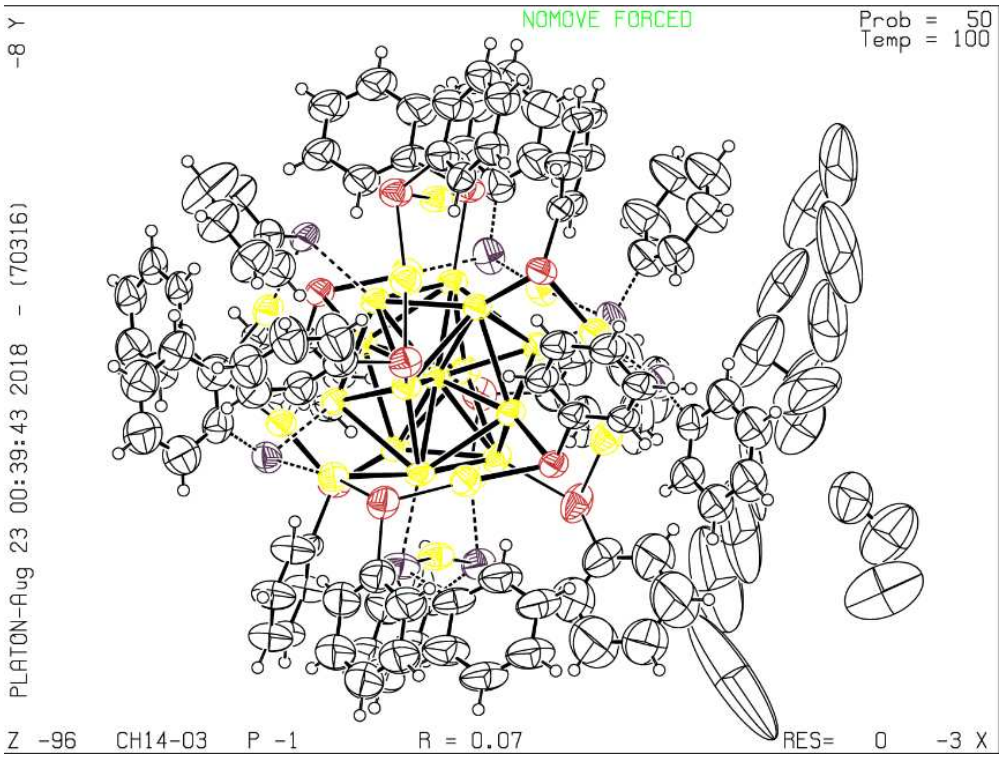


Figure A.16 ORTEP plot of crystal structure “CH14-03”.

APPENDIX B: SUPPLEMENTARY TO CHAPTER 3

B.1 General Methods

Tetrachloroaurate trihydrate (Sigma-Aldrich, ACS reagent, ≥49.0% Au basis), chloro(dimethylsulfide)gold(I) (TCI America, >97% Purity) tetra-*n*-octylammonium bromide (Acros Organics, 98% purity), sodium borohydride (Sigma-Aldrich, ≥98.0% purity), 2-phenylethanethiol (Sigma-Aldrich, ≥99% Purity), phenylacetylene (Alfa Aesar, 98+% Purity), lithium phenylacetylide (Sigma-Aldrich, 1.0M in THF), tetrahydrofuran (Fisher Scientific, certified, stabilized with 0.025% butylated hydroxytoluene), dichloromethane (Sigma-Aldrich, ACS grade, ≥99.5%, stabilized with 40-150 ppm amylene), methanol (Fisher Scientific, certified ACS, 99.9% assay), acetone (Industrial Chemical Corporation), chloroform (EMD Millipore, ≥99.8% assay, stabilized with ethanol), ethanol (Pharmaco-Aaper, 200 proof), and *trans*-2-[3-(4-*tert*-Butylphenyl)-2-methyl-2-propenyliden]malononitrile (Sigma Aldrich, ≥99.0% [HPLC]) were all used without further purification. Triethylamine (Fisher, ≥99.0%), pyridine (Fisher, ≥99.0%), and diethyl ether (Fisher, ≥99.0%, BHT stabilized) were purified using a SG Water USA glass contour solvent system prior to use. Water was obtained using a Thermo Scientific Barnstead Nanopure set to 18.2 MΩ·cm.

B.2 MALDI-MS Data Collection

2 mg *trans*-2-[3-(4-*tert*-Butylphenyl)-2-methyl-2-propenylidene]malononitrile was dissolved in 0.2 mL dichloromethane. To this solution was added 2.0 μL of nanocluster sample dissolved in dichloromethane. 0.2 μL of the combined solution was spotted on a

metal plate for MALDI-MS and allowed to dry for upwards of one hour. Data was collected using a Bruker Microflex LFR MALDI-TOF.

B.3 Synthesis of $Au_{25}(PET)_{18}TOA$

A previously published method was adapted for the synthesis of $Au_{25}(PET)_{18}TOA$.[172] In brief, 2.0 g $HAuCl_4 \cdot 3H_2O$ and 3.12 g tetra-*n*-octylammonium bromide were added to 140 mL tetrahydrofuran in a 300 mL round bottom flask. The solution was stirred for 30 minutes until a dark orange color was observed. 3.6 mL of 2-phenylethanethiol was then added to flask, and the resulting solution was stirred overnight. A separate solution containing 1.94 g sodium borohydride and 48 mL H_2O was produced in a 125 mL Erlenmeyer flask. This solution was cooled to 0 ^oC prior to adding it to the gold-containing solution. The combined solutions were then stirred for 48 hours, followed by separation and evaporation of the organic layer. The resulting brown oil was redissolved in several milliliters of dichloromethane and separated into four 50 mL conical vials. The conical vials were filled with methanol and placed in a centrifuge at 4000 RPM for 30 minutes. The supernatant was decanted and the precipitate was washed twice more by addition of methanol and centrifugation. The final product was extracted from the resulting powder using dichloromethane and evaporated to dryness.

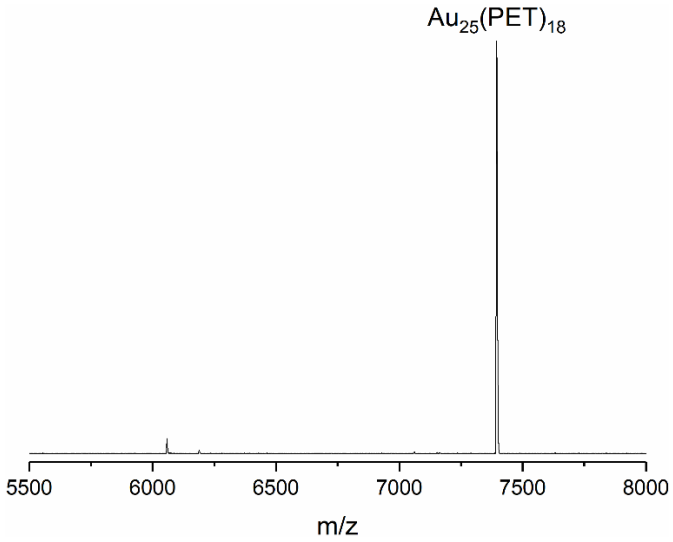


Figure B.1 Positive MALDI-MS spectrum of $Au_{25}(PET)_{18}TOA$.

B.4 Synthesis of Gold(I)-Phenylacetylide

Synthesis conditions were utilized from a previously published report.[122] In brief, 100 mg chloro(dimethylsulfide)gold(I) was added to 10.0 mL dichloromethane, 47.8 µL phenylacetylene, and 60.3 µL triethylamine in a 20 mL scintillation vial and stirred in the dark for two hours. The solution was then evaporated to approximate dryness and the resulting powder was washed with excess water, ethanol, and diethyl ether.

B.5 Acetylide Exchange Reactions on $Au_{25}(PET)_{18}TOA$

Ligand exchange was performed on $Au_{25}(PET)_{18}TOA$ by adding 12.0 mg (1.53 µmol) $Au_{25}(PET)_{18}TOA$ to 3.03 mL dichloromethane in a 20 mL scintillation vial at room temperature. 0.450 mg (1.53 µmol) gold(I)-phenylacetylide was added to the solution containing the Au_{25} cluster and stirred for 30 minutes, after which the solvent was evaporated. The crude product was then extracted using dichloromethane to remove any remaining gold(I)-phenylacetylide and evaporated to dryness.

A similar procedure was used to generate a higher amount of ligand exchange but using 4.50 mg (15.3 µmol) or 450 mg (153 µmol) of gold(I)-phenylacetylide.

B.6 Exchange of Lithium Phenylacetylide with $Au_{25}(PET)_{18}$

Ligand exchange was performed by purging a sealed 20 mL scintillation vial containing 20.0 mg (2.54 μmol) $Au_{25}(PET)_{18}$TOA and a stir bar with argon for 30 minutes. To this vial was added 25.4 μL (25.4 μmol) lithiu phenylacetylide. The solution was stirred for 30 minutes under argon at room temperature, after which a 2.0 μL aliquot of the solution was removed for MALDI-MS analysis.

B.7 Synthesis of $Au_{44}(PA)_{28}$

$Au_{44}(PA)_{28}$ was synthesized according a previously published report.[51] In brief, 44.7 mg gold(I)-phenylacetylide was added to 4.0 mL chloroform and stirred. A solution of 0.95 mg sodium borohydride in 1.0 mL was prepared and added to the solution containing gold(I)-phenylacetylide. The combined solutions were stirred in the dark for 16 hours. Afterwards, 0.3 mL phenylacetylene and 0.3 mL pyridine were added and stirred for 24 hours in the dark. The solution was subsequently evaporated to near dryness and washed with 15 mL hexanes to afford a dark powder. This powder was purified by size exclusion chromatography to afford the purified product.

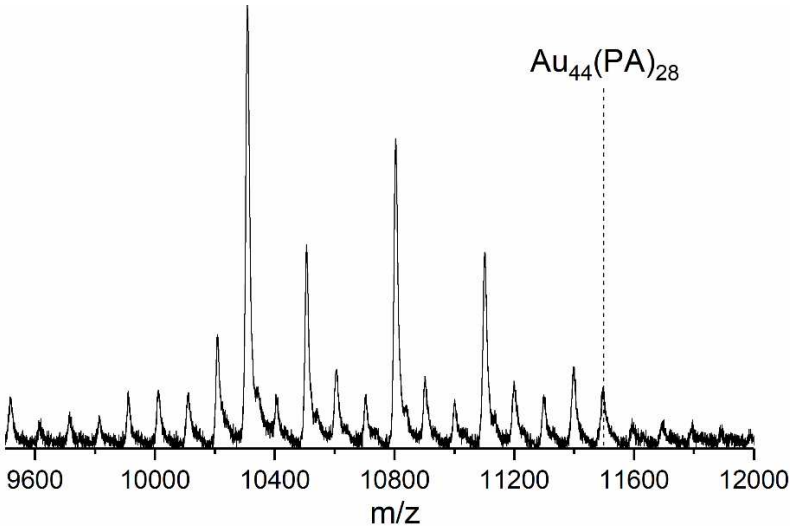


Figure B.2 Positive ion MALDI-MS of $Au_{44}(PA)_{28}$. The peak corresponding to $Au_{44}(PA)_{28}$ is labeled. All other peaks correspond to fragments or adducts of $Au_{44}(PA)_{28}$.

B.8 Thiolate Ligand Exchange on $Au_{44}(PA)_{28}$.

1.16 mg (0.148 μmol) $Au_{25}(PET)_{18}TOA$ and 1.70 mg (0.148 μmol) $Au_{44}(PA)_{28}$ were combined in 0.29 mL dichloromethane and stirred for five minutes. The solution was then evaporated to dryness.

B.9 Mass Spectrometry Results

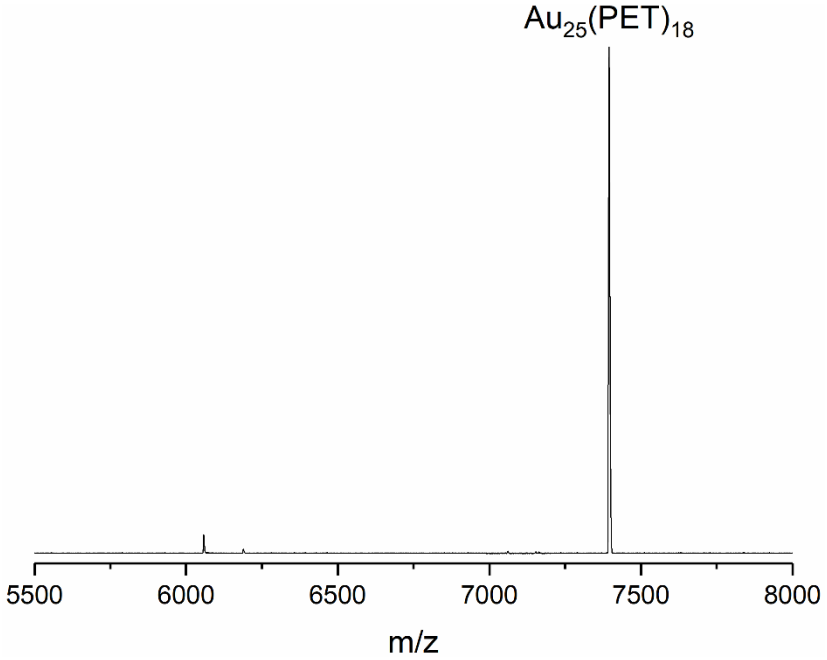


Figure B.3 Positive ion MALDI-MS of $Au_{25}(PET)_{18}$. The peak corresponding to this compound is labelled. Other peaks correspond to fragmentation products.

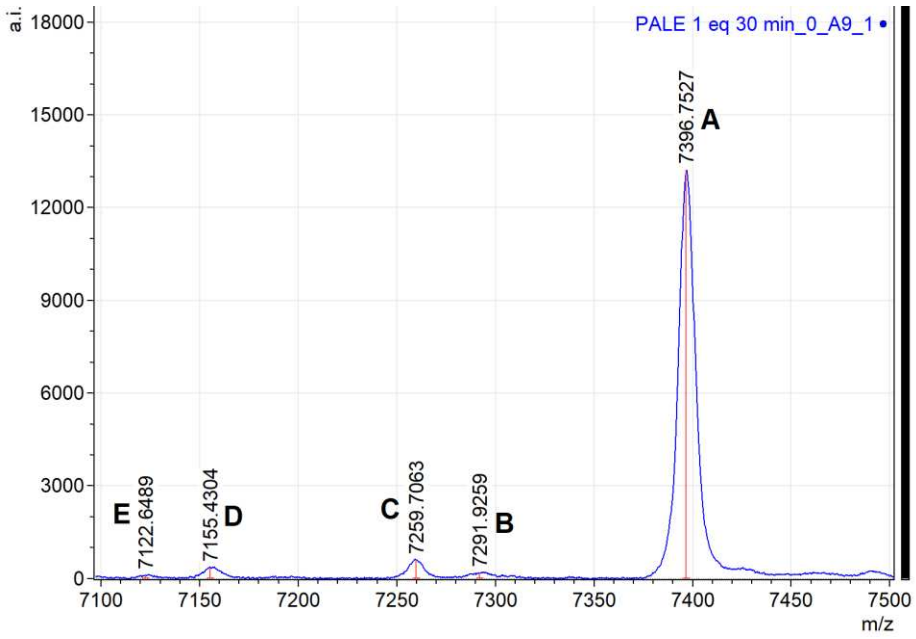


Figure B.4 Positive ion MALDI-MS spectrum after mixing $Au_{25}(PET)_{18}$ with 1 eq. phenylacetylene in DCM for 30 minutes. The peaks are labelled as the following species: A) $Au_{25}(PET)_{18}$ B) $Au_{25}(PET)_{17}S_1$ C) $Au_{25}(PET)_{17}$ D) $Au_{25}(PET)_{16}S_1$ E) $Au_{25}(PET)_{16}$

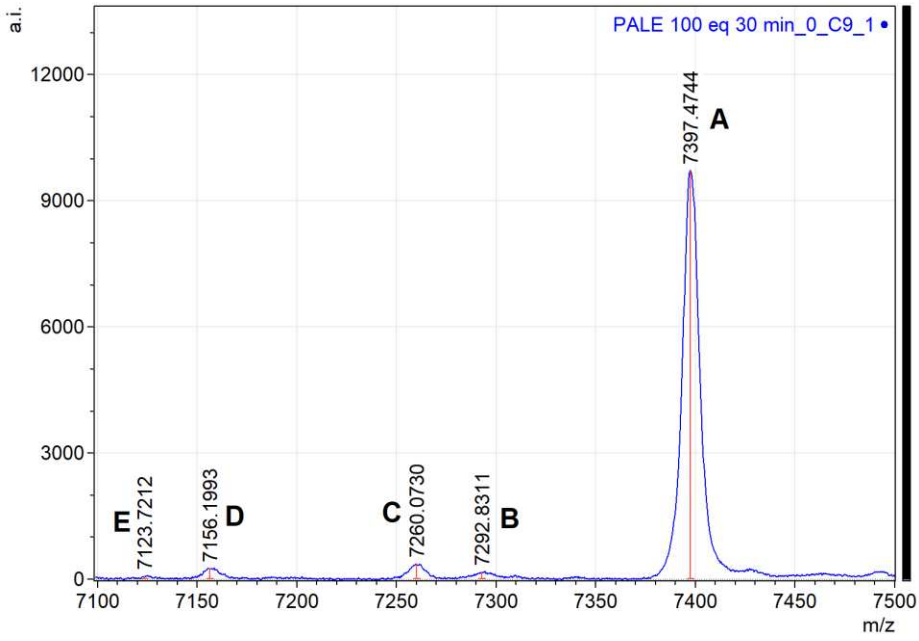


Figure B.5 Positive ion MALDI-MS spectrum after mixing $Au_{25}(PET)_{18}$ with 100 eq. phenylacetylene in DCM for 30 minutes. The peaks are labelled as the following species: A) $Au_{25}(PET)_{18}$ B) $Au_{25}(PET)_{17}S_1$ C) $Au_{25}(PET)_{17}$ D) $Au_{25}(PET)_{16}S_1$ E) $Au_{25}(PET)_{16}$

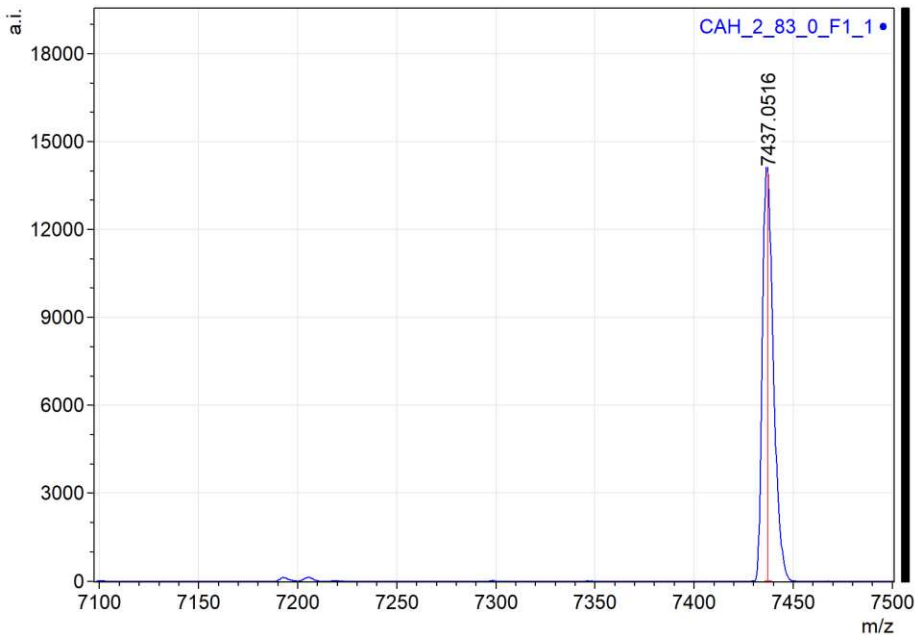


Figure B.6 Positive ion MALDI-MS spectrum after mixing $Au_{25}(PET)_{18}$ with 10 eq. phenylacetylene and 1 eq. triethylamine in DCM for 30 minutes. A sodium adduct of $Au_{25}(PET)_{18}$ is labelled. The calculated mass spectrometry result for $Au_{25}(PET)_{18}{\cdot}2Na^{+}$ is 7437.91 m/z.

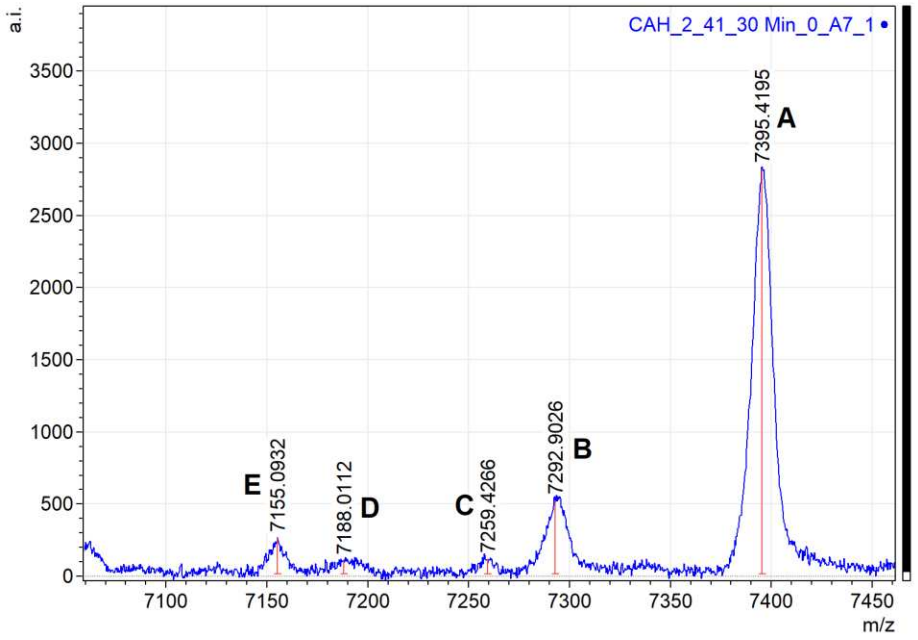


Figure B.7 Positive ion MALDI-MS spectrum after mixing $Au_{25}(PET)_{18}$ with 100 eq. phenylacetylene in toluene for 30 minutes at 60 °C. The peaks are labelled as the following species: A) $Au_{25}(PET)_{18}$ B) $Au_{25}(PET)_{17}S_1$ C) $Au_{25}(PET)_{17}$ D) $Au_{25}(PET)_{16}S_1$ E) $Au_{25}(PET)_{16}$.

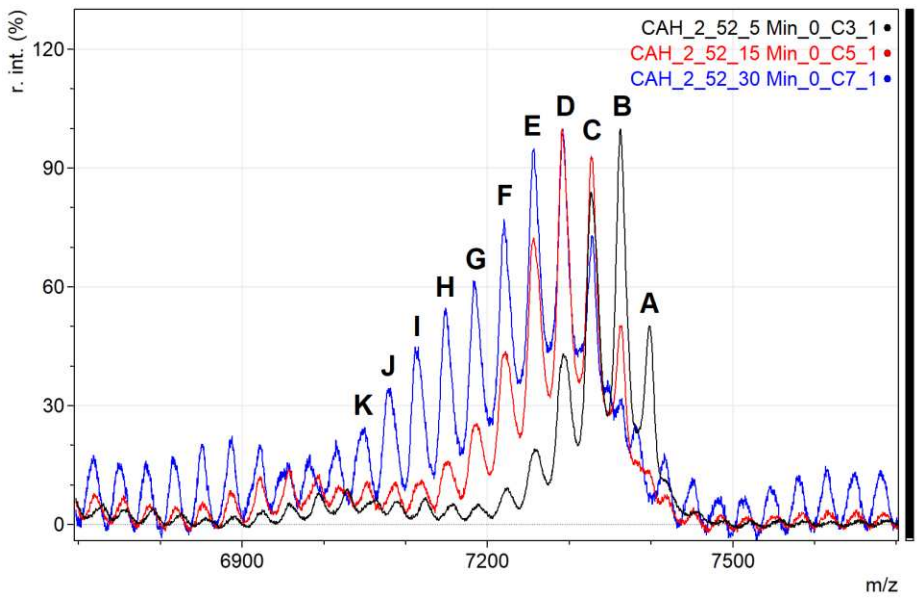


Figure B.8 Normalized positive ion MALDI-MS spetra after mixing $Au_{25}(PET)_{18}$ with 10 eq. gold(I)-phenylacetylide in THF for 5 minutes (black), 15 minutes (red), and 30 minutes (blue). The peaks are labelled as the following species: A) $Au_{25}(PET)_{18}$ B) $Au_{25}(PET)_{17}(PA)_1$ C) $Au_{25}(PET)_{16}(PA)_2$ D) $Au_{25}(PET)_{15}(PA)_3$ E) $Au_{25}(PET)_{14}(PA)_4$ F) $Au_{25}(PET)_{13}(PA)_5$ G) $Au_{25}(PET)_{12}(PA)_6$ H) $Au_{25}(PET)_{11}(PA)_7$ I) $Au_{25}(PET)_{10}(PA)_8$ J) $Au_{25}(PET)_9(PA)_9$ K) $Au_{25}(PET)_8(PA)_{10}$

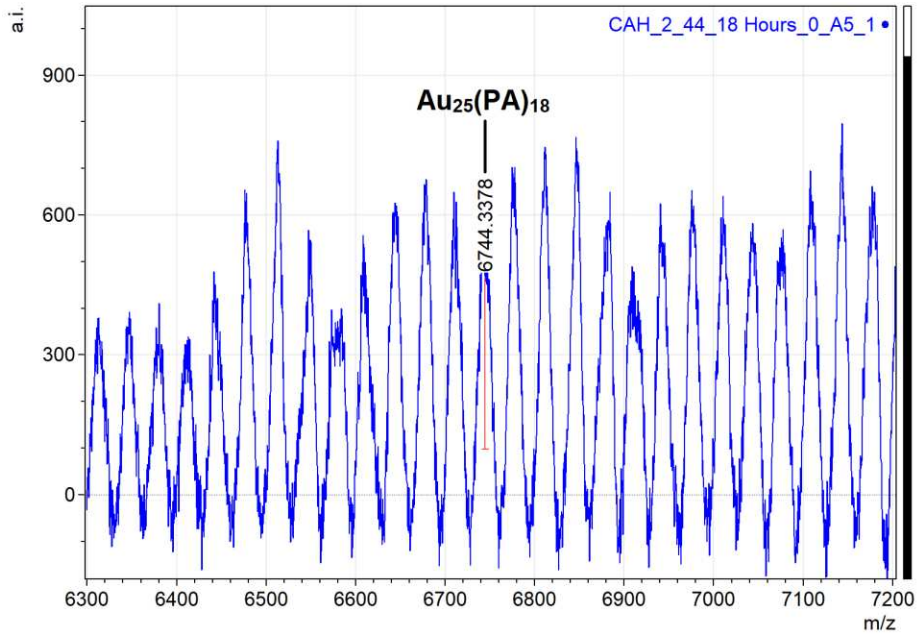


Figure B.9 Positive ion MALDI-MS spectrum after mixing $Au_{25}(PET)_{18}$ with 100 eq. gold(I)-phenylacetylide in DCM for 18 hours. The peak corresponding to the mass of $Au_{25}(PA)_{18}$ is labelled.

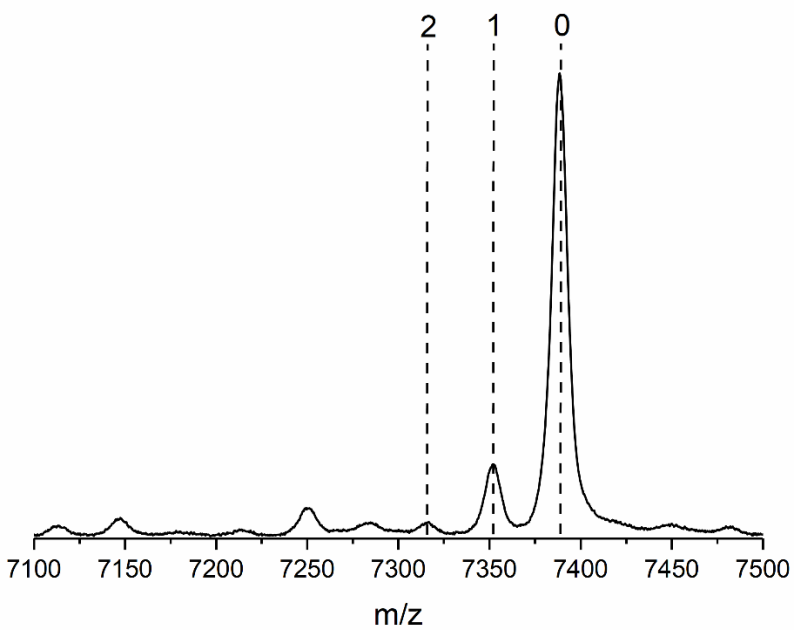


Figure B.10 Positive ion MALDI-MS spectrum of $Au_{25}(PET)_{18-x}(PA)_x$ obtained after mixing $Au_{25}(PET)_{18}$ with 10 eq. of lithium phenylacetylide in DCM under argon for 5 minutes. Other peaks correspond to fragmentation products.

APPENDIX C: SUPPLEMENTARY TO CHAPTER 4

C.1 General Methods

Tetrachloroaurate trihydrate (Sigma-Aldrich, ACS reagent, ≥49.0% Au basis), tetra-*n*-octylammonium bromide (Acros Organics, 98% purity), sodium borohydride (Sigma-Aldrich, ≥98.0% purity), 2-phenylethanethiol (Sigma-Aldrich, ≥99% Purity), tetrahydrofuran (Fisher Scientific, certified, stabilized with 0.025% butylated hydroxytoluene), methanol (Fisher Scientific, certified ACS, 99.9% assay), toluene (Sigma-Aldrich, ≥99.5% Purity), dichloromethane (Sigma Aldrich, ≥99.5%, 40-150 ppm amylene), dimethyl sulfide (Sigma Aldrich, ≥99.0%, anhydrous), diphenyl sulfide (Sigma Aldrich, 98%) *tert*-butyl sulfide (Combi-Blocks, 98.0%), tetrahydrothiophene (Sigma Aldrich, 99%), and *trans*-2-[3-(4-*tert*-Butylphenyl)-2-methyl-2-propenylidene]malononitrile (Sigma Aldrich, ≥99.0% [HPLC]) were all used without further purification. Water was obtained using a Thermo Scientific Barnstead Nanopure set to 18.2 MΩ·cm.

C.2 Synthesis of $Au_{25}(PET)_{18}TOA$

This procedure was adapted from a previously published report.[172] In brief, 2.0 g $HAuCl_4 \cdot 3H_2O$ and 3.12 g tetra-*n*-octylammonium bromide were added to 140 mL tetrahydrofuran in a 300 mL round bottom flask. The solution was stirred for 30 minutes until a dark orange color was observed. 3.6 mL of 2-phenylethanethiol was then added to flask, and the resulting solution was stirred overnight. A separate solution containing 1.94 g sodium borohydride and 48 mL H_2O was produced in a 125 mL Erlenmeyer flask. This solution was cooled to 0 °C prior to adding it to the gold-containing solution. The combined solutions were then stirred for 48 hours, followed by separation and evaporation of the

organic layer. The resulting brown oil was redissolved in several milliliters of dichloromethane and separated into four 50 mL conical vials. The conical vials were filled with methanol and placed in a centrifuge at 4000 RPM for 30 minutes. The supernatant was decanted and the precipitate was washed twice more by addition of methanol and centrifugation. Extraction with dichloromethane and subsequent evaporation of the solvent afforded the final product.

C.3 Reaction Between $Au_{25}(PET)_{18}TOA$ and Thioethers.

A generalized procedure was utilized for all reactions between $Au_{25}(PET)_{18}TOA$ and dimethyl sulfide, diphenyl sulfide, *tert*-butyl sulfide, and tetrahydrothiophene. 6.0 mg $Au_{25}(PET)_{18}TOA$ was added to 1.51 mL of a thioether solvent and stirred for upwards of 16 hours.

C.4 MALDI-MS Data Collection

2 mg *trans*-2-[3-(4-*tert*-Butylphenyl)-2-methyl-2-propenylidene]malononitrile was dissolved in 0.2 mL dichloromethane. To this solution was added 2.0 µL of nanocluster sample dissolved in dichloromethane. 0.2 µL of the combined solution was spotted on a metal plate for MALDI-MS and allowed to dry for one hour. Data was collected using a Bruker Microflex LFR MALDI-TOF.

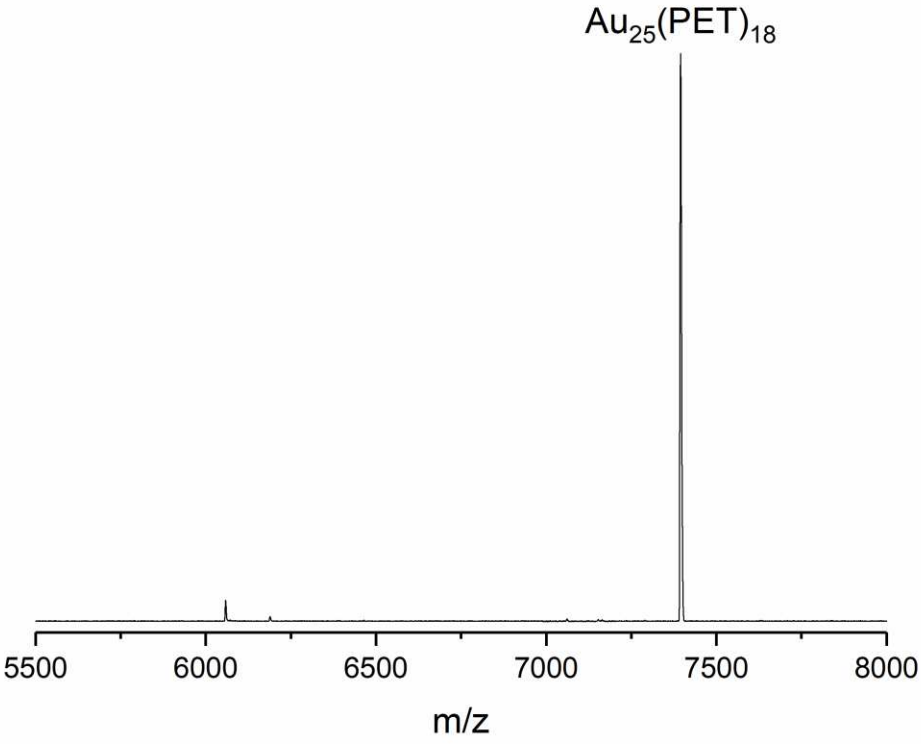


Figure C.1 Positive MALD-MS spectrum of $Au_{25}(PET)_{18}$. Unlabeled peaks correspond to fragmentations of the parent compound.

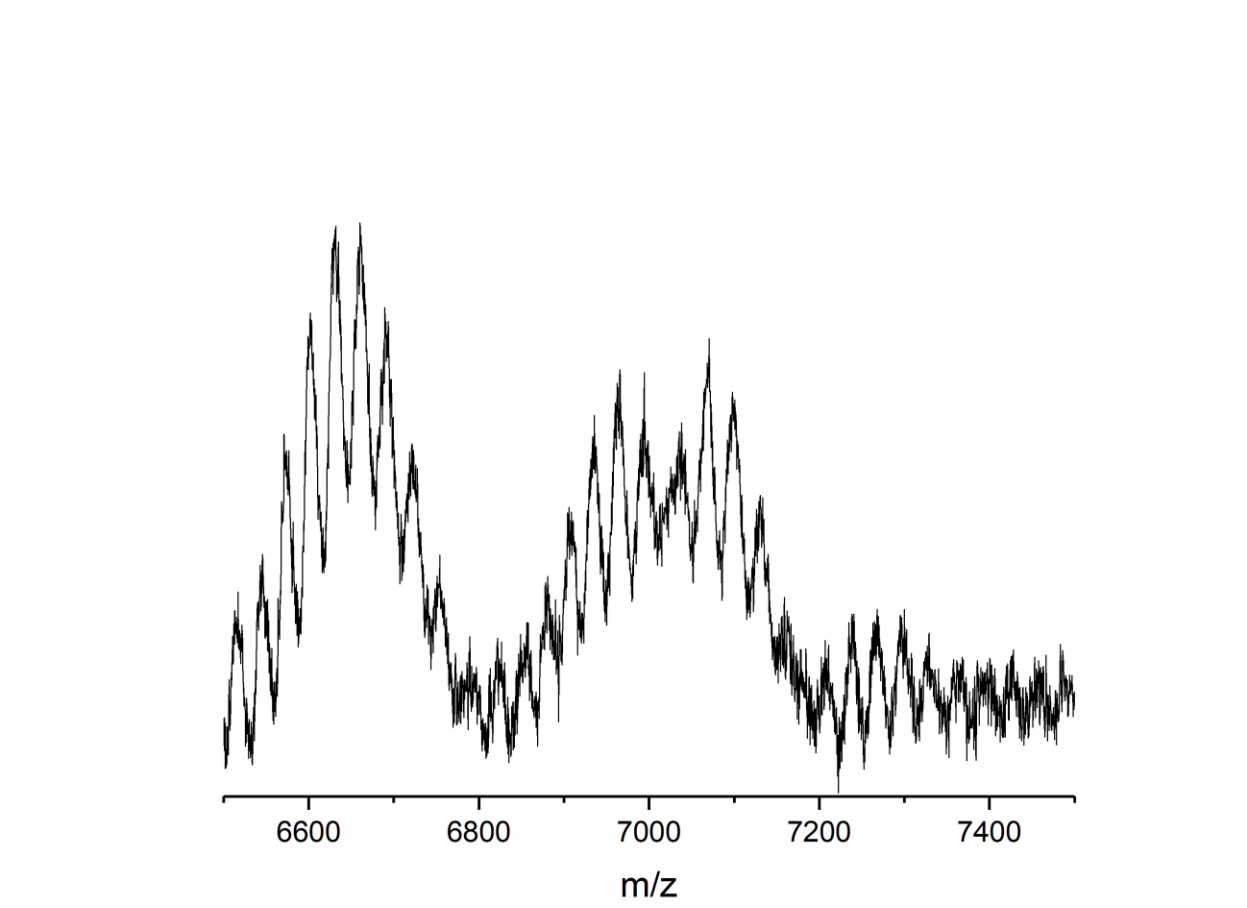


Figure C.2 Positive MALDI-MS after stirring $Au_{25}(PET)_{18}$ in diphenyl sulfide for 16 hours.

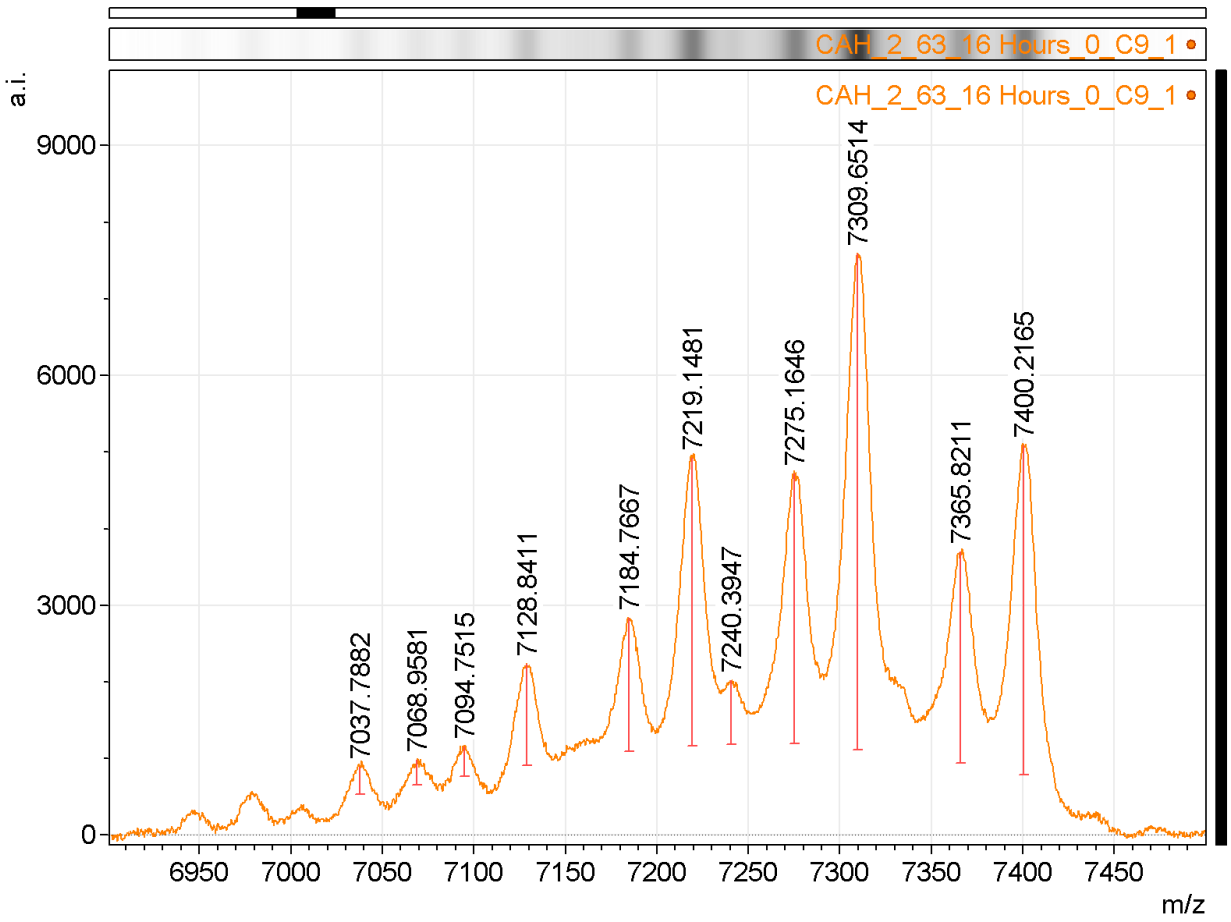


Figure C.3 Positive MALDI-MS after stirring $Au_{25}(PET)_{18}$ in THT for 16 hours.

APPENDIX D: SUPPLEMENTARY TO CHAPTER 5

D.1 General Methods

Tetrachloroaurate trihydrate (Sigma-Aldrich, ACS reagent, ≥49.0% Au basis), tetra-*n*-octylammonium bromide (Acros Organics, 98% purity), sodium borohydride (Sigma-Aldrich, ≥98.0% purity), 2-phenylethanethiol (Sigma-Aldrich, ≥99% Purity), tetrahydrofuran (Fisher Scientific, certified, stabilized with 0.025% butylated hydroxytoluene), methanol (Fisher Scientific, certified ACS, 99.9% assay), toluene (Sigma-Aldrich, ≥99.5% Purity), acetonitrile-D3 (Cambridge Isotope Laboratories, 99.8% D), and *trans*-2-[3-(4-*tert*-Butylphenyl)-2-methyl-2-propenyliden]malononitrile (Sigma Aldrich, ≥99.0% [HPLC]) were all used without further purification. Water was obtained using a Thermo Scientific Barnstead Nanopure set to 18.2 MΩ·cm.

D.2 Synthesis of $Au_{25}(PET)_{18}TOA$

This procedure was adapted from a previously published report.[172] In brief, 2.0 g $HAuCl_4 \cdot 3H_2O$ and 3.12 g tetra-*n*-octylammonium bromide were added to 140 mL tetrahydrofuran in a 300 mL round bottom flask. The solution was stirred for 30 minutes until a dark orange color was observed. 3.6 mL of 2-phenylethanethiol was then added to flask, and the resulting solution was stirred overnight. A separate solution containing 1.94 g sodium borohydride and 48 mL H_2O was produced in a 125 mL Erlenmeyer flask. This solution was cooled to 0 ^oC prior to adding it to the gold-containing solution. The combined solutions were then stirred for 48 hours, followed by separation and evaporation of the organic layer. The resulting brown oil was redissolved in several milliliters of dichloromethane and separated into four 50 mL conical vials. The conical vials were filled

with methanol and placed in a centrifuge at 4000 RPM for 30 minutes. The supernatant was decanted and the precipitate was washed twice more by addition of methanol and centrifugation. Extraction with dichloromethane and subsequent evaporation of the solvent afforded the final product.

D.3 Crystallization of Cuboid $Au_{25}(PET)_{18}^{0}$ Crystals

$Au_{25}(PET)_{18}TOA$ was dissolved in a minimal amount of toluene. To this solution was added tetra-*n*-octylammonium bromide in a 1:1 mass ratio to $Au_{25}(PET)_{18}TOA$. Ethanol was added and mixed until the solution appeared slightly cloudly, after which the solution was centrifuged. The resulting supernatant was heated slightly on a hot plate at the lowest setting. During this time, the cluster oxidized. Cuboid crystals could be observed between thirty minutes and one week depending on the exact ratio of toluene and ethanol.

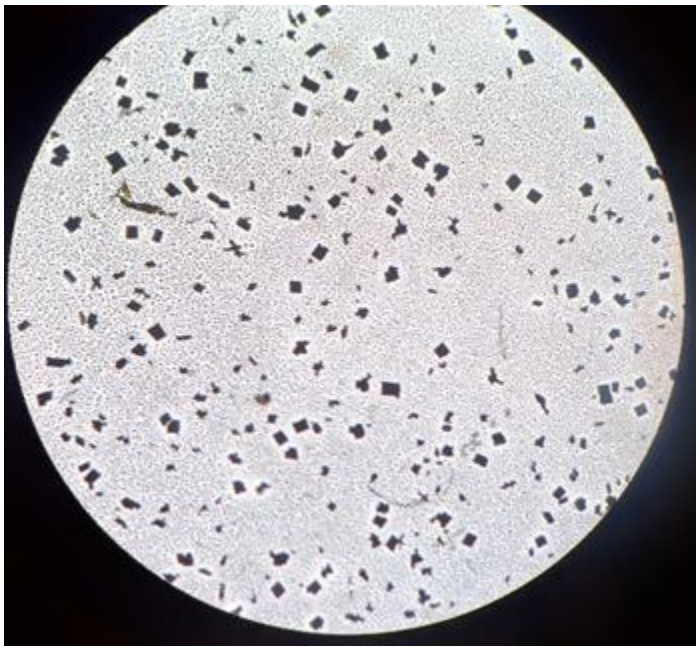


Figure D.1 Picture of cuboid crystals under a microscope.

D.4 Crystallization of Quadrilateral Prism $Au_{25}(PET)_{18}^0$ Crystals

Cuboid crystals of $Au_{25}(PET)_{18}^0$ were dissolved in a minimal amount of toluene. Ethanol was layered on top of the solution in approximately a 1:1 volume ratio to toluene and allowed to mix at room temperature. Prism crystals were observed within three days.

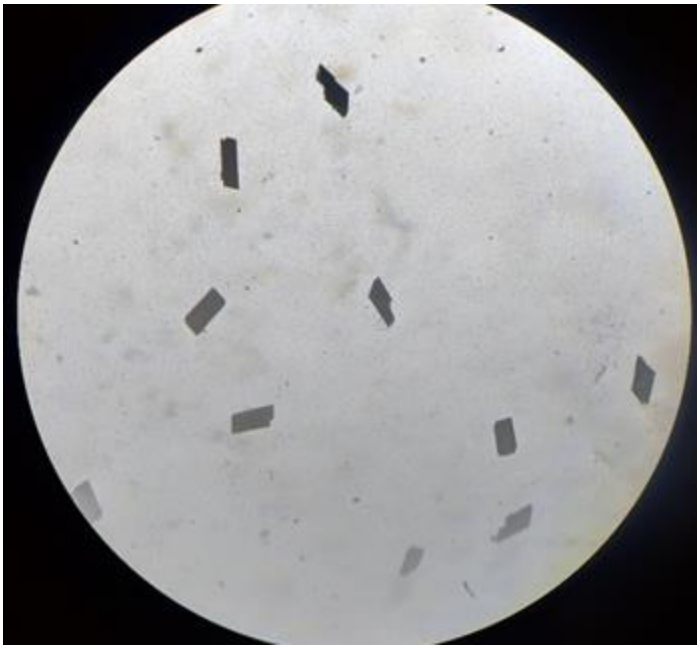


Figure D.2 Picture of quadrilateral prism crystals under a microscope.

D.5 Crystallization of Thin Platelet $Au_{25}(PET)_{18}^0$ Crystals

Cuboid crystals of $Au_{25}(PET)_{18}^0$ were dissolved in a minimal amount of deuterated acetonitrile in an NMR tube. To this solution, tetramethylsilane was added in a 1:1000 volume ratio to deuterated acetonitrile. Thin platelet crystals were observed within one day.



Figure D.3 Picture of thin platelet crystals under a microscope.

D.6 Crystallization of Needle $Au_{25}(PET)_{18}^{0}$ Crystals

Amorphous $Au_{25}(PET)_{18}$ powder was dissolved in a minimal amount of toluene. Ethanol was added and mixed until the solution appeared slightly cloudly. Crystals could be observed after approximately one month.

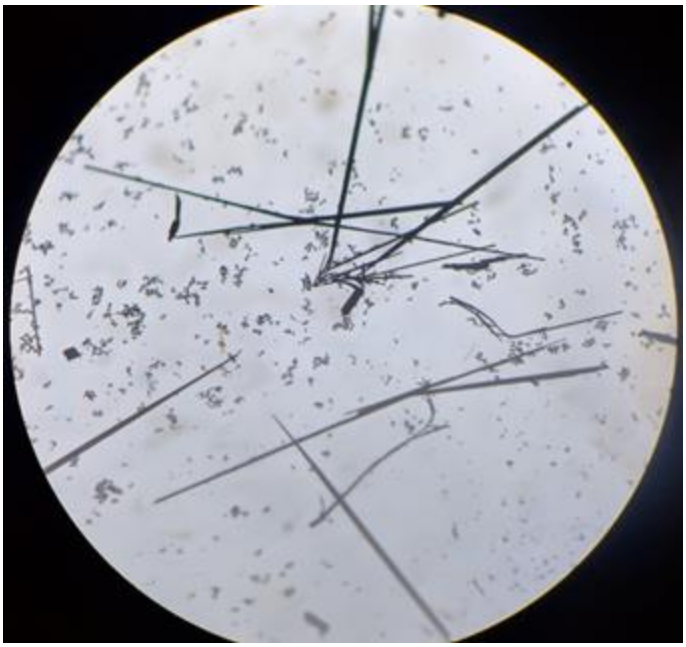


Figure D.4 Picture of needle crystals under a microscope.

D.7 Single Crystal X-ray Diffraction Data Collection

Single crystal x-ray diffraction was performed using a XtaLAB Synergy Custom FR-X diffractometer set to a generator level of 1200 W (40 kV and 30 mA) and a Pilatus P200K 3R detector. Data was collected to a resolution of 0.84 Å using a copper irradiation source (1.54184 Å) with an exposure time of 0.5 seconds and detector distance of 28 mm. Data was processed using CrysAlis(Pro). Numerical and analytical absorption corrections were attempted but not utilized in the final structures as they did not improve statistical values. SHELXT was used for initial determination of the nanocluster. Further solving of the crystal structure was performed with a full-matrix least-squared against F^2 using SHELXL.

D.8 Solvent Accessibility Calculations

Values were obtained utilizing the PyMOL Molecular Graphics System (version 2.0, Schrödinger LLC) using a dot density of 4 and a probe radius of 1.8 corresponding to the

van der Waals radius of sulfur. Solvent accessibility values for all connected gold atoms were summed to provide the solvent accessibility values listed for each ligand.

D.9 MALDI-MS Data Collection

2 mg *trans*-2-[3-(4-*tert*-Butylphenyl)-2-methyl-2-propenylidene]malononitrile was dissolved in 0.2 mL dichloromethane. To this solution was added 2.0 µL of nanocluster sample dissolved in dichloromethane. 0.2 µL of the combined solution was spotted on a metal plate for MALDI-MS and allowed to dry for one hour. Data was collected using a Bruker Microflex LFR MALDI-TOF.

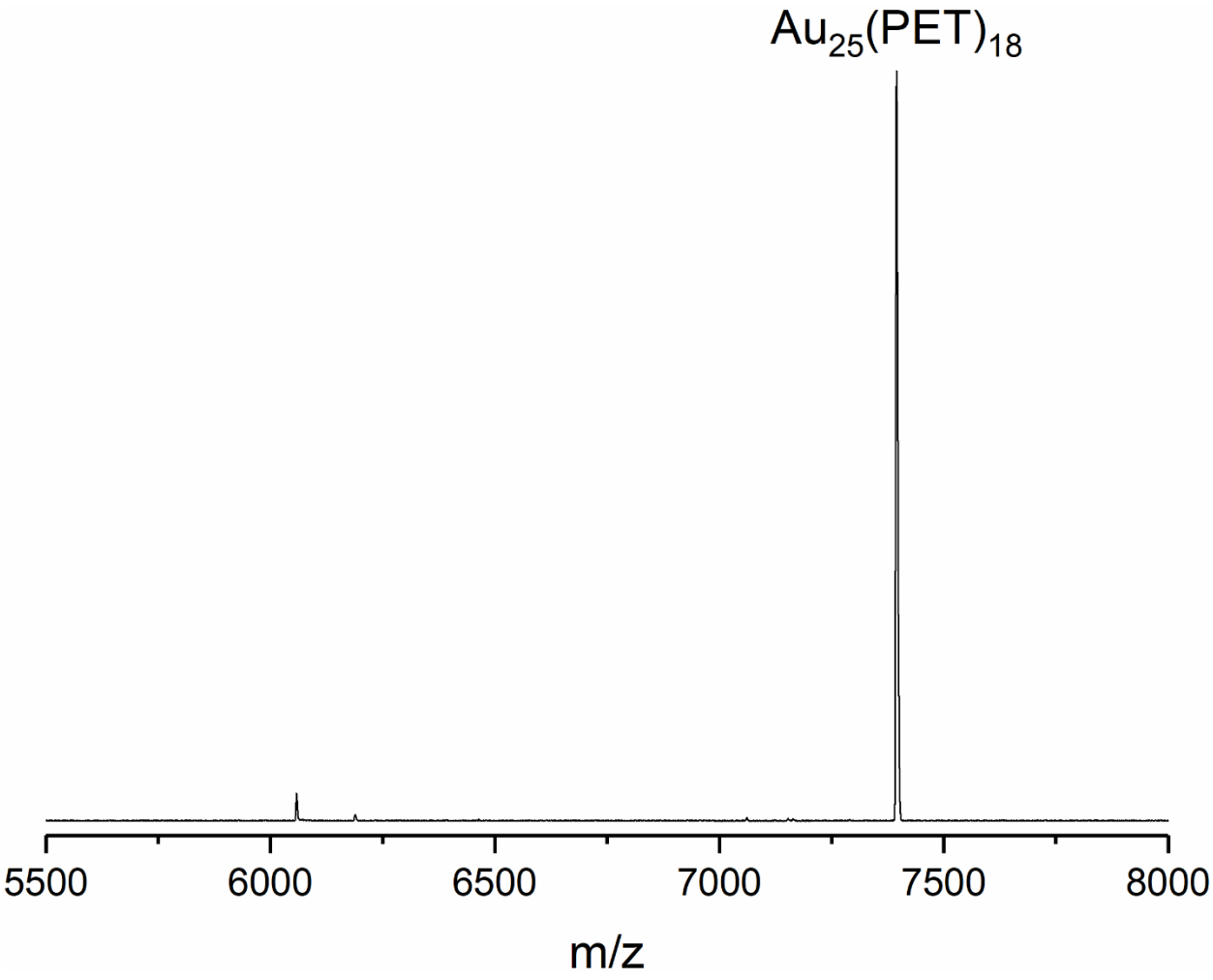


Figure D.5 Positive MALDI-MS spectrum of $Au_{25}(PET)_{18}TOA$.

D.10 Summary of Crystal Structure Results

Identification name	Cuboid	Quadrilateral Prism
Empirical formula	$C_{144}H_{162}Au_{25}S_{18}$	$C_{158}H_{178}Au_{25}S_{18}$
Formula weight	7394.00	7578.24
Habit	Needle	Quadrilateral Prism
Color	Black	Black
Temperature (K)	100	100
Wavelength (Å)	1.54184	1.54184
Crystal system	Orthorhombic	Triclinic
Space group	Pccn	P-1
a (Å)	14.1500	16.1600
b (Å)	20.4765	17.7086
c (Å)	27.8912	17.7130
α	95.851	65.113
β	94.521	81.430
γ	105.762	64.761
Volume (Å^3)	7689	4156.42
Z	1	1
Independent reflections	25097	14572
R(F) (I>2σ(I))	0.0272	0.0266
wR(F2) (all data)	0.0693	0.0666
GooF [all data]	1.116	1.039
min., max. e- dens. (e Å3)	1.825, -2.304	2.03, -1.969

Identification name	Thin Platelet	Needle
Empirical formula	$C_{144}H_{162}Au_{25}S_{18}$	$C_{144}H_{162}Au_{25}S_{18}$
Formula weight	7394.00	7394.00
Habit	Platelet	Needle
Color	Black	Black
Temperature (K)	100	100
Wavelength (Å)	1.54184	1.54184
Crystal system	Triclinic	Triclinic
Space group	P-1	P-1
a (Å)	15.0644	14.1500

b (Å)	15.2436	20.4765
c (Å)	20.2268	27.8912
α	111.378	95.851
β	93.424	94.521
γ	112.469	105.762
Volume (Å^3)	3888	7689
Z	1	2
Independent reflections	13710	26913
R(F) (I>2σ(I))	0.0242	0.0272
wR(F2) (all data)	0.0626	0.0693
GooF [all data]	1.113	1.116
min., max. e- dens. (e Å3)	1.361, -1.832	1.825, -2.304

D.11 Crystallographic Information File for $Au_{25}(PET)_{18}^0$ Cuboid Sample

```
data_PLO_12_Manual

_audit_creation_method           'SHELXL-2014/7'
_shelx_SHELXL_version_number     '2014/7'
_chemical_name_systematic        ?
_chemical_name_common            ?
_chemical_melting_point          ?
_chemical_formula_moiety         ?
_chemical_formula_sum
 'C144 H162 Au25 S18'
_chemical_formula_weight         7393.97

loop_
 _atom_type_symbol
 _atom_type_description
 _atom_type_scat_dispersion_real
 _atom_type_scat_dispersion_imag
 _atom_type_scat_source
'C'  'C'   0.0181   0.0091
 'International Tables Vol C Tables 4.2.6.8 and 6.1.1.4'
'H'  'H'   0.0000   0.0000
 'International Tables Vol C Tables 4.2.6.8 and 6.1.1.4'
'Au'  'Au'  -4.4197   7.2980
 'International Tables Vol C Tables 4.2.6.8 and 6.1.1.4'
'S'  'S'   0.3331   0.5567
 'International Tables Vol C Tables 4.2.6.8 and 6.1.1.4'
```

```
_space_group_crystal_system       orthorhombic
_space_group_IT_number            56
_space_group_name_H-M_alt         'P c c n'
_space_group_name_Hall            '-P 2ab 2ac'

_shelx_space_group_comment
;
The symmetry employed for this shelxl refinement is uniquely defined
by the following loop, which should always be used as a source of
symmetry information in preference to the above space-group names.
They are only intended as comments.
;

loop_
 _space_group_symop_operation_xyz
 'x, y, z'
 '-x+1/2, -y+1/2, z'
 '-x, y+1/2, -z+1/2'
 'x+1/2, -y, -z+1/2'
 '-x, -y, -z'
 'x-1/2, y-1/2, -z'
 'x, -y-1/2, z-1/2'
 '-x-1/2, y, z-1/2'

_cell_length_a                    31.2303(3)
_cell_length_b                    26.9497(3)
_cell_length_c                    18.5175(2)
_cell_angle_alpha                   90
_cell_angle_beta                  90
_cell_angle_gamma                    90
_cell_volume                      15585.2(3)
_cell_formula_units_Z               4
_cell_measurement_temperature     293(2)
_cell_measurement_reflns_used     ?
_cell_measurement_theta_min       ?
_cell_measurement_theta_max       ?

_exptl_crystal_description        ?
_exptl_crystal_colour             ?
_exptl_crystal_density_meas       ?
_exptl_crystal_density_method     ?
_exptl_crystal_density_diffrn     3.151
_exptl_crystal_F_000              13156
_exptl_transmission_factor_min    ?
_exptl_transmission_factor_max    ?
_exptl_crystal_size_max           ?
```

```
_exptl_crystal_size_mid          ?
_exptl_crystal_size_min          ?
_exptl_absorpt_coefficient_mu    45.556
_shelx_estimated_absorpt_T_min   ?
_shelx_estimated_absorpt_T_max   ?
_exptl_absorpt_correction_type   ?
_exptl_absorpt_correction_T_min  ?
_exptl_absorpt_correction_T_max  ?
_exptl_absorpt_process_details   ?
_exptl_absorpt_special_details   ?
_diffrn_ambient_temperature      293(2)
_diffrn_radiation_wavelength     1.54184
_diffrn_radiation_type           CuK\a
_diffrn_source                   ?
_diffrn_measurement_device_type  ?
_diffrn_measurement_method       ?
_diffrn_detector_area_resol_mean  ?
_diffrn_reflns_number            56038
_diffrn_reflns_av_unetI/netI     0.0491
_diffrn_reflns_av_R_equivalents  0.0621
_diffrn_reflns_limit_h_min       -22
_diffrn_reflns_limit_h_max       36
_diffrn_reflns_limit_k_min       -31
_diffrn_reflns_limit_k_max       32
_diffrn_reflns_limit_l_min       -21
_diffrn_reflns_limit_l_max       22
_diffrn_reflns_theta_min         4.553
_diffrn_reflns_theta_max         66.594
_diffrn_reflns_theta_full        66.594
_diffrn_measured_fraction_theta_max  0.994
_diffrn_measured_fraction_theta_full  0.994
_diffrn_reflns_Laue_measured_fraction_max  0.994
_diffrn_reflns_Laue_measured_fraction_full  0.994
_diffrn_reflns_point_group_measured_fraction_max  0.994
_diffrn_reflns_point_group_measured_fraction_full  0.994
_reflns_number_total             13691
_reflns_number_gt                11764
_reflns_threshold_expression     'I > 2\s(I)'
_reflns_Friedel_coverage         0.000
_reflns_Friedel_fraction_max     .
_reflns_Friedel_fraction_full    .

_reflns_special_details
;
 Reflections were merged by SHELXL according to the crystal
 class for the calculation of statistics and refinement.
```

_reflns_Friedel_fraction is defined as the number of unique
Friedel pairs measured divided by the number that would be
possible theoretically, ignoring centric projections and
systematic absences.
;

_computing_data_collection ?
_computing_cell_refinement ?
_computing_data_reduction ?
_computing_structure_solution ?
_computing_structure_refinement 'SHELXL-2014/7 (Sheldrick, 2014)'
_computing_molecular_graphics ?
_computing_publication_material ?
_refine_special_details ?
_refine_ls_structure_factor_coef Fsqd
_refine_ls_matrix_type full
_refine_ls_weighting_scheme calc
_refine_ls_weighting_details
'w=1/[\s^2^(Fo^2^)+(0.0566P)^2^+489.9061P] where P=(Fo^2^+2Fc^2^)/3'
_atom_sites_solution_primary ?
_atom_sites_solution_secondary ?
_atom_sites_solution_hydrogens geom
_refine_ls_hydrogen_treatment constr
_refine_ls_extinction_method none
_refine_ls_extinction_coef .
_refine_ls_number_reflns 13691
_refine_ls_number_parameters 856
_refine_ls_number_restraints 114
_refine_ls_R_factor_all 0.0572
_refine_ls_R_factor_gt 0.0487
_refine_ls_wR_factor_ref 0.1273
_refine_ls_wR_factor_gt 0.1223
_refine_ls_goodness_of_fit_ref 1.044
_refine_ls_restrained_S_all 1.040
_refine_ls_shift/su_max 0.001
_refine_ls_shift/su_mean 0.000

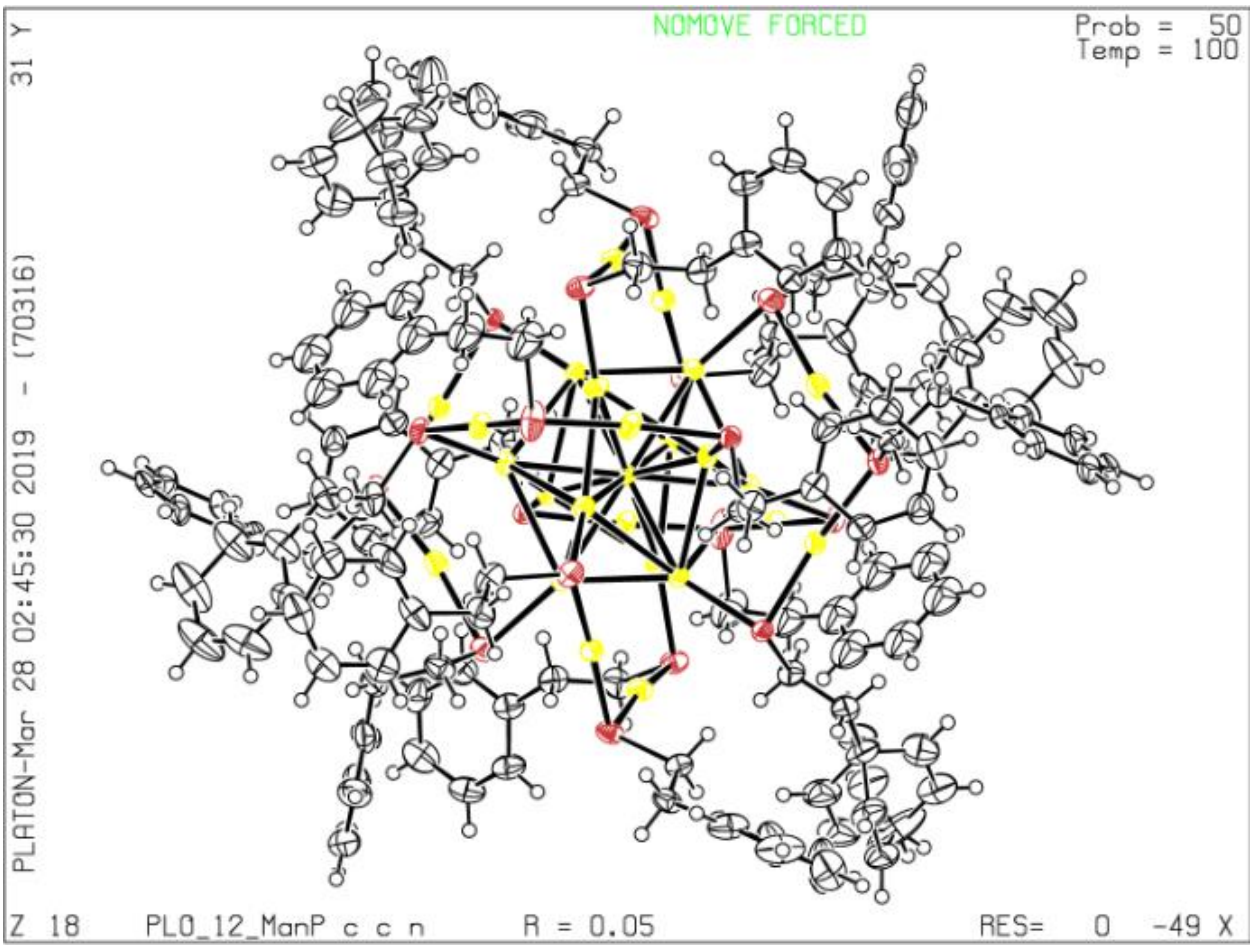


Figure D.6 ORTEP plot of $Au_{25}(PET)_{18}^{0}$ structure from a cuboid crystal

D.12 Crystallographic Information File for $Au_{25}(PET)_{18}$ Needle Sample

```
data_PLO-10_4_Manual

_audit_creation_method            'SHELXL-2014/7'
_shelx_SHELXL_version_number      '2014/7'
_chemical_name_systematic         ?
_chemical_name_common             ?
_chemical_melting_point           ?
_chemical_formula_moiety          ?
_chemical_formula_sum
 'C144 H162 Au25 S18'
_chemical_formula_weight          7393.97

loop_
 _atom_type_symbol
 _atom_type_description
 _atom_type_scat_dispersion_real
```

```
 _atom_type_scat_dispersion_imag
 _atom_type_scat_source
'C'  'C'   0.0181   0.0091
'International Tables Vol C Tables 4.2.6.8 and 6.1.1.4'
'H'  'H'   0.0000   0.0000
'International Tables Vol C Tables 4.2.6.8 and 6.1.1.4'
'Au'  'Au'  -4.4197   7.2980
'International Tables Vol C Tables 4.2.6.8 and 6.1.1.4'
'S'  'S'   0.3331   0.5567
'International Tables Vol C Tables 4.2.6.8 and 6.1.1.4'

_space_group_crystal_system      triclinic
_space_group_IT_number           2
_space_group_name_H-M_alt        'P -1'
_space_group_name_Hall           '-P 1'

_shelx_space_group_comment
;
The symmetry employed for this shelxl refinement is uniquely defined
by the following loop, which should always be used as a source of
symmetry information in preference to the above space-group names.
They are only intended as comments.
;

loop_
 _space_group_symop_operation_xyz
 'x, y, z'
 '-x, -y, -z'

_cell_length_a                 14.15000(10)
_cell_length_b                 20.4765(2)
_cell_length_c                 27.8912(2)
_cell_angle_alpha                95.8510(10)
_cell_angle_beta                 94.5210(10)
_cell_angle_gamma                  105.7620(10)
_cell_volume                   7688.84(12)
_cell_formula_units_Z            2
_cell_measurement_temperature    293(2)
_cell_measurement_reflns_used    ?
_cell_measurement_theta_min      ?
_cell_measurement_theta_max      ?

_exptl_crystal_description       ?
_exptl_crystal_colour            ?
_exptl_crystal_density_meas      ?
_exptl_crystal_density_method    ?
```

```
_exptl_crystal_density_diffrn    3.194
_exptl_crystal_F_000             6578
_exptl_transmission_factor_min   ?
_exptl_transmission_factor_max   ?
_exptl_crystal_size_max          ?
_exptl_crystal_size_mid          ?
_exptl_crystal_size_min          ?
_exptl_absorpt_coefficient_mu    46.171
_shelx_estimated_absorpt_T_min   ?
_shelx_estimated_absorpt_T_max   ?
_exptl_absorpt_correction_type   ?
_exptl_absorpt_correction_T_min  ?
_exptl_absorpt_correction_T_max  ?
_exptl_absorpt_process_details   ?
_exptl_absorpt_special_details   ?
_diffrn_ambient_temperature      293(2)
_diffrn_radiation_wavelength     1.54184
_diffrn_radiation_type           CuK\a
_diffrn_source                   ?
_diffrn_measurement_device_type  ?
_diffrn_measurement_method       ?
_diffrn_detector_area_resol_mean ?
_diffrn_reflns_number            97946
_diffrn_reflns_av_unetI/netI     0.0268
_diffrn_reflns_av_R_equivalents  0.0297
_diffrn_reflns_limit_h_min       -16
_diffrn_reflns_limit_h_max       16
_diffrn_reflns_limit_k_min       -24
_diffrn_reflns_limit_k_max       24
_diffrn_reflns_limit_l_min       -33
_diffrn_reflns_limit_l_max       33
_diffrn_reflns_theta_min         4.468
_diffrn_reflns_theta_max         66.599
_diffrn_reflns_theta_full        66.599
_diffrn_measured_fraction_theta_max  0.991
_diffrn_measured_fraction_theta_full 0.991
_diffrn_reflns_Laue_measured_fraction_max   0.991
_diffrn_reflns_Laue_measured_fraction_full  0.991
_diffrn_reflns_point_group_measured_fraction_max  0.991
_diffrn_reflns_point_group_measured_fraction_full 0.991
_reflns_number_total             26913
_reflns_number_gt                25097
_reflns_threshold_expression     'I > 2\s(I)'
_reflns_Friedel_coverage         0.000
_reflns_Friedel_fraction_max     .
_reflns_Friedel_fraction_full    .
```

```
_refIns_special_details
;
 Reflections were merged by SHELXL according to the crystal
 class for the calculation of statistics and refinement.

 _refIns_Friedel_fraction is defined as the number of unique
 Friedel pairs measured divided by the number that would be
 possible theoretically, ignoring centric projections and
 systematic absences.
;

_computing_data_collection        ?
_computing_cell_refinement        ?
_computing_data_reduction         ?
_computing_structure_solution     ?
_computing_structure_refinement 'SHELXL-2014/7 (Sheldrick, 2014)'
_computing_molecular_graphics     ?
_computing_publication_material   ?
_refine_special_details           ?
_refine_ls_structure_factor_coef  Fsqd
_refine_ls_matrix_type            full
_refine_ls_weighting_scheme       calc
_refine_ls_weighting_details
'w=1/[\s^2^(Fo^2^)+(0.0320P)^2^+49.0971P] where P=(Fo^2^+2Fc^2^)/3'
_atom_sites_solution_primary      ?
_atom_sites_solution_secondary    ?
_atom_sites_solution_hydrogens    geom
_refine_ls_hydrogen_treatment     constr
_refine_ls_extinction_method      none
_refine_ls_extinction_coef        .
_refine_ls_number_refIns          26913
_refine_ls_number_parameters      1684
_refine_ls_number_restraints      0
_refine_ls_R_factor_all           0.0299
_refine_ls_R_factor_gt            0.0272
_refine_ls_wR_factor_ref          0.0693
_refine_ls_wR_factor_gt           0.0681
_refine_ls_goodness_of_fit_ref    1.116
_refine_ls_restrained_S_all       1.116
_refine_ls_shift/su_max           0.012
_refine_ls_shift/su_mean          0.002
```

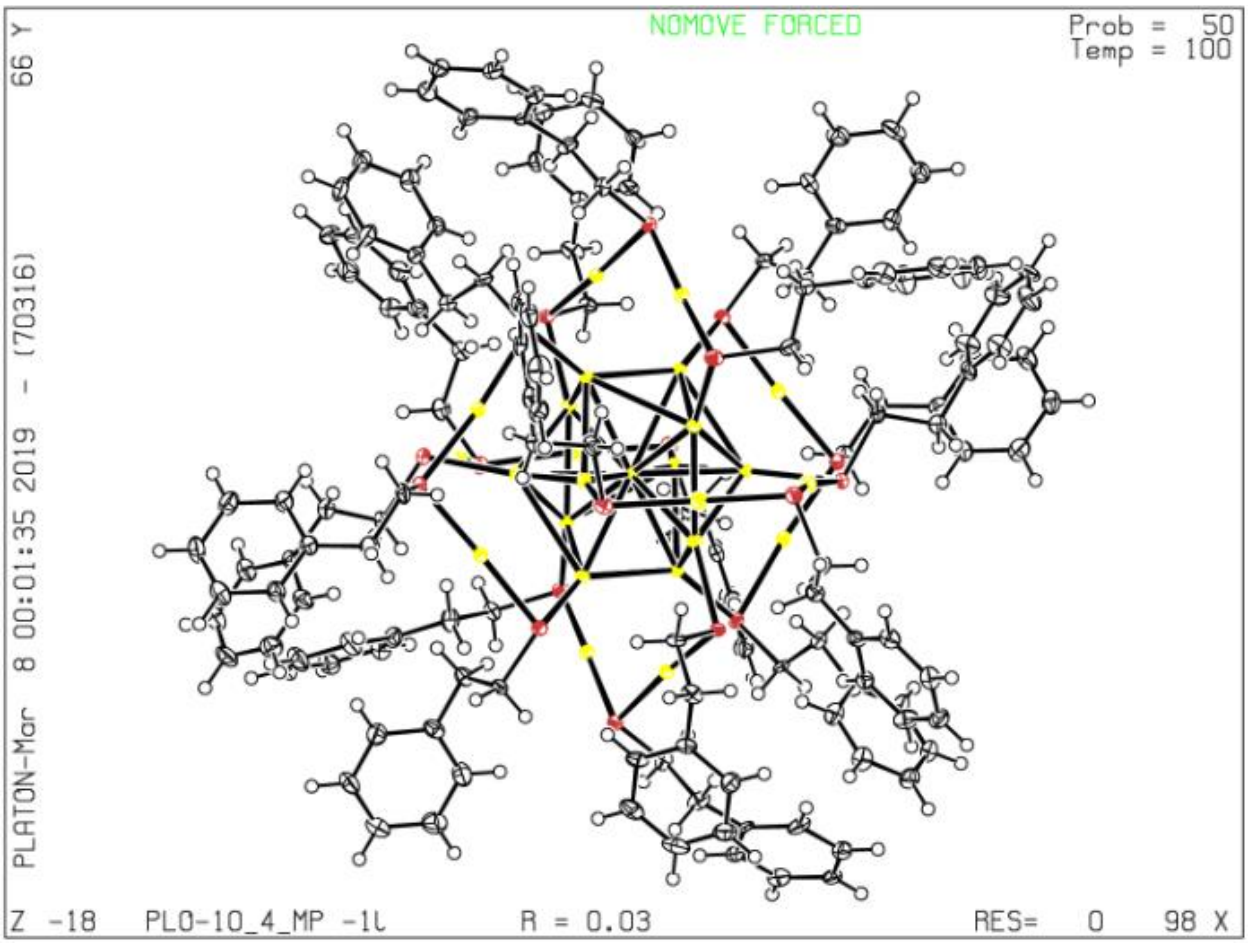


Figure D.7 ORTEP plot of $Au_{25}(PET)_{18}^{0}$ structure from a needle crystal.

D.13 Crystallographic Information File for $Au_{25}(PET)_{18}$ Thin Platelet Sample

```
data_plo-1_4fold
_audit_creation_date              2018-04-18
_audit_creation_method
;
Olex2 1.2
(compiled 2018.04.18 svn.r3501 for OlexSys, GUI svn.r5488)
;
_shelx_SHELXL_version_number      '2014/7'
_audit_contact_author_address     ?
_audit_contact_author_email       ?
_audit_contact_author_name        ''
_audit_contact_author_phone       ?
_publ_contact_author_id_orcid     ?
_publ_section_references
;
Dolomanov, O.V., Bourhis, L.J., Gildea, R.J, Howard, J.A.K. & Puschmann, H.
```

(2009), J. Appl. Cryst. 42, 339-341.

Sheldrick, G.M. (2015). Acta Cryst. A71, 3-8.

Sheldrick, G.M. (2015). Acta Cryst. C71, 3-8.
;
_chemical_name_common ?
_chemical_name_systematic ?
_chemical_formula_moiety 'C144 H162 Au25 S18'
_chemical_formula_sum 'C144 H162 Au25 S18'
_chemical_formula_weight 7393.97
_chemical_melting_point ?
_chemical_oxdiff_formula 'C72 H81 Au12.5 S9'
loop_
_atom_type_symbol
_atom_type_description
_atom_type_scat_dispersion_real
_atom_type_scat_dispersion_imag
_atom_type_scat_source
'C' 'C' 0.0181 0.0091 'International Tables Vol C Tables 4.2.6.8 and 6.1.1.4'
'H' 'H' 0.0000 0.0000 'International Tables Vol C Tables 4.2.6.8 and 6.1.1.4'
'Au' 'Au' -4.4197 7.2980
'International Tables Vol C Tables 4.2.6.8 and 6.1.1.4'
'S' 'S' 0.3331 0.5567 'International Tables Vol C Tables 4.2.6.8 and 6.1.1.4'

_shelx_space_group_comment
;
The symmetry employed for this shelxl refinement is uniquely defined
by the following loop, which should always be used as a source of
symmetry information in preference to the above space-group names.
They are only intended as comments.
;
_space_group_crystal_system 'triclinic'
_space_group_IT_number 2
_space_group_name_H-M_alt 'P -1'
_space_group_name_Hall '-P 1'
loop_
_space_group_symop_operation_xyz
'x, y, z'
'-x, -y, -z'

_cell_length_a 15.0644(2)
_cell_length_b 15.2436(2)
_cell_length_c 20.2268(2)
_cell_angle_alpha 111.3780(10)
_cell_angle_beta 93.4240(10)

```
_cell_angle_gamma                  112.4690(10)
_cell_volume                       3888.48(9)
_cell_formula_units_Z              1
_cell_measurement_reflns_used      51403
_cell_measurement_temperature      293(2)
_cell_measurement_theta_max        72.1300
_cell_measurement_theta_min        3.2670
_shelx_estimated_absorpt_T_max     ?
_shelx_estimated_absorpt_T_min     ?
_exptl_absorpt_coefficient_mu      45.648
_exptl_absorpt_correction_T_max    1.00000
_exptl_absorpt_correction_T_min    0.08487
_exptl_absorpt_correction_type     multi-scan
_exptl_absorpt_process_details
;
CrysAlisPro 1.171.40.4a (Rigaku Oxford Diffraction, 2018)
Empirical absorption correction using spherical harmonics,
 implemented in SCALE3 ABSPACK scaling algorithm.
;
_exptl_absorpt_special_details     ?
_exptl_crystal_colour              'dark black'
_exptl_crystal_colour_modifier     dark
_exptl_crystal_colour_primary      black
_exptl_crystal_density_diffrn      3.158
_exptl_crystal_density_meas        ?
_exptl_crystal_density_method      ?
_exptl_crystal_description         plate
_exptl_crystal_F_000               3289
loop_
  _exptl_crystal_face_index_h
  _exptl_crystal_face_index_k
  _exptl_crystal_face_index_l
  _exptl_crystal_face_perp_dist
 0 1 11 0.0083
 0 -1 -11 0.0083
 9 -7 2 0.0520
 -9 7 -2 0.0520
 -3 -7 8 0.0086
 3 7 -8 0.0066

_exptl_crystal_size_max            0.106
_exptl_crystal_size_mid            0.019
_exptl_crystal_size_min            0.015
loop_
  _exptl_oxdiff_crystal_face_indexfrac_h
  _exptl_oxdiff_crystal_face_indexfrac_k
```

```
 _exptl_oxdiff_crystal_face_indexfrac_l
 _exptl_oxdiff_crystal_face_x
 _exptl_oxdiff_crystal_face_y
 _exptl_oxdiff_crystal_face_z
0.0198 0.9989 10.9910 -0.1429 0.0601 -0.9690
-0.0198 -0.9989 -10.9910 0.1429 -0.0601 0.9690
8.9925 -7.0241 2.0057 0.9347 -0.3124 -0.1652
-8.9925 7.0241 -2.0057 -0.9347 0.3124 0.1652
-3.0228 -6.9791 8.0121 0.3538 0.8965 -0.1371
3.0228 6.9791 -8.0121 -0.3538 -0.8965 0.1371

_exptl_transmission_factor_max     ?
_exptl_transmission_factor_min     ?
_diffrn_reflns_av_R_equivalents    0.0391
_diffrn_reflns_av_unetI/netI       0.0247
_diffrn_reflns_Laue_measured_fraction_full  0.990
_diffrn_reflns_Laue_measured_fraction_max  0.990
_diffrn_reflns_limit_h_max         17
_diffrn_reflns_limit_h_min         -17
_diffrn_reflns_limit_k_max         18
_diffrn_reflns_limit_k_min         -18
_diffrn_reflns_limit_l_max         23
_diffrn_reflns_limit_l_min         -24
_diffrn_reflns_number              64208
_diffrn_reflns_point_group_measured_fraction_full  0.990
_diffrn_reflns_point_group_measured_fraction_max  0.990
_diffrn_reflns_theta_full          66.600
_diffrn_reflns_theta_max           66.600
_diffrn_reflns_theta_min           4.486
_diffrn_ambient_temperature        293(2)
_diffrn_detector                   'CCD plate'
_diffrn_detector_area_resol_mean   ?
_diffrn_measured_fraction_theta_full  0.990
_diffrn_measured_fraction_theta_max  0.990
_diffrn_measurement_details
;
List of Runs (angles in degrees, time in seconds):

  # Type    Start    End  Width  t~exp~   \w     \q     \k     \f   Frames
------------------------------------------------------------------------------
  1  \w    -89.00  89.00   0.50    0.50    --    0.00   9.00-153.00  356
  2  \w    -89.00  89.00   0.50    0.50    --    0.00  43.00 120.00  356
  3  \w      1.00 179.00   0.50    0.50    --   90.00  55.00  60.00  356
  4  \w      1.00 179.00   0.50    0.50    --   90.00  55.00-180.00  356
  5  \w      1.00 179.00   0.50    0.50    --   90.00  55.00   0.00  356
  6  \w      1.00 179.00   0.50    0.50    --   90.00  55.00 -30.00  356
```

```
  7  \w      1.00 179.00   0.50    0.50    --   90.00  55.00-150.00  356
  8  \w      1.00 179.00   0.50    0.50    --   90.00  55.00 120.00  356
  9  \w      1.00 179.00   0.50    0.50    --   90.00  55.00 120.00  356
 10  \w      1.00 179.00   0.50    0.50    --   90.00  55.00 -90.00  356
 11  \w      1.00 179.00   0.50    0.50    --   90.00  55.00  30.00  356
 12  \w      1.00 179.00   0.50    0.50    --   90.00  11.00  60.00  356
;
_diffrn_measurement_device         'four-circle diffractometer'
_diffrn_measurement_device_type    'XtaLAB AFC11 (RCD3): quarter-chi single'
_diffrn_measurement_method         '\w scans'
_diffrn_orient_matrix_type
 'CrysAlisPro convention (1999,Acta A55,543-557)'
_diffrn_orient_matrix_UB_11        0.0450266000
_diffrn_orient_matrix_UB_12        -0.0771648000
_diffrn_orient_matrix_UB_13        -0.0060655000
_diffrn_orient_matrix_UB_21        -0.0947344000
_diffrn_orient_matrix_UB_22        -0.0732968000
_diffrn_orient_matrix_UB_23        0.0123043000
_diffrn_orient_matrix_UB_31        -0.0440133000
_diffrn_orient_matrix_UB_32        -0.0565183000
_diffrn_orient_matrix_UB_33        -0.0829451000
_diffrn_radiation_monochromator    mirror
_diffrn_radiation_probe            x-ray
_diffrn_radiation_type             CuK\a
_diffrn_radiation_wavelength       1.54184
_diffrn_source                     'Rotating-anode X-ray tube'
_diffrn_source_type                'Rigaku (Cu) X-ray Source'
_reflns_Friedel_coverage           0.000
_reflns_Friedel_fraction_full      .
_reflns_Friedel_fraction_max       .
_reflns_number_gt                  13104
_reflns_number_total               13572
_reflns_odcompleteness_completeness  99.01
_reflns_odcompleteness_iscentric   1
_reflns_odcompleteness_theta       66.97
_reflns_special_details
;
 Reflections were merged by SHELXL according to the crystal
 class for the calculation of statistics and refinement.

 _reflns_Friedel_fraction is defined as the number of unique
 Friedel pairs measured divided by the number that would be
 possible theoretically, ignoring centric projections and
 systematic absences.
;
_reflns_threshold_expression       'I > 2\s(I)'
```

_computing_cell_refinement 'CrysAlisPro 1.171.40.4a (Rigaku OD, 2018)'
_computing_data_collection 'CrysAlisPro 1.171.40.4a (Rigaku OD, 2018)'
_computing_data_reduction 'CrysAlisPro 1.171.40.4a (Rigaku OD, 2018)'
_computing_molecular_graphics 'Olex2 (Dolomanov et al., 2009)'
_computing_publication_material 'Olex2 (Dolomanov et al., 2009)'
_computing_structure_refinement 'ShelXL (Sheldrick, 2015)'
_computing_structure_solution 'ShelXT (Sheldrick, 2015)'
_refine_diff_density_max 1.361
_refine_diff_density_min -1.832
_refine_diff_density_rms 0.193
_refine_ls_extinction_coef .
_refine_ls_extinction_method none
_refine_ls_goodness_of_fit_ref 1.113
_refine_ls_hydrogen_treatment constr
_refine_ls_matrix_type full
_refine_ls_number_parameters 844
_refine_ls_number_reflns 13572
_refine_ls_number_restraints 0
_refine_ls_R_factor_all 0.0258
_refine_ls_R_factor_gt 0.0242
_refine_ls_restrained_S_all 1.113
_refine_ls_shift/su_max 0.002
_refine_ls_shift/su_mean 0.000
_refine_ls_structure_factor_coef Fsqd
_refine_ls_weighting_details
'w=1/[\s^2^(Fo^2^)+(0.0343P)^2^+13.9841P] where P=(Fo^2^+2Fc^2^)/3'
_refine_ls_weighting_scheme calc
_refine_ls_wR_factor_gt 0.0617
_refine_ls_wR_factor_ref 0.0626
_refine_special_details ?
_olex2_refinement_description
;
1. Fixed Uiso
At 1.2 times of:
All C(H) groups, All C(H,H) groups
2.a Secondary CH2 refined with riding coordinates:
C00N(H00A,H00B), C00R(H00C,H00D), C00S(H00E,H00F), C00U(H00G,H00H), C00X(H00I,
H00J), C010(H01A,H01B), C011(H01C,H01D), C013(H01E,H01F), C017(H01G,H01H),
C018(H01I,H01J), C01E(H01O,H01P), C01G(H01Q,H01R), C01I(H01T,H01U), C01Q(H01,
H), C01Y(H7AA,HA), C022(H02A,H02B), C1(H1A,H1B), C2(H2A,H2B)
2.b Aromatic/amide H refined with riding coordinates:
C00O(H00O), C00Q(H00Q), C00T(H00T), C00V(H00V), C00W(H00W), C00Z(H00Z),
C012(H012), C019(H019), C01A(H01K), C01B(H01L), C01C(H01M), C01D(H01N),
C01H(H01S), C01J(H01V), C01L(H01W), C01M(H01X), C01N(H01Y), C01O(H01Z),

C01R(H0AA), C01S(H1AA), C01T(H2AA), C01U(H3AA), C01V(H4AA), C01W(H5AA), C01X(H6AA), C01Z(H8AA), C020(H020), C021(H021), C3(H3), C5(H5), C6(H6), C7(H7),
C8(H8), C9(H9), C10(H10), C11(H11), C12(H12), C13(H13), C14(H14), C15(H15), C16(H16), C17(H17), C18(H18), C19(H19), C20(H20)
;
_atom_sites_solution_hydrogens geom
_atom_sites_solution_primary dual
_atom_sites_solution_secondary ?

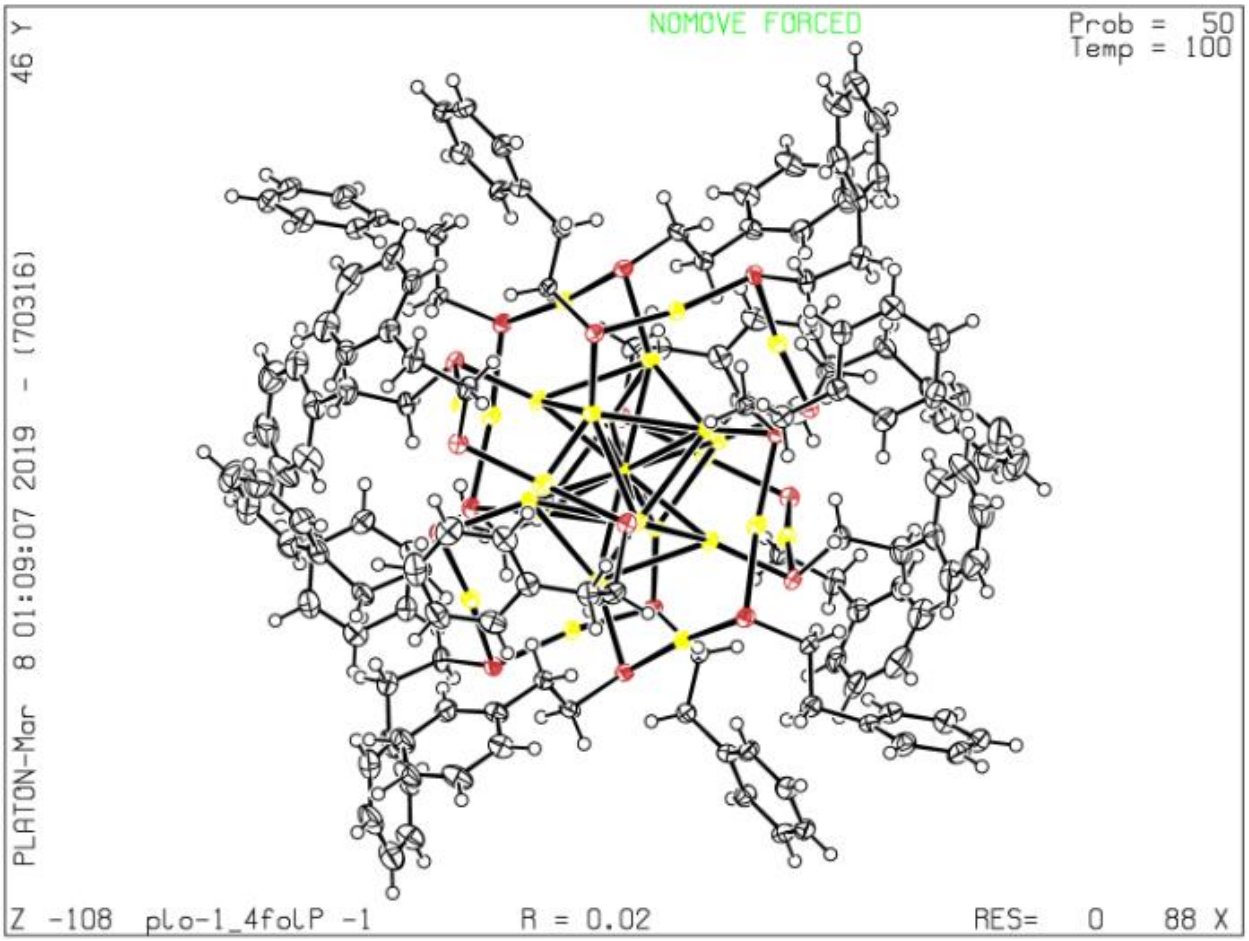


Figure D.8 ORTEP plot of $Au_{25}(PET)_{18}^{0}$ structure from a thin platelet crystal

D.14 Crystallographic Information File for $Au_{25}(PET)_{18}$ Quadrilateral Prism Sample

data_PLO-14_Manual

_audit_creation_method 'SHELXL-2014/7'
_shelx_SHELXL_version_number '2014/7'
_chemical_name_systematic ?
_chemical_name_common ?

```
_chemical_melting_point          ?
_chemical_formula_moiety         ?
_chemical_formula_sum
 'C158 H178 Au25 S18'
_chemical_formula_weight         7578.24

loop_
 _atom_type_symbol
 _atom_type_description
 _atom_type_scat_dispersion_real
 _atom_type_scat_dispersion_imag
 _atom_type_scat_source
 'C'  'C'   0.0181   0.0091
 'International Tables Vol C Tables 4.2.6.8 and 6.1.1.4'
 'H'  'H'   0.0000   0.0000
 'International Tables Vol C Tables 4.2.6.8 and 6.1.1.4'
 'Au'  'Au'  -4.4197   7.2980
 'International Tables Vol C Tables 4.2.6.8 and 6.1.1.4'
 'S'  'S'   0.3331   0.5567
 'International Tables Vol C Tables 4.2.6.8 and 6.1.1.4'

_space_group_crystal_system      triclinic
_space_group_IT_number           2
_space_group_name_H-M_alt        'P -1'
_space_group_name_Hall           '-P 1'

_shelx_space_group_comment
;
The symmetry employed for this shelxl refinement is uniquely defined
by the following loop, which should always be used as a source of
symmetry information in preference to the above space-group names.
They are only intended as comments.
;

loop_
 _space_group_symop_operation_xyz
 'x, y, z'
 '-x, -y, -z'

_cell_length_a                   16.1600(2)
_cell_length_b                   17.7086(2)
_cell_length_c                   17.7130(2)
_cell_angle_alpha                  65.1130(10)
_cell_angle_beta                 81.4300(10)
_cell_angle_gamma                    64.7610(10)
_cell_volume                     4156.42(10)
```

```
_cell_formula_units_Z            1
_cell_measurement_temperature    293(2)
_cell_measurement_reflns_used    ?
_cell_measurement_theta_min      ?
_cell_measurement_theta_max      ?

_exptl_crystal_description       ?
_exptl_crystal_colour            ?
_exptl_crystal_density_meas      ?
_exptl_crystal_density_method    ?
_exptl_crystal_density_diffrn    3.028
_exptl_crystal_F_000             3389
_exptl_transmission_factor_min   ?
_exptl_transmission_factor_max   ?
_exptl_crystal_size_max          ?
_exptl_crystal_size_mid          ?
_exptl_crystal_size_min          ?
_exptl_absorpt_coefficient_mu    42.736
_shelx_estimated_absorpt_T_min   ?
_shelx_estimated_absorpt_T_max   ?
_exptl_absorpt_correction_type   ?
_exptl_absorpt_correction_T_min  ?
_exptl_absorpt_correction_T_max  ?
_exptl_absorpt_process_details   ?
_exptl_absorpt_special_details   ?
_diffrn_ambient_temperature      293(2)
_diffrn_radiation_wavelength     1.54184
_diffrn_radiation_type           CuK\a
_diffrn_source                   ?
_diffrn_measurement_device_type  ?
_diffrn_measurement_method       ?
_diffrn_detector_area_resol_mean ?
_diffrn_reflns_number            57132
_diffrn_reflns_av_unetI/netI     0.0269
_diffrn_reflns_av_R_equivalents  0.0305
_diffrn_reflns_limit_h_min       -19
_diffrn_reflns_limit_h_max       19
_diffrn_reflns_limit_k_min       -20
_diffrn_reflns_limit_k_max       21
_diffrn_reflns_limit_l_min       -19
_diffrn_reflns_limit_l_max       20
_diffrn_reflns_theta_min         4.825
_diffrn_reflns_theta_max         66.598
_diffrn_reflns_theta_full        66.598
_diffrn_measured_fraction_theta_max  0.992
_diffrn_measured_fraction_theta_full 0.992
```

```
_diffrn_reflns_Laue_measured_fraction_max    0.992
_diffrn_reflns_Laue_measured_fraction_full   0.992
_diffrn_reflns_point_group_measured_fraction_max   0.992
_diffrn_reflns_point_group_measured_fraction_full  0.992
_reflns_number_total              14572
_reflns_number_gt                 13612
_reflns_threshold_expression      'I > 2\s(I)'
_reflns_Friedel_coverage          0.000
_reflns_Friedel_fraction_max      .
_reflns_Friedel_fraction_full     .

_reflns_special_details
;
 Reflections were merged by SHELXL according to the crystal
 class for the calculation of statistics and refinement.

 _reflns_Friedel_fraction is defined as the number of unique
 Friedel pairs measured divided by the number that would be
 possible theoretically, ignoring centric projections and
 systematic absences.
;

_computing_data_collection        ?
_computing_cell_refinement        ?
_computing_data_reduction         ?
_computing_structure_solution     ?
_computing_structure_refinement 'SHELXL-2014/7 (Sheldrick, 2014)'
_computing_molecular_graphics     ?
_computing_publication_material   ?
_refine_special_details           ?
_refine_ls_structure_factor_coef  Fsqd
_refine_ls_matrix_type            full
_refine_ls_weighting_scheme       calc
_refine_ls_weighting_details
'w=1/[\s^2^(Fo^2^)+(0.0308P)^2^+30.5676P] where P=(Fo^2^+2Fc^2^)/3'
_atom_sites_solution_primary      ?
_atom_sites_solution_secondary    ?
_atom_sites_solution_hydrogens    geom
_refine_ls_hydrogen_treatment     constr
_refine_ls_extinction_method      none
_refine_ls_extinction_coef        .
_refine_ls_number_reflns          14572
_refine_ls_number_parameters      926
_refine_ls_number_restraints      903
_refine_ls_R_factor_all           0.0294
_refine_ls_R_factor_gt            0.0266
```

_refine_ls_wR_factor_ref 0.0666
_refine_ls_wR_factor_gt 0.0653
_refine_ls_goodness_of_fit_ref 1.039
_refine_ls_restrained_S_all 1.024
_refine_ls_shift/su_max 0.002
_refine_ls_shift/su_mean 0.000

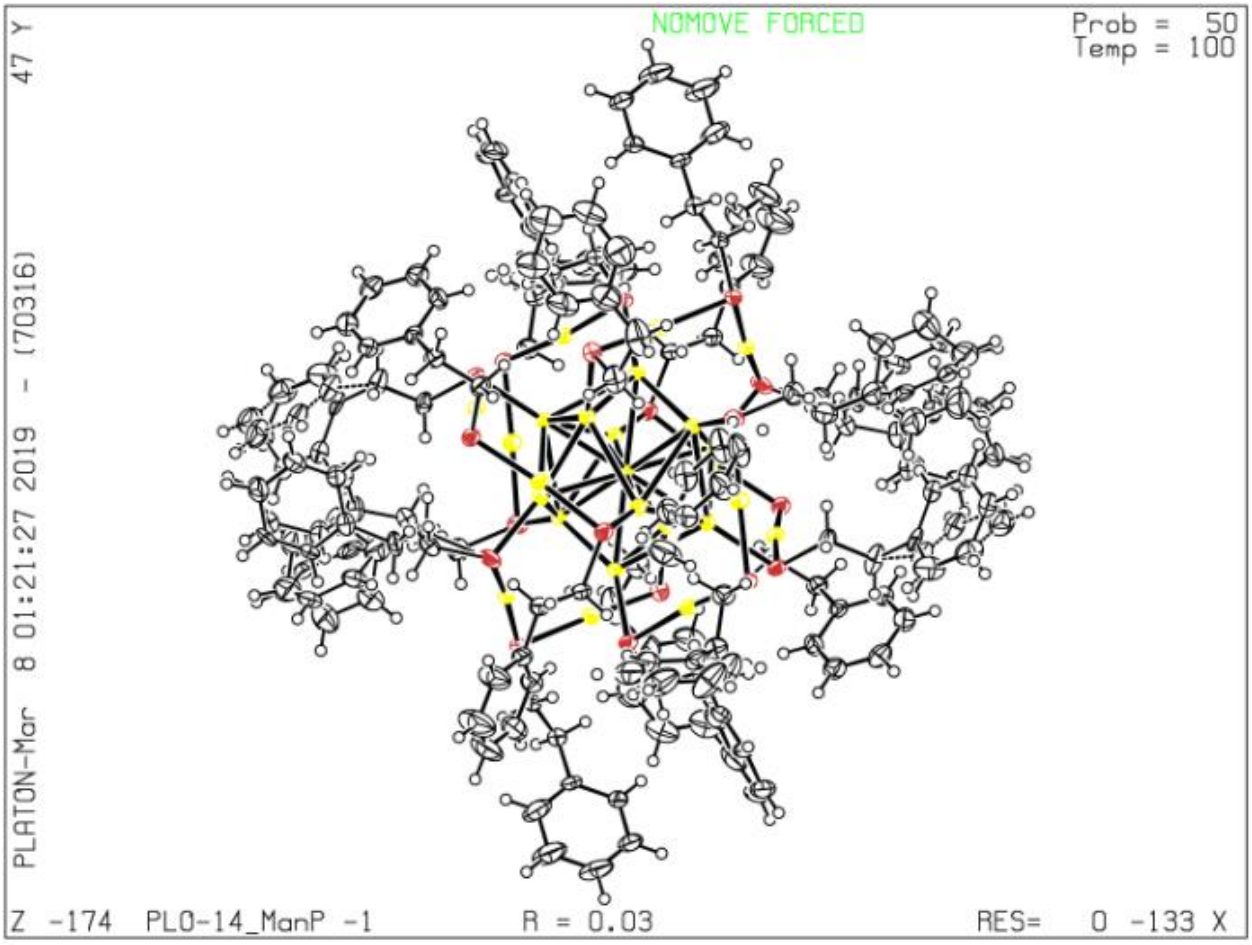


Figure D.9 ORTEP plot of $Au_{25}(PET)_{18}^{0}$ structure from a quadrilateral prism crystal